

Design and Analysis of an Active Underbody Aerodynamic Device for Tractor Trailers

by

MOHAMED IBRAHIM

A Thesis Submitted in Partial Fulfilment

of the Requirements for the Degree of

Master of Applied Science

in

Automotive Engineering

Faculty of Engineering and Applied Science

University of Ontario Institute of Technology

April, 2018

Abstract

At highway speeds, up to 65 % of the total energy used by large trucks is for overcoming aerodynamic drag. The underbody region of a tractor-trailer is responsible for up to 30 % of the aerodynamic drag on tractor-trailers, which is the highest drag created by any region on the vehicle. In this study, a novel concept of an active underbody drag reduction device is developed and investigated. The device was evaluated and optimized using computational fluid dynamics (CFD) techniques. It successfully decreased the drag coefficient of the tractor-trailer model by 4.1 %. Additionally, the device eliminated the underbody recirculation region and reduced the negative adverse pressure in the wake. A novel mechanism is also developed to allow for the active deployment of the device to mitigate some operational issues such as roadway protrusions, parasitic drag at low speeds, snow and dirt accumulation.

Keywords: CFD, aerodynamics, tractor-trailer, underbody device, drag reduction, numerical, collapsible, mechanism.

Acknowledgment

First and foremost, I'd like to thank my parents for their continuous support. Their unconditional love and encouragement has opened many doors for me and allowed me to pursue my dreams; for that I am forever grateful.

Furthermore, I would like to express my sincere gratitude to my supervisor Dr. Martin Agelin-Chaab. His patient guidance, advice and encouragement throughout this academic journey paved the way for this dissertation. His knowledge, vision and insight have made me see far beyond my perceived capability and pushed me through remarkable achievements. It was an honor to work under his mentorship.

Ahmad Hasan deserves special thanks for his support and motivation. I would also like to thank my friends and colleagues at ACE 3030B for providing a wonderful atmosphere that enticed intellectual discussion.

I would also like to thank Bruce L. Storms (NASA Ames Research Center) for sharing the experimental data used in validation. I would also like to thank W. David Pointer (ORNL) for sharing his numerical data that was also used during validation. Financial support of this work by the Natural Science and Engineering Research Council of Canada (NSERC) is gratefully acknowledged.

Table of Contents

Abstract	ii
Acknowledgment	iii
Table of Contents	iv
List of Figures	vii
List of Tables	xii
Nomenclature	xiii
Chapter 1 : Introduction	15
1.1. Background	15
1.2. Motivation	18
1.3. Objective	19
1.4. Thesis Structure.....	19
Chapter 2 : Literature Review.....	21
2.1. Generic Tractor-Trailer Models	21
2.2. Impact of Drag on the Fuel Consumption of Heavy Vehicles	23
2.3. Aerodynamic Drag Distribution of Tractor-Trailers.....	25
2.4. Aerodynamic Drag Reduction Devices.....	26
2.4.1. Tractor Fairings.....	26
2.4.2. Tractor-Trailer Gap Coverage.....	28
2.4.3. Base Drag Reduction	30
2.4.4. Underbody Drag Reduction	33
2.4.5. Other Aerodynamic Devices.....	37
2.4.6. Active Drag Reduction Devices.....	38
2.5. Summary of Literature	43
Chapter 3 : Methodology	45
3.1. System Description	45
3.2. Numerical Approach	51
3.2.1. Flow Modeling.....	51
3.2.2. Turbulence Modeling.....	52
3.2.3. Wall Treatment	57
3.2.4. Model Setup.....	60
3.2.4.1. Preliminary Study Setup.....	60

3.2.4.2.	GCM with Underbody Device Setup.....	62
3.2.5.	Grid Generation	64
3.2.5.1.	Boundary layer grid.....	64
3.2.5.2.	Unstructured grid.....	66
3.2.5.3.	Grid Independence.....	68
3.2.6.	Solver Settings	69
3.2.7.	Post Processing	71
3.3.	Validation.....	72
3.4.	Uncertainty and Error Analysis.....	73
3.5.	Design of Active Mechanism.....	75
3.5.1.	Introduction.....	75
3.5.2.	Design Considerations	76
Chapter 4 :	Results and Discussion.....	78
4.1.	Preliminary Results	78
4.1.1.	Baseline Channel	78
4.1.2.	Channel Optimization	80
4.2.	Baseline Configuration.....	83
4.2.1.	Validation.....	83
4.2.1.1.	Drag Convergence	83
4.2.1.2.	Pressure Coefficient Profile.....	85
4.2.2.	Flow Structure.....	87
4.3.	Detailed Results.....	89
4.3.1.	Velocity and Pressure Profiles	94
4.3.2.	Pressure Contours	98
4.3.3.	Iso-Surfaces.....	104
4.3.4.	Streamlines.....	106
4.3.5.	Turbulence Kinetic Energy and Intensity	108
4.4.	Active Mechanism.....	112
4.5.	Summary of Results	118
Chapter 5 :	Conclusions and Recommendations	120
5.1.	Conclusion.....	120
5.2.	Main Contribution	120

5.3. Limitations	121
5.4. Recommendations for Future Works	121
Publications from Thesis.....	123
References.....	124
Appendix: Detailed Preliminary Study Analysis	131

List of Figures

Figure 2.1: Ground Transportation Systems (GTS), Modified Ground Transportation Systems (M-GTS), Generic Conventional Model (GCM) and Modified Generic Conventional Model (M-GCM).....	22
Figure 2.2: Aerodynamic drag distribution of a tractor-trailer	26
Figure 2.3: Tractor flow control devices: vertical fence, cab deflector, moving surface boundary-layer control, and front splitter (adapted from Choi, Lee, and Park 2014)	27
Figure 2.4: Tractor-trailer gap flow control: gap enclosure, cab side extender, trailer splitter plate, cross-flow trap device, tractor splitter plate and tractor base bleeding (adapted from Choi, Lee, and Park 2014).....	28
Figure 2.5: Drag reduction (%) vs yaw angle: cab deflectors (Drollinger 1987), tractor splitter plate (Drollinger 1987), gap enclosure (Muirhead and Saltzman 1979) and side extenders (Leuschen and Cooper 2006; Choi, Lee, and Park 2014).....	30
Figure 2.6: Passive base drag reduction devices: vertical splitter plate, base cavity and boat tail (adapted from Choi, Lee, and Park 2014)	31
Figure 2.7: Effect of the slant angle (α) on the drag coefficient (CD) on the GM model (Yi 2007).....	32
Figure 2.8: Underbody drag reduction devices of a tractor-trailer: side skirt, belly box, and undercarriage wedge skirt	34
Figure 2.9: T1 fairing (adapted from Ortega and Salari 2008).....	35
Figure 2.10: Vehicle drag coefficient at a yaw angle of 6.1° with respect to the fairing length. Fairing T1 is displayed as a solid line, fairing T2 as a dashed line while the trailer side skirt is a solid triangle (Ortega and Salari 2008)	36
Figure 2.11: Slide Deturbulator on a Freightliner Tractor (modified from Sinha 2008)	38
Figure 2.12: Classification of active flow control (adapted from Cattafesta and Sheplak 2011)	39
Figure 2.13: Steady blowing configurations shown on a Windsor model (adapted from Littlewood and Passmore 2012).....	40
Figure 2.14: Tractor base bleeding and blowing at the base (adapted from Choi, Lee, and Park 2014)	40

Figure 2.15: Moving surface boundary layer (adapted from Choi, Lee, and Park 2014)	42
Figure 3.1: GCM dimensions (in mm)	46
Figure 3.2: First proposed device concept	47
Figure 3.3: Second proposed device concept	47
Figure 3.4: GCM with trailer underbody device shown in isometric view (top), side view (middle) and bottom view (bottom)	49
Figure 3.5: a) Bottom view of the device indicating the side skirt angle b) Side view of the device indicating the ramp angle	50
Figure 3.6: Subdivisions of the Near-Wall Region (ANSYS 2013)	58
Figure 3.7: Difference between the Wall Function approach and the Near-Wall Model approach in modeling the near-wall region (ANSYS 2013)	59
Figure 3.8: GCM with device configuration #2 (Ramp 6° - Side Skirt 4°) (left) and the channel location highlighted in red (right)	61
Figure 3.9: Domain of device configuration #2 in the preliminary study	61
Figure 3.10: Computational domain	63
Figure 3.11: Close up of the inflation layer at the tractor face	65
Figure 3.12: Overview of the surface mesh	66
Figure 3.13: Computational domain refinement regions	67
Figure 3.14: Overview of the computational domain	68
Figure 3.15: y^+ values along the surface of the baseline GCM	70
Figure 4.1: Velocity contour at the centerline of the baseline channel	79
Figure 4.2: Pressure contour at the centerline of the baseline channel	80
Figure 4.3: Comparison between the average outlet velocity of all 12 device configurations	81
Figure 4.4: Comparison between the mass flow rate of all 12 device configurations	81
Figure 4.5: Comparison between the drag monitors for all three grids	84

Figure 4.6: Close up of the drag monitors for all three grids at the last 1000 iterations	84
Figure 4.7: a) Comparison between the predicted pressure coefficient distribution along the vehicle surface with the experimental pressure coefficient data for the GCM (Storms et al. 2006) along the normalized height. b) Comparison between the predicted pressure coefficient distribution along the vehicle surface with the computational results by Pointer (Pointer 2004) along the normalized height.....	86
Figure 4.8: Velocity contour along the centerline of the baseline GCM.	88
Figure 4.9: Velocity contour along the center of the aft trailer wheels of the baseline GCM ($z = 0.123$ m).....	88
Figure 4.10: Velocity contours along the underbody of the baseline GCM.	89
Figure 4.11: Velocity contour of the GCM with the underbody device (Ramp 5° - Side Skirt 4°) at the a) centerline of the model b) center of the aft trailer wheels ($z = 0.123$ m).	91
Figure 4.12: Velocity contour of the GCM with the underbody device (Ramp 6° - Side Skirt 4°) at the a) center of the model b) center of the aft trailer wheels ($z = 0.123$ m).	92
Figure 4.13: a) Velocity contours along the underbody of the baseline GCM with the underbody device (Ramp 5° - Side Skirt 4°). b) Velocity contours along the underbody of the baseline GCM with the underbody device (Ramp 6° - Side Skirt 4°).	93
Figure 4.14: Velocity profile (V_u) at the trailer underbody comparing the baseline GCM (solid line), GCM with Ramp 5° - Side Skirt 4° (dotted line) and the GCM with Ramp 6° - Side Skirt 4° (dashed line). The profiles were located at $y = 0.3$ m with a 0.25 m spacing between a) Sections 1, b) Section 2 and c) Section 3 where Section 3 is at device exit. d) Section 4 is parallel to the trailer backside.	96
Figure 4.15: Coefficient of pressure (C_p) at the trailer underbody comparing the baseline GCM (solid line), GCM with Ramp 5° - Side Skirt 4° (dotted line) and the GCM with Ramp 6° - Side Skirt 4° (dashed line). The profiles were located at $y = 0.3$ m with a 0.25 m spacing between a) Sections 1, b) Section 2 and c) Section 3 where Section 3 is at device exit. d) Section 4 is parallel to the trailer backside.	97
Figure 4.16: Pressure coefficient (C_p) prediction at the trailer base of the a) baseline GCM, b) the GCM equipped with the underbody device (Ramp 5° Side Skirt 4°) and c) the GCM equipped with the underbody device (Ramp 6° Side Skirt 4°).	99

Figure 4.17: Planes where the pressure contours at the wake are located. Plane A was located at the trailer base, while Planes B and C were positioned 0.09 m and 0.18 m from Plane A. Plane 1 was located 0.08 m from the bottom edge of the trailer base, with Planes 1 to 3 were positioned in increments of 0.08 m.	100
Figure 4.18: Comparison between the pressure at the wake of the baseline model (left) and the model with the optimized device (right) at a) Plane A, b) Plane B and c) Plane C. The location of these planes is shown in Figure 4.17.	101
Figure 4.19: Comparison between the wake of the baseline model (left) and the wake of the model with the optimized device (right) at a) Plane 1, b) Plane 2 and c) Plane 3. The location of these planes is shown in Figure 4.17.	103
Figure 4.20: Comparison between the wake of the baseline model (left) and the wake of the model with the optimized device (right) at a slanted plane	104
Figure 4.21: Iso-surface at $V_u = -0.01$ m/s for the a) baseline model and b) model with optimized device	105
Figure 4.22: Velocity contours at the a) underbody of the baseline model and b) the underbody of the model with optimized device.....	106
Figure 4.23: Comparison between the velocity streamlines at the wake of the a) baseline model and b) model with optimized device.....	107
Figure 4.24: Comparison between the velocity streamlines at the underbody of the a) baseline model and b) model with optimized device.....	108
Figure 4.25: Locations where different profiles and contours are obtained. Section 0 is at the bottom edge of the trailer base, with each consecutive section being in increments of 0.09 m, and Section 4 being at the top edge of the trailer base.....	109
Figure 4.26: Turbulence kinetic energy profiles at position a) 0, b) 1, c) 2, d) 3 and e) 4 for the baseline model (solid lines) compared to model with optimized device (dashed lines)	111
Figure 4.27: Comparison between the turbulence intensity at the centerline of the a) baseline model and b) model with optimized device.....	112
Figure 4.28: Device in the deployed position	113
Figure 4.29: Close up of the 2 DOF rail joint.....	114
Figure 4.30: Close up of the ramp pivot joint.....	114
Figure 4.31: Device halfway during ramp collapsing.....	115

Figure 4.32: Close up of the side skirt indicating the locations of the self-closing hinges	116
Figure 4.33: Device with ramp collapsed	116
Figure 4.34: Device in the collapsed position.....	117
Figure A.1: Velocity contour at the centerline of device configuration #1 (Ramp 3° - Straight Side Skirt).....	131
Figure A.2: Velocity contour at the centerline of device configuration #2 (Ramp 3° - Side Skirt 3°).....	132
Figure A.3: Velocity contour at the centerline of device configuration #3 (Ramp 3° - Side Skirt 4°).....	132
Figure A.4: Velocity contour at the centerline of device configuration #4 (Ramp 4° - Straight Side Skirt).....	133
Figure A.5: Velocity contour at the centerline of device configuration #5 (Ramp 4° - Side Skirt 3°).....	134
Figure A.6: Velocity contour at the centerline of device configuration #6 (Ramp 4° - Side Skirt 4°).....	134
Figure A.7: Velocity contour at the centerline of device configuration #7 (Ramp 5° - Straight Side Skirt).....	135
Figure A.8: Velocity contour at the centerline of device configuration #8 (Ramp 5° - Side Skirt 3°).....	136
Figure A.9: Velocity contour at the centerline of device configuration #9 (Ramp 5° - Side Skirt 4°).....	136
Figure A.10: Velocity contour at the centerline of device configuration #10 (Ramp 6° - Straight Side Skirt).....	137
Figure A.11: Velocity contour at the centerline of device configuration #11 (Ramp 6° - Side Skirt 3°).....	138
Figure A.12: Velocity contour at the centerline of device configuration #12 (Ramp 6° - Side Skirt 4°).....	138

List of Tables

Table 3.1: Summary of the different configurations conducted in the preliminary study	51
Table 3.2: Boundary conditions	63
Table 3.3: Summary of the grid independence study for the baseline GCM.....	69
Table 3.4: Summarized under relaxation solver settings	70
Table 4.1: Summary of the preliminary simulations comparing the average outlet velocity, mass flow rate and average outlet pressure of all 12 configurations	82
Table 4.2: Results of the preliminary simulations comparing the average outlet velocity, mass flow rate and average outlet pressure of the top two configurations in terms of mass flow rate.	83
Table 4.3: Drag convergence for the baseline GCM	85
Table 4.4: Results of the evaluation of the underbody devices and their percent drag reduction compared to the baseline GCM.	94

Nomenclature

A	frontal area of the GCM (m ²)
C_D	body-axis drag coefficient
C_p	pressure coefficient
F_D	drag force (N)
Re	Reynolds number = $\frac{V_u w}{\nu}$
u_r	friction velocity (m/s)
V_u	freestream velocity (m/s)
w	width of the GCM
x	axial distance from the front of the model
y	vertical distance from the bottom of the model
z	lateral distance from the centerline of the model

Symbols

α	slant angle (°)
ρ	density (kg/m ³)
μ	dynamic viscosity (P)

μ_t	turbulent viscosity (Pa · s)
ν	kinematic viscosity (m ² /s)
k	turbulence kinetic energy (J/kg)
ϵ	turbulence dissipation rate (J/kg·s)
ω	specific turbulence dissipation rate (1/s)
y^+	dimensionless wall distance

Acronyms

CAD	Computer-Aided Design
CFD	Computational Fluid Dynamics
DES	Detached Eddy Simulation
DNS	Direct Numerical Simulation
DOF	Degrees of Freedom
EWT	Enhanced Wall Treatment
GCI	Grid Convergence Index
LES	Large Eddy Simulations
MSBC	Moving Surface Boundary Layer Control
OEM	Original Equipment Manufacturer
RANS	Reynolds Averaged Navier Stokes
RSM	Reynolds Stress Transport Models
SST	Shear Stress Transport
TKE	Turbulence Kinetic Energy

Chapter 1 : Introduction

In this chapter, the background, motivation, objective and the thesis structure are discussed. The trucking industry and its impact on the transportation sector are introduced. In addition, the aerodynamic drag distribution around a tractor-trailer, drag reduction devices and emissions are provided to give readers a brief overview.

1.1. Background

Ever since the industrial revolution, the transportation of goods has been a critical aspect of every supply chain. For example, the US transportation sector is a trillion-dollar industry where 80% of all cargo is transported by the trucking industry alone (Plunkett Research 2016). In addition, trucks transport 60% of the value of trade between the US and Canada (American Trucking Associations 2015). There are approximately 3.6 million tractor-trailers in the US alone which consume around 54 billion gallons of fuel per annum (American Trucking Associations 2015). On average, a long-haul tractor driver covers over 100,000 miles annually, which is almost 4 times the length of the equator.

Understanding the effects of the flow characteristics on a tractor-trailer is important, as they impact the fuel economy, emissions, driving stability, etc. Fuel economy is a critical reason behind the intensive research interest in heavy vehicles; as overcoming the aerodynamic drag at a typical highway speed requires up to 65% of the total energy used by a heavy vehicle (McCallen et al. 2004). Drag is a force acting opposite to the relative motion of an object that is moving through a fluid. For vehicles, drag resists the motion of a vehicle and causes the vehicle to exert more power to achieve its desired performance (Barnard 2009). The drag coefficient (C_D) is a dimensionless parameter that is usually used to express the drag of a road vehicle. The drag coefficient equation is shown below:

$$C_D = \frac{F_D}{\frac{1}{2}\rho v^2 A} \quad (1.1)$$

Where F_D is the drag force exerted on the vehicle, ρ and v being the density and velocity of the air and A is the projected frontal area of the vehicle.

For bluff bodies, such as heavy vehicles, aerodynamic drag is primarily the result of flow separation and flow stagnation around the vehicle. For tractor-trailers, the aerodynamic drag is distributed around four main regions; the tractor front face, the tractor-trailer gap, the underbody and the trailer base. The underbody region is responsible for approximately 30% of the drag on heavy vehicles, making this region the highest cause of drag (Drollinger 1987; Sovran 1978), while the tractor front face, tractor-trailer gap, and trailer base being responsible for 25%, 20%, and 25% respectively.

In order to reduce drag at the tractor front face and the tractor-trailer gap, significant studies have been carried out in the 1970's and 1980's that resulted in what is referred to as the first generation drag reduction devices (Cooper 2003, 2004). These devices include cab deflectors, fairings, side extenders and edge rounding. Cab deflectors and cab side extenders were responsible for reducing the pre-1980 drag levels by around 25%. Cab deflectors eventually became a staple in every tractor, with manufacturers adopting them as Original Equipment Manufacturer (OEM) parts.

Aerodynamic drag reduction devices aimed primarily at trailers were later introduced, which are referred to as second-generation devices. These devices have been reviewed by Choi, Lee, and Park (Choi, Lee, and Park 2014), which included boat tails and trailer side skirts. For the trailer base, studies were aimed at reducing the size of the wake

or moving it further away from the trailer base. Vertical splitter plates (Gilliéron and Kourta 2010) have been shown to interrupt the recirculation zone formation, reducing drag. However, they have been deemed impractical due to the large size of the required plate and support. Boat tails and base cavities were found to reduce the wake size and/or push the recirculation zone downstream (Balkanyi, Bernal, and Khalighi 2002; Khalighi et al. 2001; Verzicco et al. 2002; Yi 2007). This was achieved by delaying the flow separating from the base or by deflecting the base flow inward. Up to 8% drag reduction was achieved using boat tails, however, the number of modifications required to install these devices on heavy vehicle fleets and the laws limiting the length of tractors prevented boat tails and base cavities from being widely adopted. They also hinder the loading and unloading of trailers. However, collapsible boattails have recently been proposed to mitigate some of these issues and have started to gain traction.

As for the underbody region, straight side skirts were proposed but were found to only reduce aerodynamic drag as the yaw angle increases; having no drag reduction at a yaw angle of zero (Salari, Ortega, and Castellucci 2004; Buil and Herrer 2009; Cooper and Leuschen 2005; McCallen et al. 2004; Tooren and Raemdonck 2009). To mitigate that issue, Ortega and Salari proposed the undercarriage wedge skirt which reduced drag at yaw angles close to zero (Ortega and Salari 2004). Alternatively, belly boxes enclosed the underbody completely to block lateral flow from the underbody. While belly boxes have been found to significantly reduce drag by approximately 38%, they reduced the ground clearance of the trailer significantly (Storms et al. 2004).

These underbody drag reduction devices suffer from common operational issues that hinder their widespread adoption. For example, these underbody devices limit the

ground clearance of the vehicle, which often causes them to get damaged from speed bumps, loading docks, or any road protrusions. Additionally, in countries with a colder climate, side skirts, for example, tend to collect large amounts of ice and/or snow due to their low ground clearance. This causes an increase in the weight of the vehicle, which affects the overall weight at weighing stations; often requiring drivers to clear the ice/snow in order to meet weight restrictions (Ortega and Salari 2008). Trailer underbody fairings were introduced recently to mitigate a few operational issues that side skirts suffer from. It is believed that these operational issues are what is inhibiting the widespread adoption of these aerodynamic drag reduction devices.

1.2. Motivation

As stated earlier, the underbody flow of a tractor-trailer is responsible for approximately 30% of the drag acting on heavy vehicles, making this region the highest cause of drag. Most of the underbody devices available on the market have a few operational issues that prevent underbody drag reduction devices from mass adoption. Therefore, there is a need for a device that can mitigate those issues while being economically and operationally viable. In addition, as the trucking industry uses over 50 billion gallons of diesel a year (American Trucking Associations 2015), fuel savings in this sector can prevent the dumping of billions of pounds of carbon dioxide (CO₂) and other harmful pollutants that cause significant harm to our ecosystem. A drag reduction of 4% would translate to a fuel consumption reduction of around 2% (TIAX 2010). Long-haul tractor-trailer travel around 100,000 miles annually, thus a drag reduction of 4% would translate up to \$2600 in fuel savings for a single tractor-trailer while preventing the

dumping of nearly 6200 pounds of CO₂ into our atmosphere (NRC 2016; EIA 2017; Trucker Path 2017).

1.3. Objective

The main objective of this thesis is to develop and analyze an active underbody aerodynamic device for trailer trucks that overcomes many of the issues of existing devices as enumerated above. To achieve the main objective, three sub-objectives are pursued as follows:

- 1) Develop conceptual models of underbody aerodynamic drag reduction devices that mitigate the operational issues mentioned above.
- 2) Conduct studies to aerodynamically examine and optimize the underbody drag reduction devices in Objective (1).
- 3) Develop a collapsible mechanism to facilitate the implementation of an active system for the underbody devices above. The mechanism should promote easy storage of the device in order to eliminate parasitic drag when not in use (i.e., at low-speed driving) and allow the device to clear road protrusions such as loading docks, speed bumps, etc.

1.4. Thesis Structure

The thesis is divided into five chapters including the current chapter. Chapter 2 presents an extensive literature review, covering the generic tractor trailer models as well as the aerodynamic drag reduction devices currently available for heavy vehicles. The literature review is divided into three main categories; generic tractor-trailer models, aerodynamic drag distribution of tractor-trailers and underbody devices. Chapter 3 presents the methodology used in this research work. In particular, the system description is covered

detailing the proposed device as well as the vehicle model used. In addition, the numerical aspects are discussed, which include turbulence modeling and grid generation. In Chapter 4 the results of the studies are discussed in detail, including validation, drag reduction and the influence of the devices on the flow structure of the model. In addition, the active collapsible mechanism is discussed. Finally, the summary of the results, conclusions, and recommendations for future work are reported in Chapter 5.

Chapter 2 : Literature Review

In this chapter, an extensive literature review is conducted to gain insight into the effect of drag on the fuel consumption of heavy vehicles, as well as different generic models and drag reduction devices. The review is organized as follows; generic tractor-trailer models, the impact of drag on the fuel consumption of heavy vehicles, aerodynamic drag distribution of tractor-trailers, and aerodynamic drag reduction devices.

2.1. Generic Tractor-Trailer Models

The flow structure around tractor-trailers features multiple stagnation points, gap flow, underbody flow and a large wake region; as they geometrically consist of two rectangular bluff bodies. Generally, the flow around a tractor-trailer stagnates around the front grill of the tractor while separating at the trailing edge of the tractor. This separated flow recirculates at the tractor-trailer gap. The flow around the trailer remains attached, separating at the trailers trailing edge. This separating results in a large recirculating region referred to as the wake.

To better understand the flow structure around tractor-trailers, the Heavy Vehicle Drag Consortium developed two simplified tractor-trailer models (McCallen et al. 2004). The Heavy Vehicle Drag Consortium is a collaboration between the following 7 organizations: Lawrence Livermore National Laboratory (LLNL), Argonne National Laboratory (ANL), National Aeronautics and Space Administration Ames Research Center (NASA Ames), University of Southern California (USC), California Institute of Technology (Caltech), Georgia Tech Research Institute (GTRI) and Sandia National Laboratories (SNL). The Heavy Vehicle Aerodynamic Drag Consortium developed two simplified tractor-trailer models, the Ground Transportation Systems (GTS) (Storms et al.

2001; Salari, Ortega, and Castellucci 2004; C. Roy et al. 2004; Ortega and Salari 2004; Maddox and Squires 2004; Gutierrez et al. 1996; Croll et al. 1996; McCallen et al. 2004) model and the Generic Conventional Model (GCM) (McCallen et al. 2004; Heineck, Walker, and Satran 2004; Hyams et al. 2011; Paschkewitz 2006; Storms et al. 2004).

The Ground Transportation System (GTS) baseline vehicle is a model developed by SNL (Gutierrez et al. 1996; Croll et al. 1996). The GTS model is a simplified model that removes all the detailed features of a generic class-8 tractor-trailer. It combines the tractor-trailer into a single geometric model, effectively eliminating the tractor-trailer gap and height difference. A variety of features were also omitted such as wheel wells, mirrors, and underbody features. The simplified model has a semicircular front face with the back being straight cut. Figure 2.1 below shows the GTS model. The Generalized European Transport System (GETS) is another simplified model that was proposed, with a similar structure to the GTS (Van Raemdonck and Van Tooren 2008).

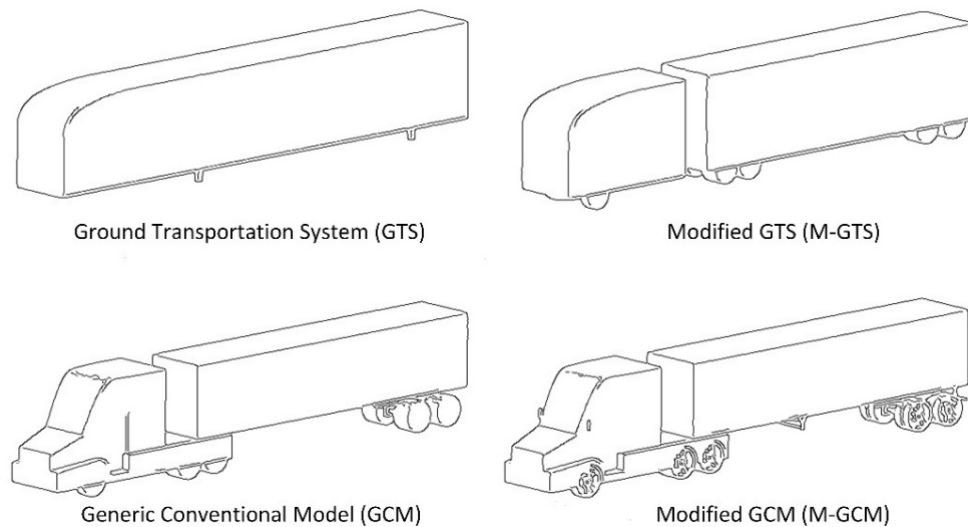


Figure 2.1: Ground Transportation Systems (GTS), Modified Ground Transportation Systems (M-GTS), Generic Conventional Model (GCM) and Modified Generic Conventional Model (M-GCM).

The GCM model, on the other hand, is a more realistic interpretation of a generic class-8 tractor-trailer. The GCM includes a detailed tractor as well as a tractor-trailer gap. The trailer wheel assembly was also modeled. In both the GTS and GCM models, the undercarriage of both the tractor and trailer are modeled as smooth, flat surfaces. Figure 2.1 above shows the difference between the GTS and GCM model. Modifications were made to both of these models to create a more realistic model, as shown in Figure 2.1. The Modified Ground Transportation System (M-GTS) (Castellucci and Salari 2005; McCallen et al. 2007) adds wheels for both the tractor and trailer and also a tractor-trailer gap as shown in Figure 2.1. The Modified Generic Conventional Model (M-GCM) (Castellucci and Salari 2005; McCallen et al. 2007) improves on the GCM model by adding more realistic wheels with no cover and undercarriage.

The GCM model was chosen for this study as it allowed the proposed underbody device to be suitable for a wider range of tractor-trailers, compared to a commercial configuration. In addition, using the GCM model allows for the simulations to be validated using NASA's experimental data on the GCM model; which include the surface pressure coefficients and drag coefficient of the model (Storms et al. 2006).

2.2. Impact of Drag on the Fuel Consumption of Heavy Vehicles

The impact of aerodynamic drag on the fuel consumption of a heavy vehicle is substantial. At a typical highway speed of 110 km/h, 65% of the total energy used by a heavy vehicle is used to overcome aerodynamic drag (McCallen et al. 2004). Heavy vehicles consume about 25% of all fuel, despite accounting for only 7% of the total vehicles on the road (ORNL 2013). The US trucking industry alone consumes around 54 billion gallons of fuel per year (American Trucking Associations 2015). A primary reason to these

staggering numbers is that the fuel economy of heavy vehicles has been largely unregulated for nearly 40 years, resulting in heavy vehicles maintaining the same fuel economy standards since the 1970s; which is around 6 mpg (Cooke 2015). The first fuel efficiency regulations were only passed in 2011 and took effect in 2014. These standards require vehicle manufacturers to reduce the fuel consumption for new trucks by about 16% by 2018 (EPA and NHTSA 2011). The regulations mandated the cut of carbon dioxide equivalent pollution by 270 million metric tons (ORNL 2013; EIA 2013). This is equivalent to the emissions of 4 million passenger cars and trucks over their lifetimes. While these regulations are a necessary first step in reducing fuel usage for heavy vehicles, further steps are necessary to implement new drag reduction technologies to further reduce the annual fuel consumption and prevent global warming emissions.

In general for tractor-trailers at highway speed, the relationship between drag reduction and fuel consumption reduction is 2:1. For example, a drag reduction of 10% would translate roughly to a fuel consumption reduction of 5% (TIAX 2010). The Union of Concerned Scientists predicts that by using existing technology, new trucks can be 40% more efficient by 2025 (Cooke 2015). They estimate that by employing standards to reduce the fuel consumption of heavy vehicles by 40%, the annual fuel consumption can be reduced by 9 billion gallons while preventing 110 million metric tons of global warming emissions.

Thus, aerodynamic drag reduction plays an important role in attaining these fuel consumption reductions. In addition, the implementation of stricter regulations to accelerate the wide adoption of drag reduction devices on heavy vehicles is necessary. For example, even though the trailer is responsible for approximately 65% of the drag on a

heavy (Drollinger 1987; Sovran 1978); trailer drag reduction devices have not achieved wide adoption due to trailers usually being owned by the client, while tractors are owned by the third-party transportation company. Thus, the client has no incentive to spend capital on a fuel saving option that would only benefit the transportation company (Cooper 2003). Future regulations would influence transportation companies to find solutions, i.e., clients with aerodynamically optimized trailers can receive discounts, saving money for the client and transportation company while reducing fuel consumption and emissions.

2.3. Aerodynamic Drag Distribution of Tractor-Trailers

In this section, the aerodynamic drag distribution of tractor-trailers will be discussed. Each region of the tractor-trailer will be examined in its contribution to the overall drag of the vehicle. In addition, the drag reduction devices available for each region will be reviewed. These devices are generally categorized into the following four regions: tractor fairings, tractor-trailer gap coverage, base drag reduction and trailer underbody devices.

In order to recognize the technical challenges that comprise aerodynamic drag reduction, it is essential to understand the drag distribution around a tractor-trailer. The aerodynamic drag distribution around a tractor-trailer is dominated by four regions; the tractor front face, the tractor-trailer gap, the underbody and the trailer base. Figure 2.2 displays the aerodynamic drag distribution for a tractor-trailer. The figure was developed using the data by Drollinger (Drollinger 1987) and Sovran (Sovran 1978). The tractor front face region contributes approximately 25% of the drag, while the tractor-trailer gap and the trailer base contribute 20% and 25% respectively. The underbody region of a tractor-trailer is responsible for the highest drag created by any region of a tractor-trailer; accounting for

up to 30% of the aerodynamic drag. Generally, the data shows that 35% of the drag is caused by the tractor while the remaining 65% is caused by the trailer. Thus, focusing on the underbody of the trailer would theoretically provide the highest potential for drag reduction.

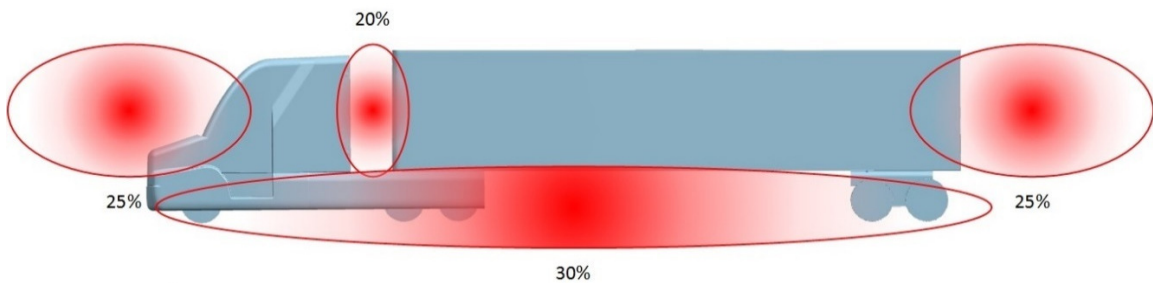


Figure 2.2: Aerodynamic drag distribution of a tractor-trailer

2.4. Aerodynamic Drag Reduction Devices

In this section, the drag reduction devices currently available for tractor-trailers are discussed. The devices are grouped into four categories; tractor fairings, tractor-trailer gap coverage, base drag reduction and underbody drag reduction. These categories cover the four main regions previously mentioned that dominate the drag distribution around a tractor-trailer. In addition, active drag reduction devices are also reviewed.

2.4.1. Tractor Fairings

As previously mentioned, approximately 25% of the drag on a typical tractor-trailer vehicle operating on a highway is due to the flow structure of the front face of the tractor (Sovran 1978; Drollinger 1987). Many solutions have been developed for the drag reduction of the tractor but with only a few being widely used by trucks fleets. It started off with Steers & Saltzman (Steers and Saltzman 1977) in 1977 with the earliest attempt to reduce the fuel consumption of a full-scale tractor-trailer through drag reduction.

This was achieved by rounding the front corners and edges of the tractor as well as attaching a fairing to the tractor roof. With these modifications, they reported approximately 20% fuel savings. Ever since then, many more devices were developed to enhance the flow around the tractor body. These devices include vertical fence (Allan 1981), cab deflectors (Cooper 2003; Leuschen and Cooper 2009a; Malviya, Mishra, and Fieldhouse 2009), moving surface boundary-layer control (Malviya, Mishra, and Fieldhouse 2009) and front spoiler (Hyams et al. 2011; Pankajakshan, Mitchell, and Whitfield 2009). Figure 2.3 below shows the different devices used for tractor flow control.

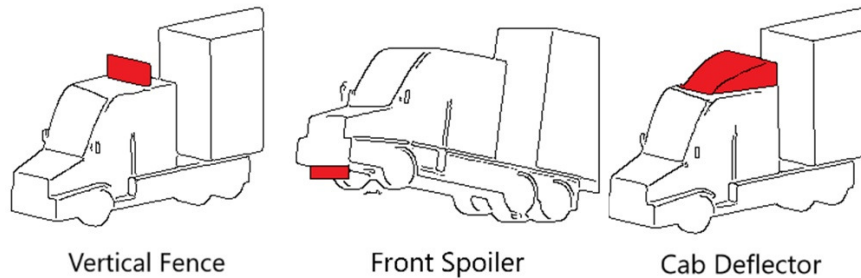


Figure 2.3: Tractor flow control devices: vertical fence, cab deflector, moving surface boundary-layer control, and front splitter (adapted from Choi, Lee, and Park 2014)

Allan (Allan 1981) conducted a study where a vertical fence was tested on a simplified tractor-trailer model. The model consisted of two rectangular boxes in tandem, where the small front box is supported by a larger box at the rear using two metal tubes. The study found that up to 11% drag reduction can be obtained. Meanwhile, another study conducted found that cab deflectors had the largest drag reduction of around 20 % at zero yaw. This drag reduction decreased as the yaw angle increased reaching up to nearly no reduction in aerodynamic drag at a yaw angle of $\pm 20^\circ$ (Drollinger 1987). On the other hand, front spoilers were found to increase drag by 0.2% (Hyams et al. 2011). However, it was concluded that due to the spoiler only increasing drag slightly, this indicates that the

spoiler will reduce drag if a more realistic underbody was used as it will have a significant amount of blockage.

2.4.2. Tractor-Trailer Gap Coverage

Moving on, the tractor-trailer gap plays an essential role in the flow structure of a heavy vehicle, as it accounts for approximately 20% of the aerodynamic drag. Different types of gap flow control were proposed over the years, such as gap enclosure (Allan 1981; Muirhead and Saltzman 1979), cab side extender (Hyams et al. 2011; Storms et al. 2004; Castellucci and Salari 2005; Cooper 2003), trailer splitter plate (McCallen et al. 2004; Hyams et al. 2011; Castellucci and Salari 2005; Mohamed-Kassim and Filippone 2010), cross-flow vortex trap device (Wood 2006; Wood and Bauer 2003), tractor splitter plate (Cooper 2003) and tractor base bleeding (Ortega, Salari, and Storms 2009). These gap flow control add-ons are shown in Figure 2.4.

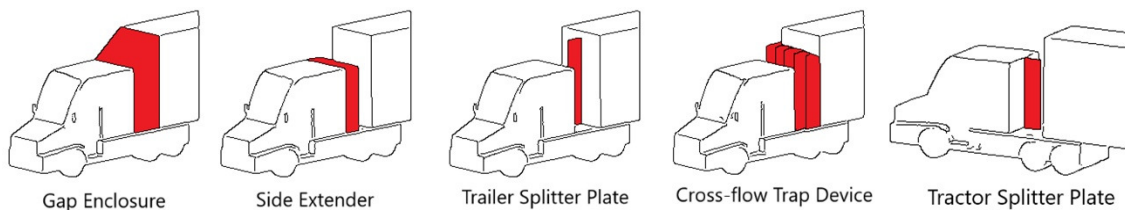


Figure 2.4: Tractor-trailer gap flow control: gap enclosure, cab side extender, trailer splitter plate, cross-flow trap device, tractor splitter plate and tractor base bleeding (adapted from Choi, Lee, and Park 2014)

Gap enclosures prevent the flow from recirculating between the tractor and trailer but are not a viable solution as they hinder the tractors turning ability as well as make it more complex to detach the trailer from the tractor. In addition, different tractor-trailer configurations have different gap dimensions which makes it difficult for companies to come up with a universal solution. Side extenders, on the other hand, are the most widely used add-on devices to reduce gap flow. They delay flow separation from the tractor, which

in return forces the recirculation region to form further away from the tractor base, reducing drag. This also causes a reduction in the flow volume on the frontal area of the trailer, reducing the aerodynamic drag force on the trailer (Castellucci and Salari 2005). While not as effective as side extenders, trailer splitter plates reduce drag by interfering with the gap flow (Ortega and Salari 2008; McCallen et al. 2004). Also, tractor splitter plates have been shown to reduce aerodynamic drag at large yaw angles by blocking the gap flow (Drollinger 1987). Cross-flow vortex trap devices (Leuschen and Cooper 2009b; Wood and Bauer 2003) are multiple splitter plates installed on the front face of a trailer. Crossflow develops in the gap, separating at the leading edges of the splitter plates. This forms a vortex that is trapped in the plates; these trapped vortices induce low pressure locally reducing the aerodynamic drag force on the trailer. This device was estimated to obtain up to 10% in fuel savings (Leuschen and Cooper 2009b; Wood and Bauer 2003).

As tractor-trailers are mainly operated in open environments, such as highways, where the aerodynamics will be influenced significantly under crosswind conditions; performance of drag reduction add-ons are evaluated at various yaw angles. As shown in Figure 2.5, the drag reduction performance of different add-ons varies significantly at different yaw angles. Cab deflectors, which were discussed in the previous section, had the largest drag reduction of around 20 % at zero yaw. This drag reduction decreased as the yaw angle increased reaching up to nearly no reduction in aerodynamic drag at a yaw angle of $\pm 20^\circ$. Tractor splitter plates were found to display the same phenomenon where the drag reduction decreased from a yaw angle of zero to a yaw angle of $\pm 15^\circ$, then the drag reduction started to increase. Gap enclosure displayed a phenomenon opposite to both tractor splitter plates and cab deflectors, as gap enclosures provided the lowest drag

reduction at a yaw angle of zero, while significantly increasing at about 5° yaw reaching up to 30% in drag reduction. Finally, side extenders displayed behavior similar to gap enclosure, where the drag reduction was over 40 % at a yaw angle of zero, decreasing to approximately 25 % at a yaw angle of 20°, and then increasing back to approximately 40% at a yaw angle of 30°.

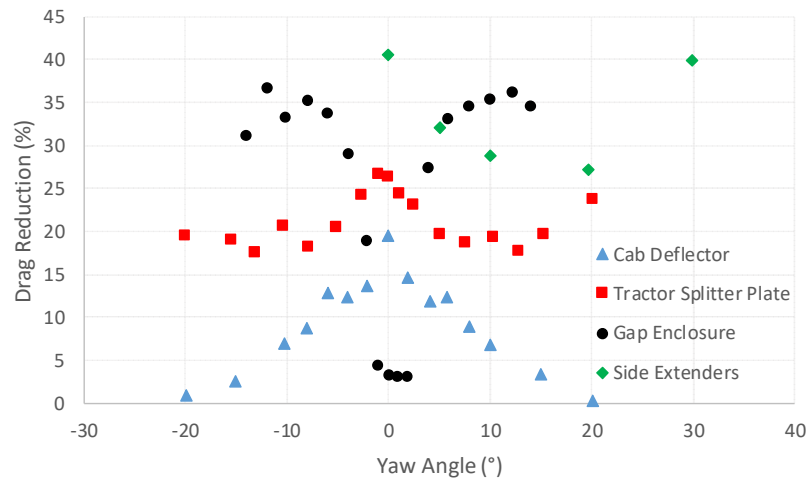


Figure 2.5: Drag reduction (%) vs yaw angle: cab deflectors (Drollinger 1987), tractor splitter plate (Drollinger 1987), gap enclosure (Muirhead and Saltzman 1979) and side extenders (Leuschen and Cooper 2006; Choi, Lee, and Park 2014)

2.4.3. Base Drag Reduction

As most heavy vehicles are bluff-body shapes with blunt trailing edges, the pressure drop at the trailer base is large; thus influencing the drag significantly (Hucho and Sovran 1993). Flow separation occurs at the trailing edge of the trailer causing the formation of a large recirculation region at the wake; which reduces the base pressure. Base drag reduction has been achieved by reducing the size of the recirculation region or by moving it further away from the base (Balkanyi, Bernal, and Khalighi 2002; Englar 2001; Gilliéron and Kourta 2010; Howell, Sheppard, and Blakemore 2003; Littlewood and Passmore 2012;

Peterson 1981; Wong and Mair 1983; Yi 2007). Figure 2.6 shows these base drag reduction devices.

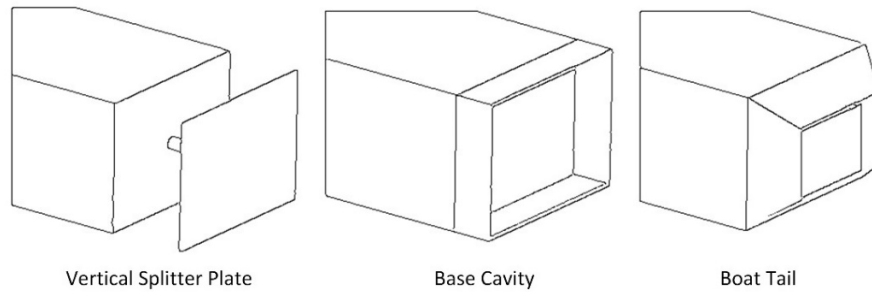


Figure 2.6: Passive base drag reduction devices: vertical splitter plate, base cavity and boat tail (adapted from Choi, Lee, and Park 2014)

Vertical splitter plates have been shown to interrupt the formation of the recirculation bubble, causing a reduction in drag (Gilliéron and Kourta 2010). However, it was deemed impractical due to the large size of the plate and support. On the other hand, base cavities and boat tails extend the edges of the base to delay the formation of the recirculation region and/or reduce size of the region by either delaying the flow separation at the base or by diverting the flow inward (Balkanyi, Bernal, and Khalighi 2002; Khalighi et al. 2001; Verzicco et al. 2002; Yi 2007). The difference between base cavities and boat tails is that base cavities extend directly from the base while boat tails are tapered at a slant angle (α). Figure 2.7 shows the effect of the slant angle (α) on the coefficient of drag (C_D) on the GM Model (Yi 2007).

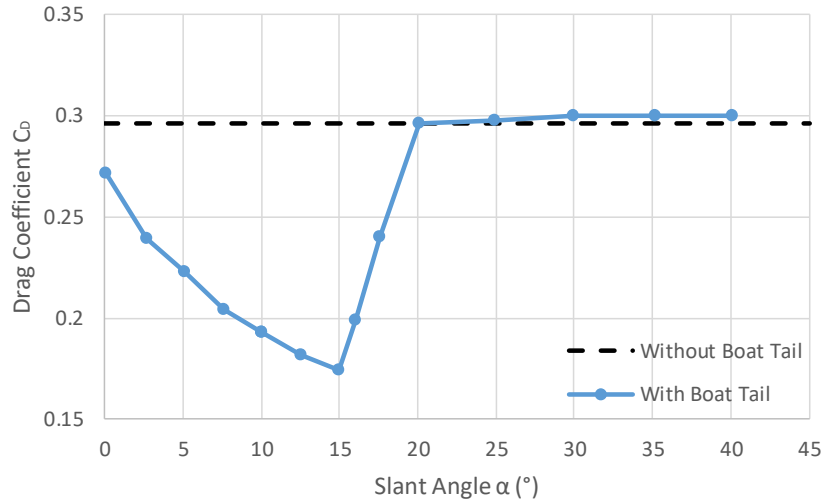


Figure 2.7: Effect of the slant angle (α) on the drag coefficient (C_D) on the GM model (Yi 2007)

Yi (Yi 2007) investigated the effect of the slant angle (α) on the drag coefficient (C_D) of the GM model and the flow structure near the boat tail. It was found that at a slant angle between 5° and 15° a separation bubble was formed at the leading edge of the boat tail. In addition, flow reattachment causes the strong near-wall momentum to delay the separation to the trailing edge of the boat tail. This resulted in significant drag reduction that peaked at a slant angle of approximately 15° . Similar results were found by (Wong and Mair 1983; Yi 2007; Han, Hammond, and Sagi 1992), where the slant angle and length of the boat tail affected significantly the drag of the heavy vehicle. Another study (Heineck, Walker, and Satran 2004) obtained a drag reduction of up to 8% using a GTS model with a boat tail in a wind tunnel.

Compared to all the currently available base drag-reduction devices, boat tails are considered the most effective. Due to the number of modifications required in order to apply them to heavy vehicle fleets and laws limiting the length of tractors, boat tails were not widely adopted.

2.4.4. Underbody Drag Reduction

As previously mentioned, the underbody region of a tractor-trailer is responsible for the highest drag created by any region of a tractor-trailer; accounting for up to 30% of the aerodynamic drag. Additionally, 35% of the drag is caused by the tractor while the remaining 65% is caused by the trailer. Thus, focusing on the underbody of the trailer would theoretically provide the highest potential for drag reduction. In this section, underbody drag reduction devices available will be covered and discussed in detail.

The undercarriage straight skirt (Salari, Ortega, and Castellucci 2004; Buil and Herrer 2009; Cooper and Leuschen 2005; McCallen et al. 2004; Tooren and Raemdonck 2009), belly box (Cooper and Leuschen 2005; Leuschen and Cooper 2006) and undercarriage wedge skirt (Ortega and Salari 2004; Cooper and Leuschen 2005) in Figure 2.8 are the only devices available for underbody drag reduction (excluding the trailer underbody fairing (Ortega and Salari 2008) which will be discussed later on in this section). Undercarriage straight skirts were found to only reduce aerodynamic drag as yaw increases, with nearly no reduction at zero yaw. In order to mitigate this issue, Ortega and Salari (Ortega and Salari 2004) created an undercarriage wedge skirt which reduced drag only at a yaw angle close to zero. Belly boxes, on the other hand, block lateral flow through the ground clearance which is sufficient to reduce drag by approximately 38% (Storms et al. 2004).

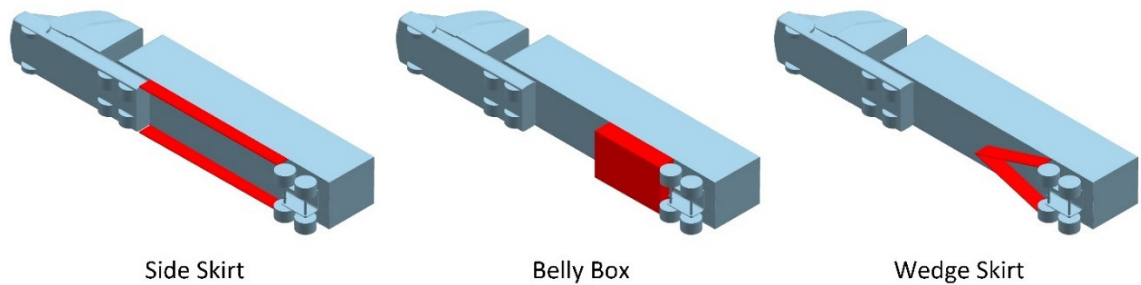


Figure 2.8: Underbody drag reduction devices of a tractor-trailer: side skirt, belly box, and undercarriage wedge skirt

While some of these operational issues can be mitigated by deploying skirts that can retract to increase the vehicles ground clearance (Schoon 2007), Ortega and Salari (Ortega and Salari 2008) have designed a trailer underbody fairing that can overcome some of the drawbacks of side skirts. CFD simulations were performed on a full-scale Freightliner Columbia tractor with a 13.7 m long freight van. The tractor was simplified by sealing the front grill, as it has been shown to have negligible effects on the drag of the vehicle (Leuschen and Cooper 2006). Two types of underbody fairing designs were investigated, the T1 and the T2. The T1 and T2 were identical except for one primary difference; the T2 had a 0.97 m wide channel that covered the length of the fairing. The T1 fairing is shown in Figure 2.9. Both fairings were evaluated in terms of drag reduction to a traditional side skirt.

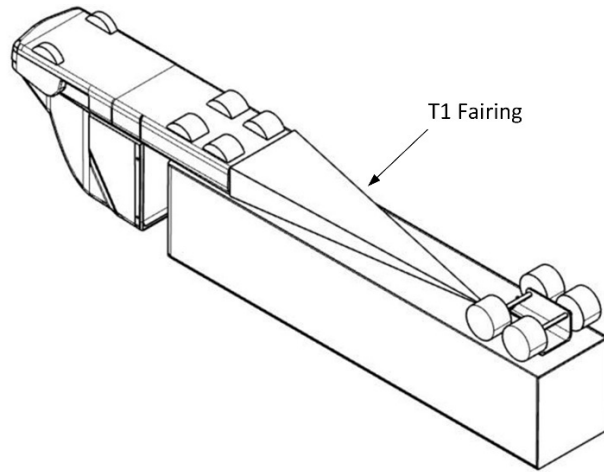


Figure 2.9: T1 fairing (adapted from Ortega and Salari 2008)

The simulations were performed with 0.2% blockage and a width-based Reynolds number of 5 million. Also, the vehicle was simulated on a moving ground plane. The $k - \omega$ SST turbulence model with wall function was employed for its known robustness and reduced computational time and data storage requirements.

The baseline drag coefficient of the tractor-trailer was found to be 0.641, where the majority of the drag was due to the tractor (0.429). For the T1 fairings, the coefficient of drag C_d decreased as the fairing length was increasing. The longest T1 fairing displayed a drag coefficient of 0.617. As for the T2 fairing, the same phenomenon was displayed with a substantial overall reduction in the drag coefficient. The longest T2 fairing displayed a drag coefficient of 0.599. This was less than the coefficient of drag of the trailer with side skirts, which had a coefficient of drag of 0.605. The drag coefficient of the vehicle with respect to the fairing length is displayed in Figure 2.10 for both the T1 and T2 fairings.

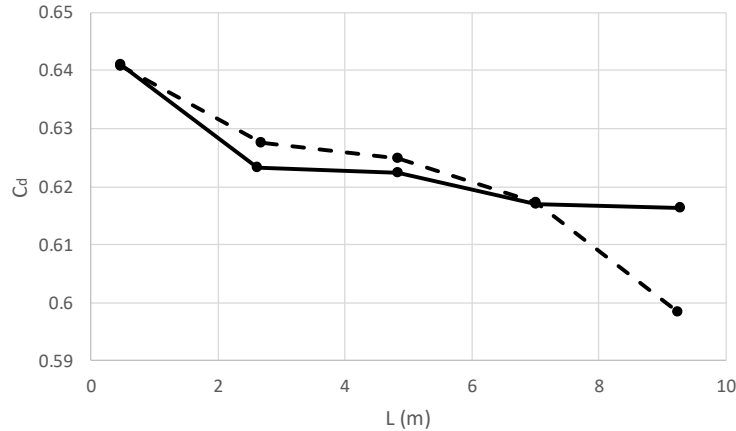


Figure 2.10: Vehicle drag coefficient at a yaw angle of 6.1° with respect to the fairing length. Fairing T1 is displayed as a solid line, fairing T2 as a dashed line while the trailer side skirt is a solid triangle (Ortega and Salari 2008)

By examining the trailer underflow with and without the fairing, the underbody flow physics were determined. It was found that with the baseline trailer, the underbody trailer flow was recirculating after being separated from the tractor drive wheels and underbody. The recirculation zone extended about 5.7 m downstream of the tractor drive wheels. The fairing provided a surface where the underflow can reattach; this reduced the recirculation zone as the fairing length increased and nearly eliminating it using the longest configuration (9.2 m).

As previously discussed, the underbody of the tractor-trailer accounts for the highest percentage of drag on a heavy vehicle, yet it is given less attention. This brings on the question of why underbody drag reduction devices are not accepted on a wide scale. This is due to multiple economic and operational issues. Trailer underbody devices suffer from two economical disadvantages; the first being that installation of them requires modifications to the trailers, which are much greater in number compared to tractors. This means that they require a larger capital. Secondly, as trailers are usually owned by the client, the client has no incentive to spend capital on a fuel saving option that will only

benefit a third-party transportation company. In addition, underbody devices create a few operational issues. Side skirts limit the ground clearance of the vehicle which results in them being damaged from road protrusions, such as speed bumps or railroad crossings. In countries with a colder climate, side skirts tend to collect large amounts of ice. This causes an overall increase in the vehicle weight, which requires the driver to clear the ice before entering weight stations. More importantly, parasitic drag due to skin friction from drag reduction devices needs to be mitigated as it can adversely affect the drag of the vehicle at low speeds (i.e., city driving).

2.4.5. Other Aerodynamic Devices

Sinha (Sinha 2008) patented a flexible surface Deturbulator tape that is used to streamline tractor-trailers. The Deturbulator tape works by weakening the vortices in separated flow regions. Applying a strip of 50-mm wide and 1.8 m long Deturbulator tape on both sides of the tractor cab was found to increase the fuel economy by 4%. In addition, adding Deturbulators on the tractors front corners increased the fuel economy by 8%. Up to 29% improvement in fuel economy was achieved using a full Deturbulator treatment on a Volvo Van-Trailer Tractor. The full Deturbulator treatment consisted of placement on the mirrors, front bumper, top lateral wind deflectors, the top of the cab and both sides of the cab. The tractor-trailer was run for two weeks before treatment and two weeks after the Deturbulator treatment to assess the fuel economy with varying loads. Figure 2.11 shows the locations of the Deturbulators. In addition, swaying due to crosswinds was reduced. Storms, Satran, Heineck, and Walker (Storms et al. 2006) have tested vortex generators by attaching them to the side of the trailer at both the middle and the end of the trailer. This was applied to the GCM model in hope that it will reduce the vehicles wake size due to the

added vorticity. The results showed that the vortex generators increased the drag compared to the baseline vehicle. Also, drag was found to increase significantly at higher yaw angles.



Figure 2.11: Slide Deturbulator on a Freightliner Tractor (modified from Sinha 2008)

2.4.6. Active Drag Reduction Devices

Active flow control devices have received increased attention within the recent years in the automotive industry. They provide the potential to modify the flow around a vehicle without requiring any modification to the external shape. Various types of active flow control have been proposed over the years with few ever moving from laboratories to real-world application. A primary reason is due to the difficulty of designing an active flow control device. Flow control actuators are generally classified into three sections, fluidic, moving object/surface, plasma (Figure 2.12). In this section, current active flow control that relates to tractor-trailers will be reviewed and discussed in detail.

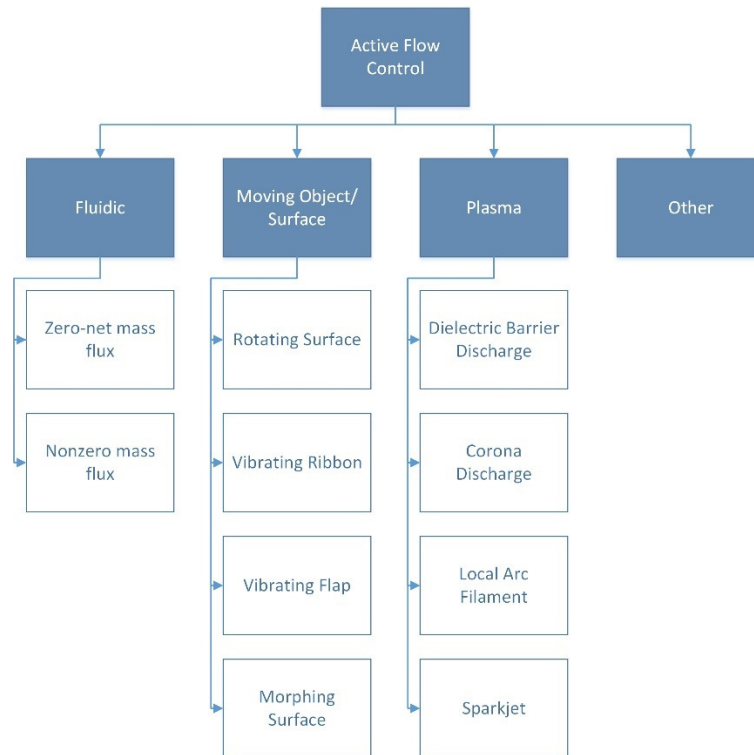


Figure 2.12: Classification of active flow control (adapted from Cattafesta and Sheplak 2011)

Fluidic active flow control devices work by either providing fluid injection or suction. They are classified as zero-net-mass flux (synthetic jets) and nonzero mass flux devices. Zero-net-mass flux devices operate by ingesting and expelling fluid in an oscillatory manner. This is applied through an orifice where only the working fluid is used. Nonzero mass flux devices use an external fluid source while expelling the fluid in either a steady or/and oscillatory manner.

Blowing at the base (often called base bleeding) is a method of achieving drag reduction by moving the low-pressure region downstream of the vehicle base (Englar 2001; Howell, Sheppard, and Blakemore 2003; Littlewood and Passmore 2012). Low-velocity air is injected into the base region of the vehicle, moving the low-pressure region further downstream. Littlewood and Passmore (Littlewood and Passmore 2012) conducted wind tunnel experiments on a 1/4th scale Windsor model. Four different steady blowing

configurations were tested. Only configuration D, angled downward and downstream, produced a drag reduction. All four configurations are shown in Figure 2.13.

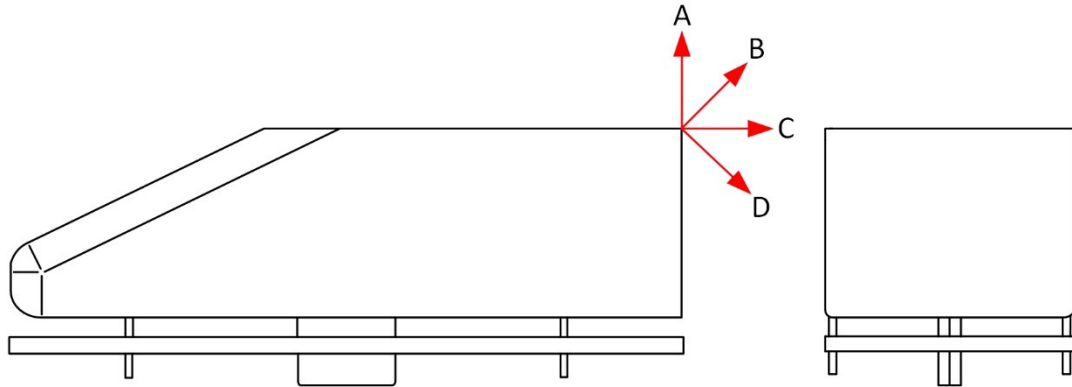


Figure 2.13: Steady blowing configurations shown on a Windsor model (adapted from Littlewood and Passmore 2012)

Tractor base bleeding was found to achieve drag reduction higher than side extenders; however, base bleeding requires an implementation of an active bleeding system which requires additional running cost (McCallen et al. 2007). In addition, base bleeding and base blowing require relatively high additional power input, making them impractical for real-life usage. Tractor base bleeding and base blowing are shown in Figure 2.14.

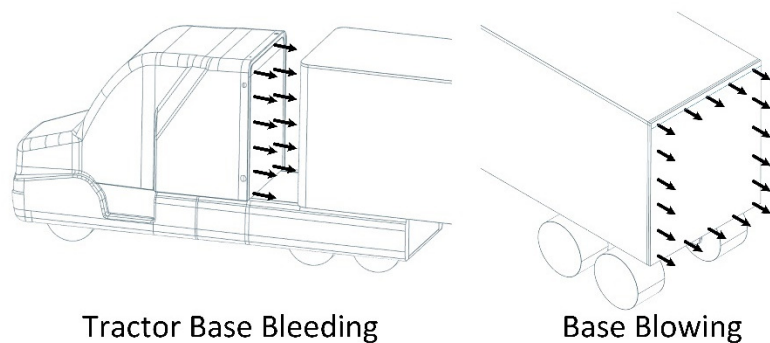


Figure 2.14: Tractor base bleeding and blowing at the base (adapted from Choi, Lee, and Park 2014)

Another numerical study focused on the integration of a microjet network on a square back Ahmed body (Peres and Pasquetti 2013). The study found that up to 30% drag

reduction can be obtained using steady blowing, which agreed with the results obtained by (Rouméas, Gilliéron, and Kourta 2009). In addition, they found that synthetic blowing achieved up to 10% drag reduction.

Another category of active flow control is moving object/surface. It involves using a moving part in order to inject or suck fluid to induce local fluid motion. A study conducted by (Singh et al. 2005) investigated momentum injection using wind tunnel experiments and CFD simulations. Two boxes were used to represent the tractor and trailer in tandem. Momentum injection was conducted using a rotating cylinder. The rotating cylinder diameter and speed were varied to determine the effects on the drag coefficient of the model. A drag reduction of up to 35% was concluded after the optimization of the momentum injection on the two-dimensional tractor-trailer model. It is important to mention that the results were obtained with the model placed on the ground and the underbody flow completely ignored. In addition, both the trailer and the tractor were the same height. Malviya, Mishra, and Fieldhouse conducted a numerical study on a simplified tractor-trailer model with a moving surface boundary control (MSBC) (Malviya, Mishra, and Fieldhouse 2009). Four different configurations were simulated in the study; a baseline configuration with no devices, the model with a cab fairing, the model with the proposed MSBC system and the model with both the MSBC system and the cab fairing. The MSBC is composed of a rotating cylinder that is installed at the top front edge of the trailer (Figure 2.15). The MSBC system was found to create a more streamlined flow passage where the flow stagnates at the trailer. The study showed that using MSBC reduced the coefficient of drag of the baseline vehicle by 13%. When used alongside a cab fairing, the coefficient of drag was reduced by an additional 9%; which resulted in an overall drag reduction of

approximately 22%. This provides a power consumption reduction of 13% while only requiring 8% of the power saved for the rotating cylinder to run.

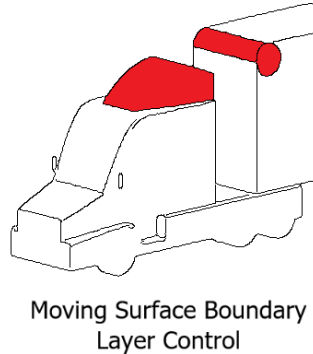


Figure 2.15: Moving surface boundary layer (adapted from Choi, Lee, and Park 2014)

Another category of active drag reduction devices is plasma actuators. Plasma actuators have been used for flow control; such as vortex generation, noise control, supersonic/hypersonic flow control and flight control. Only recently have plasma actuators found their way from the lab into viable solutions.

Roy conducted an experimental study on a 1:60 scale model tractor-trailer model with a serpentine plasma actuator (S. Roy et al. 2016). This was the first successful study to report drag reduction on a vehicle at highway speeds using plasma actuators. The study was conducted in a wind tunnel at speeds of 60 and 70 mph. Two types of plasma actuators were tested by attaching them to the back of the vehicle, linear and serpentine actuators. They found that the serpentine actuator reduced the aerodynamic drag of the vehicle by approximately 15% at 60 mph and 10% at 70 mph while the linear actuator of a comparable size failed to reduce the drag. However, the electric power needed to run the actuator was approximately 4.5 times the power saved from the drag reduction on the scaled model.

Thus, it was concluded that further scaling analysis would be required to determine if the device would be practically viable for a full-scale heavy vehicle.

Corke and Spivey have developed and patented with the University of Notre Dame a method of using plasma to reduce drag on class 8 tractor-trailers (Corke and Spivey 2008). The method is currently being developed by a start-up called Plasma Stream Technologies. The device, which is called the eTail, consists of two long high voltage electrode strips that energize the air above it at speeds over 72 km/h. These charged ions force the turbulent, high-energy airflow at the edges to move into a low-energy region that is right behind the vehicle. This, in turn, minimizes the drag of the vehicle as it reduces the wake size.

2.5. Summary of Literature

The literature covering the different generic truck models available, as well as drag reduction devices for tractors and trailers have been reviewed in this chapter. In addition, the impact of drag on the fuel consumption of heavy vehicles is discussed.

Tractor-trailers have four main regions that constitute the aerodynamic drag distribution; the tractor front face, the tractor-trailer gap, the underbody and the trailer base. Among these regions, the literature reveals that the underbody region accounts for the majority of the drag; which is approximately 30% of the total aerodynamic drag on a tractor-trailer. In addition, the trailer is responsible for 65% of the total drag of a tractor-trailer. Therefore, the underbody region of the trailer has the highest drag reduction potential. Heavy vehicles consume a substantial amount of fuel, consuming approximately 25% of all fuel despite accounting for only 7% of the total vehicles on the road (ORNL 2013). In addition, 65% of the energy used by a tractor-trailer at highway speed is to overcome aerodynamic drag (McCallen et al. 2004). Thus, reducing the aerodynamic drag

of tractor-trailers can have substantial positive effects; both economically and environmentally.

Several underbody drag reduction devices have been proposed but what prevents them from being widely accepted is multiple economical and operational disadvantages. The first economical issue is that their installation requires modifications to the trailers, which are much greater in number compared to tractors. Secondly, trailers are usually owned by the client, and there is no incentive on the part of the client to spend capital on a fuel saving option that will only benefit a third-party transportation company (Cooper 2003). In addition, underbody devices create a few operational issues. Side skirts limit the ground clearance of the vehicle which results in them being damaged from protrusions on the road, such as speed bumps or railroad crossings. Additionally, in countries with a colder climate, side skirts tend to collect large amounts of ice and snow. This causes an overall increase in the vehicle weight, which requires the driver to remove the ice/snow before entering weight stations. More importantly, parasitic drag due to skin friction from drag reduction devices needs to be prevented as it can adversely affect the drag of the vehicle at low speeds. This leaves a lot to be desired in order to create a device that is both operationally and economically practical. Thus, the present work is conducted to investigate and develop a novel device that mitigates these issues.

Chapter 3 : Methodology

In this chapter, the methodology used to conduct this research thesis is discussed. The chapter is split into four sections; system description, numerical approach, validation and uncertainty and error analysis. In the system description section, the underbody device proposed will be introduced as well as the tractor-trailer model used to evaluate the device. The numerical approach section includes flow and turbulence modeling in addition to grid generation. This is followed by validation which covers the procedure used to validate the baseline model with available experimental and numerical data. Finally, the methodology used in conducting the error analysis for this study is discussed in the error analysis section.

A numerical approach was selected to conduct this research primarily due to the availability of experimental data to rigorously validate a numerical model and allow for a rapid and comprehensive preliminary study. Individually testing different concepts in a wind tunnel is costly and inefficient while a theoretical approach would be impractical. A Reynolds Averaged Navier-Stokes (RANS) turbulence model was selected in conducting this research due to its proven robustness in predicting the drag and pressure distribution of the selected generic model along with the computing power available.

3.1. System Description

As previously mentioned, the baseline model chosen for this study was the Generic Conventional Model (GCM). Using a generic tractor-trailer model allowed the proposed underbody device to be suitable for a wider range of tractor-trailers, compared to a specific commercial configuration. In addition, the availability of experimental data on the GCM allowed for the validation of the model using wind tunnel data; which includes the surface pressure coefficients and drag coefficient of the model (Storms et al. 2006). The GCM is a

1/8th scale generic class-8 tractor-trailer model that was developed by the Heavy Vehicle Drag Consortium (McCallen et al. 2004). The underbody of the tractor and the trailer were not modeled and were approximated with flat surfaces. The tractor wheel wells were also not modeled and were approximated with flat surfaces. In addition, the trailer landing gear was not modeled. This proved to be beneficial as changes in the flow field due to the underbody device can be readily identified. The trailer is 13.7 m in length at full scale while the tractor-trailer gap is a full-scale equivalent of 1.0 m. The GCM dimensions are shown in Figure 3.1.



Figure 3.1: GCM dimensions (in mm)

During this research, a few concepts were proposed to meet the objectives that were outlined earlier. The 1st device concept was composed of a combination of a ramp and straight side skirts. The ramp provides a surface for the recirculating flow at the underbody to reattach while the side skirts shield the flow from crosswinds. The 1st device concept is shown in Figure 3.2.

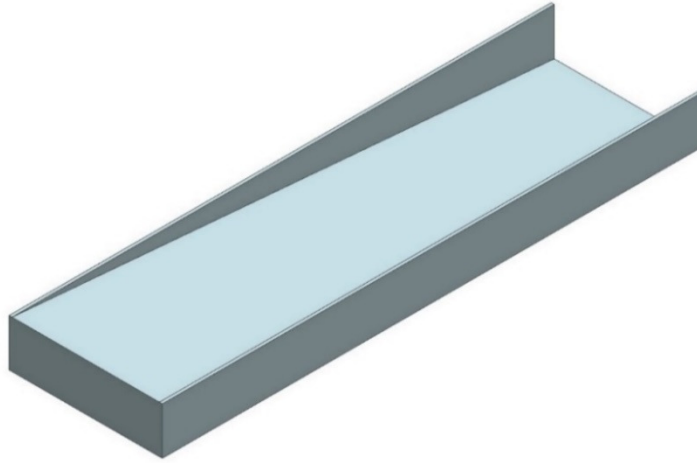


Figure 3.2: First proposed device concept

In the 2nd concept, the device was improved by adding a slanted edge between the ramp and the side skirts. This was proposed for two primary reasons; the first being to accelerate the flow velocity by decreasing the cross-sectional area of the device. By increasing the flow velocity, flow attachment can be maintained using a device with a steeper ramp; which allows for a device with a smaller footprint. The second reason is that with this design the underbody flow is diverted away from the trailer wheels. As was mentioned in the literature review, this results in further drag reduction. The 2nd concept is shown in Figure 3.3.

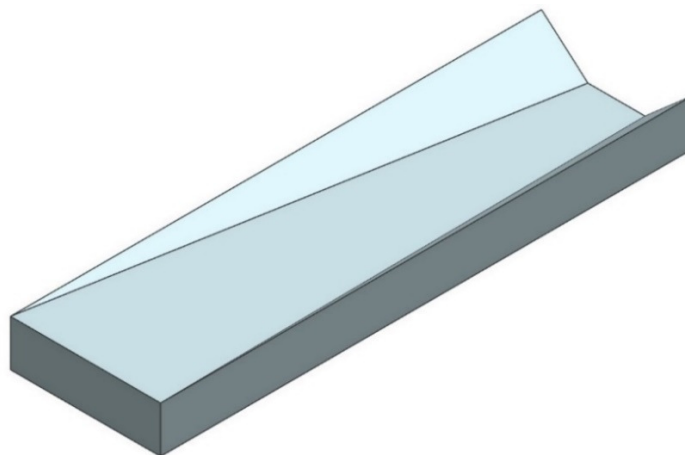


Figure 3.3: Second proposed device concept

The 3rd concept combines the functionality of both proposed concepts while decreasing the size of the device. Figure 3.4 displays the proposed concept attached to the GCM. The underbody fairing was implemented to provide the underbody flow field with a means that will guide the flow that is exiting the tractor underbody so that it can remain attached throughout the underbody of the trailer to reduce flow recirculation. On the other hand, the converging side skirt was implemented for three primary reasons. The first being that converging side skirts will prevent crosswinds from disturbing the underbody flow; providing better drag reduction. Secondly, using a converging side skirt, the underbody flow can be accelerated so that it remains attached as the ramp angles increase. Finally, the converging side skirts will prevent the underbody flow from interacting with the trailer wheels, which should theoretically reduce drag.

As this concept provided the combined features of the previously proposed concepts while having the benefits of a smaller package, it was selected for this research thesis. In addition, what differentiates this device from those in the literature is that it integrates the functionality of an underbody fairing and a side skirt in a single device. Another novelty is the ability of the device to collapse so that it can be stored flat when not required, such as during city driving or in order to clear a loading dock or a speed bump. The mechanism that will enable the collapsibility of the device will be designed so that it can be actuated using a single motor.

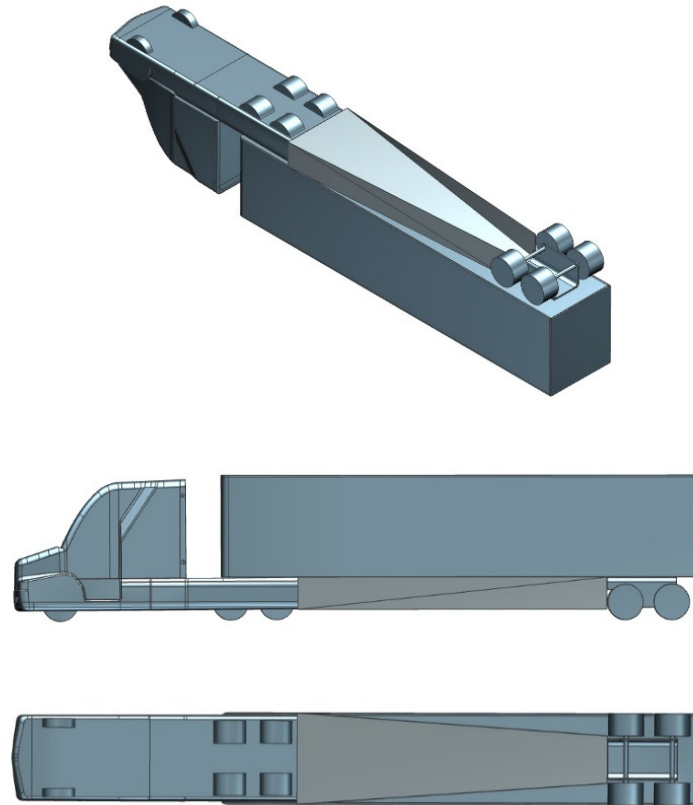
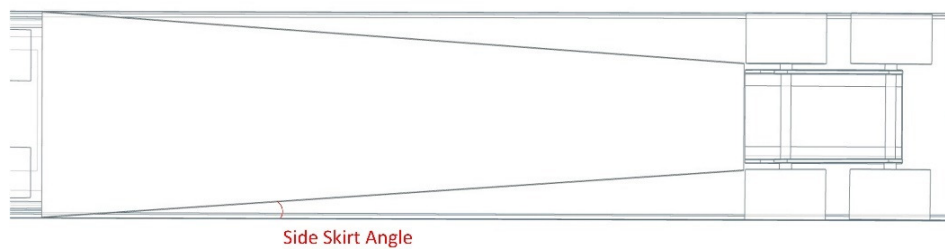


Figure 3.4: GCM with trailer underbody device shown in isometric view (top), side view (middle) and bottom view (bottom)

Preliminary studies were done to optimize the device on its own by controlling two of the device dimensions simultaneously; the ramp angle and the side skirt angle. This was done to ensure flow attachment while maintaining a flow velocity that would not negatively affect the wake region, i.e., decrease the pressure in the wake. The side skirt angle is the angle between the side skirt and the edge of the trailer (Figure 3.5a). Meanwhile, the ramp angle is the angle measured from the ramp to the side skirt (i.e. a ramp angle of zero would make the ramp parallel to the ground) (Figure 3.5b). 12 different device configurations were simulated individually, where the ramp angle was varied between four different configurations (3° , 4° , 5° and 6°) while the side skirt angle was varied between three different configurations (straight side skirt, 3° , and 4°). When testing ramp angles higher

than 6° , it was found that flow separation was evident. Meanwhile, angles lower than 3° were not tested as they hindered the ground clearance of the vehicle significantly. As for the side skirt angle, angles higher than 4 degrees caused choking in the flow while angles lower than 3 degrees did not result in a pronounced effect on the flow field when compared to the straight side skirts. It is important to note that a straight side skirt would be equivalent to having a side skirt angle of 0° . A summary of the device configurations that will be evaluated in this research thesis is shown in Table 3.1.

a)



b)

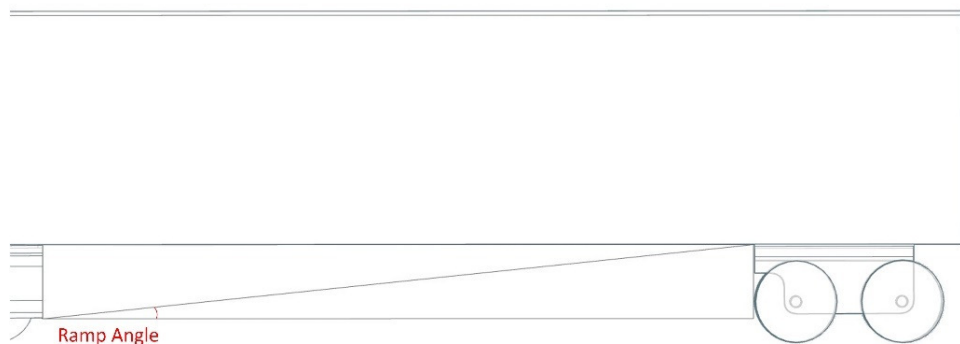


Figure 3.5: a) Bottom view of the device indicating the side skirt angle b) Side view of the device indicating the ramp angle

Table 3.1: Summary of the different configurations conducted in the preliminary study

Configuration Number	Device Description
1	Ramp 3° - Straight Side Skirt
2	Ramp 3° - Side Skirt 3°
3	Ramp 3° - Side Skirt 4°
4	Ramp 4° - Straight Side Skirt
5	Ramp 4° - Side Skirt 3°
6	Ramp 4° - Side Skirt 4°
7	Ramp 5° - Straight Side Skirt
8	Ramp 5° - Side Skirt 3°
9	Ramp 5° - Side Skirt 4°
10	Ramp 6° - Straight Side Skirt
11	Ramp 6° - Side Skirt 3°
12	Ramp 6° - Side Skirt 4°

3.2. Numerical Approach

In this section, the numerical aspects governing the fluid flow are discussed, which includes flow modeling, turbulence modeling, model setup, solver settings, grid generation and post-processing.

3.2.1. Flow Modeling

Numerical fluid flow is computed using the conservation of mass and momentum.

The conservation of mass is as follows (ANSYS 2013):

$$\frac{\partial \rho}{\partial t} + \nabla(\rho \vec{v}) = S_m \quad (3.1)$$

where S_m is the mass added to a continuous phase from a dispersed phase, such as vaporization or liquid droplets, or a user-defined source.

As the flow in this study is incompressible and the source term is not required, the continuity equation simplifies to:

$$\nabla \vec{v} = 0 \quad (3.2)$$

The conservation of momentum for a non-accelerating reference frame is as follows (Batchelor 1967)

$$\frac{\partial}{\partial t}(\rho\vec{v}) + \nabla \cdot (\rho\vec{v}\vec{v}) = -\nabla p + \nabla \cdot (\bar{\tau}) + \rho\vec{g} + \vec{F} \quad (3.3)$$

where p is the static pressure, $\bar{\tau}$ is the stress tensor, $\rho\vec{g}$ is the gravitational body force and \vec{F} is the external body forces and other model dependent source terms. The stress tensor $\bar{\tau}$ is:

$$\bar{\tau} = \mu \left[(\nabla\vec{v} + \nabla\vec{v}^T) - \frac{2}{3}\nabla \cdot \vec{v}I \right] \quad (3.4)$$

where μ is the molecular viscosity, I is the unit tensor and the second term on the right side represents the effect of volume dilation. At a low Reynold number (Mach < 0.3), the compressibility effects can be ignored and the equation for energy conservation is not required.

3.2.2. Turbulence Modeling

Directly solving the Navier-Stokes equations using Direct Numerical Simulation (DNS) requires immense computational power; making it not feasible even using the world's most powerful supercomputers. Thus, averaging the Navier-Stokes equations is done to reduce the turbulent spectrum that is explicitly computed or completely model the turbulent spectrum. For high Reynolds number external flow, the following turbulence models are applicable:

- Large Eddy Simulation (LES)
- Detached Eddy Simulation (DES)
- Reynolds Averaged Navier-Stokes (RANS)

Large Eddy Simulation (LES) turbulence model resolves the Navier-Stokes equations for turbulence structures (eddies) that are equal to or larger than the grid size while modeling the rest of eddies. Detached Eddy Simulations (DES) turbulence model offers a hybrid between the LES model and the unsteady RANS model. The LES model is deployed in the turbulent regions of the flow while the RANS model is employed at the near-wall region. Compared to the LES model, the computational requirements for the DES model is lower. Unfortunately, both turbulence models require computational power that exceeds that allocated for this research thesis. In addition, RANS based studies have been conducted on the validation of the GCM that have proved its robustness and accuracy in predicting the flow field and drag coefficient (Pointer 2004).

Reynolds Averaged Navier-Stokes (RANS) turbulence models are the most computationally economic approach to solving complex turbulent flows, as the entire turbulent spectrum is modeled. In the RANS model, the solution variables in the Navier-Stokes equation are decomposed into a mean (ensemble-averaged or a time-averaged) and a fluctuating component. The velocity components are decomposed to:

$$u_i = \bar{u}_i + u'_i \quad (3.5)$$

where \bar{u}_i is the mean velocity component and u'_i is the fluctuating velocity component. This can be also applied to other scalar quantities, such as pressure or energy such as:

$$\phi = \bar{\phi} + \phi' \quad (3.6)$$

Substituting the decomposed expressions into the instantaneous Navier-Stokes equations while taking a time average yields the ensemble-averaged continuity and

momentum equations (ANSYS 2013). These equations are referred to as the Reynolds Averaged Navier-Stokes (RANS) equations:

$$\frac{\partial \rho}{\partial t} + \frac{\partial}{\partial x_i}(\rho u_i) = 0 \quad (3.7)$$

$$\frac{\partial}{\partial t}(\rho u_i) + \frac{\partial}{\partial x_j}(\rho u_i u_j) = -\frac{\partial p}{\partial x_i} + \frac{\partial}{\partial x_j} \left[\mu \left(\frac{\partial u_i}{\partial x_j} + \frac{\partial u_j}{\partial x_i} - \frac{2}{3} \delta_{ij} \frac{\partial u_l}{\partial x_l} \right) \right] + \frac{\partial}{\partial x_j}(-\rho \bar{u}_i' \bar{u}_j') \quad (3.8)$$

The RANS equations have the same general form as the instantaneous Navier-Stokes equations with the velocities and other solution variables being time-averaged values. The effects of turbulence are represented using an additional term called the Reynolds stresses ($-\rho \bar{u}_i' \bar{u}_j'$). The Reynolds stresses need to be modeled in order to close the RANS equations due to several unknown terms in the exact equation. This is often referred to as the closure problem. A common approach to model the Reynolds stresses is the Boussinesq hypothesis (Hinze 1975):

$$-\rho \bar{u}_i' \bar{u}_j' = \mu_t \left(\frac{\partial u_i}{\partial x_j} + \frac{\partial u_j}{\partial x_i} \right) - \frac{2}{3} \left(\rho k + \mu_t \frac{\partial u_k}{\partial x_k} \right) \delta_{ij} \quad (3.9)$$

The Boussinesq hypothesis establishes a relationship between the Reynolds stresses and the mean velocity gradients, with a relatively low computational cost. This hypothesis is employed in the Spalart-Allmaras model, the $k - \varepsilon$ model and the $k - \omega$ model. The disadvantage of the Boussinesq hypothesis is that it assumes that the turbulent viscosity (μ_t) is an isotropic quantity, which is not the case. However this assumption is applicable for shear flows that only have one major turbulent shear stress, such as flows with wall boundary layers, mixing layers and jets (ANSYS 2013). Another approach to solve the Reynolds stresses is by using the Reynolds Stress Transport Models (RSM). This method

solves the transport equations for each term in the Reynolds stress tensor, which requires more computational power compared to the Boussinesq hypothesis. The RSM model offers an advantage compared to the Boussinesq hypothesis in situations where the turbulence anisotropy is dominant; such as highly swirling flows (ANSYS 2013).

Examining the turbulence models, the Spalart-Allmaras one equation model (Spalart and Allmaras 1992) is a simple model that solves a modeled transport equation for the kinematic turbulent viscosity. This model is applicable only for low-Reynolds number flows, requiring the boundary layer to be resolved at around a $y^+ \sim 1$.

In industrial CFD, the $k - \varepsilon$ models is one of the most commonly used turbulence models. The model solves two transport equations and models the Reynolds stresses using the Boussinesq hypothesis mentioned earlier. There are three different $k - \varepsilon$ models, the standard $k - \varepsilon$, the ReNormalization Group (RNG) $k - \varepsilon$ and the Realizable $k - \varepsilon$. The major difference between the three models are as follows (ANSYS 2013):

- The turbulent viscosity calculation method
- ε equation generation and destruction terms
- Prandtl numbers used in the diffusion of k and ε

The standard $k - \varepsilon$ model (Launder and Spalding 1972) is based on the model transport equations for the turbulence kinetic energy (k) and its dissipation rate (ε). The model neglects the effects of molecular viscosity and assumes that the flow is fully turbulent, thus this model is only applicable for fully turbulent flows. The standard $k - \varepsilon$ model has been improved over the years to account for its strengths and weaknesses. The

RNG $k - \varepsilon$ model improves on the standard $k - \varepsilon$ model with the following refinements (ANSYS 2013):

- Improves the accuracy of rapidly strained flows
- Enhances the accuracy of swirling flows
- Provides an analytical formula for the turbulent Prandtl numbers, compared to the user-specified constant values used in the standard $k - \varepsilon$ model
- RNG model provides a differential formula for the effective viscosity accounting for low-Reynolds number effects.

As for the realizable $k - \varepsilon$ model, it is different from standard $k - \varepsilon$ model in the following ways (ANSYS 2013):

- It contains an alternative formulation for the turbulent viscosity
- The dissipation rate (ε) transport equation is derived from the exact equation for the transports of the mean-square vorticity fluctuation.

On the other hand, the $k - \omega$ models use a transport equation for specific dissipation rate (ω) instead of the dissipation rate (ε). The advantages for using the ω -equation is that it offers a y^+ -insensitive wall treatment. The standard $k - \omega$ model (Wilcox 1993) is sensitive to the freestream values of k and ω outside the shear layer; thus it is not recommended in ANSYS Fluent (ANSYS 2017b). The SST $k - \omega$ model is designed to avoid this freestream sensitivity. The shear stress transport (SST) $k - \omega$ model (Menter 1994) combines both the standard $k - \omega$ model and the high Reynolds number version of the $k - \varepsilon$. The standard $k - \omega$ model is applied in the inner region of the boundary layer while gradually applying the high Reynolds number version of the $k - \varepsilon$ in

the outer region of the boundary layer. This allows the SST $k - \omega$ model be accurate and reliable for a wide class of flows and the reason behind its wide usage in aerodynamic flows. The transport equations for the SST $k - \omega$ model are as follows:

$$\frac{\partial}{\partial t}(\rho k) + \frac{\partial}{\partial x_i}(\rho k u_i) = \frac{\partial}{\partial x_j} \left(\Gamma_k \frac{\partial k}{\partial x_j} \right) + G_k - Y_k + S_k \quad (3.10)$$

$$\frac{\partial}{\partial t}(\rho \omega) + \frac{\partial}{\partial x_j}(\rho \omega u_j) = \frac{\partial}{\partial x_j} \left(\Gamma_\omega \frac{\partial \omega}{\partial x_j} \right) + G_\omega - Y_\omega + D_\omega + S_\omega \quad (3.11)$$

Where G_k is the production of turbulence kinetic energy, G_ω is the generation of ω , Γ_k and Γ_ω are the effective diffusivity of k and ω , Y_k and Y_ω represent the dissipation due to turbulence of k and ω , D_ω is the cross-diffusion term and finally S_k and S_ω are user defined source terms.

Due to the improved behavior with separating flow and adverse pressure gradients compared to the other turbulence models, the $k-\omega$ SST model (Menter 1993) was selected in conducting this research. In addition, a previous study conducted by Pointer (Pointer 2004) demonstrated that the $k-\omega$ SST turbulence model displayed the least amount of error (0.8%) compared to other turbulence models in predicting the drag coefficient of the GCM model with a width based Reynolds number similar to the one used in this study.

3.2.3. Wall Treatment

The presence of walls significantly affects turbulent flows. Other than the no-slip condition affecting the mean velocity field, viscous damping and kinematic blocking affect the turbulence properties. The turbulence boundary layer is subdivided into the following three domains:

- Viscous sublayer
- Buffer layer or blending region
- Fully turbulent region or log-law layer

The viscous sublayer is the innermost layer, where the effects of the molecular viscosity are dominant and effects of turbulence are insignificant. After this region comes the buffer layer, where the molecular viscosity and turbulence effects are approximately equal. As for the outer layer, which is referred to as the log-law layer, the effects of turbulence play a major role while the molecular viscosity effects are negligible.

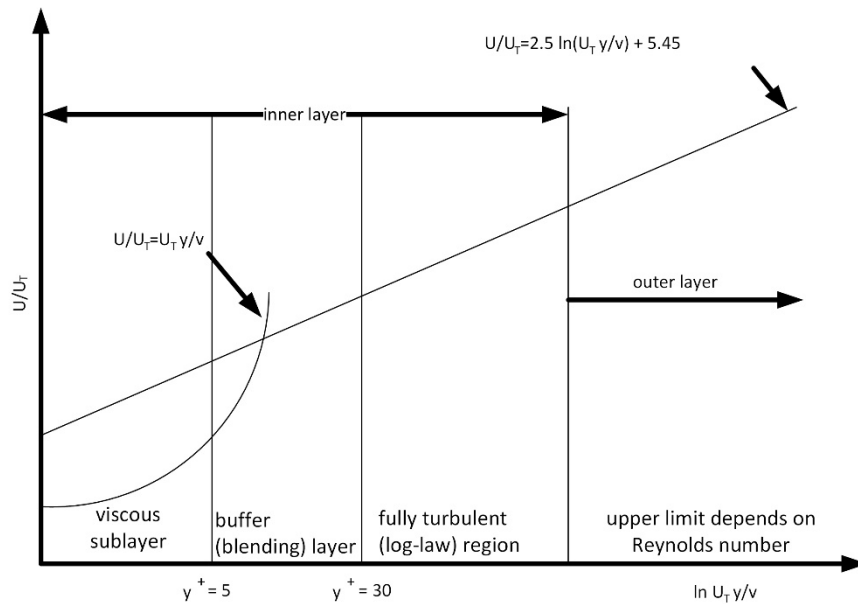


Figure 3.6: Subdivisions of the Near-Wall Region (adapted from ANSYS 2013)

These three regions can be defined using the friction velocity (u_T) and the non-dimensional wall distance (y^+). The friction velocity and the non-dimensional wall distance are as follows:

$$u_T = \sqrt{\frac{\tau_w}{\rho}} \quad (3.12)$$

$$y^+ = u_T y \frac{\rho}{\mu} = \frac{u_T y}{\nu} \quad (3.13)$$

These three subdivisions of the turbulent boundary layer are referred to as the “law of the wall”. As shown in Figure 3.6, the three layers are bounded by the following y^+ values:

- Viscous sub-layer: $0 < y^+ \leq 5$
- Buffer (blending) layer: $5 < y^+ < 30$
- Fully turbulent (log-law) region: $y^+ \geq 30$

ANSYS Fluent has two approaches for wall modeling based on these subdivisions, wall functions and near wall model. For wall functions, the viscous sublayer and buffer layer are modeled. As for the near-wall model, the turbulence model is modified to enable the viscous sublayer and the buffer layer to be resolved all the way to the wall. Figure 3.7 below summarizes the differences between both wall modeling approaches.

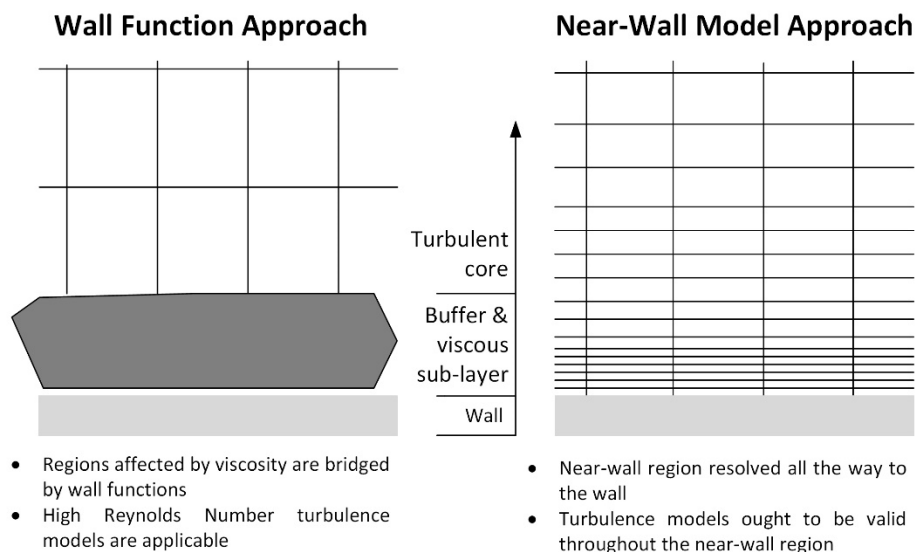


Figure 3.7: Difference between the Wall Function approach and the Near-Wall Model approach in modeling the near-wall region (ANSYS 2013)

As previously mentioned, the $k-\omega$ SST turbulence model (Menter 1993) was chosen to conduct this research. The $k-\omega$ SST turbulence model integrates the Enhanced Wall Treatment ω -equation (EWT- ω). This method formulates the law of the wall as a single wall law using a blending function to combine the laminar and turbulent law of the wall (Kader 1981).

3.2.4. Model Setup

3.2.4.1. Preliminary Study Setup

As previously mentioned, 12 different device configurations were evaluated and optimized in the preliminary study. These underbody devices were modeled as channels in order to reduce the computational time required to evaluate the different configurations while providing results that rank the proposed configuration in terms of defined metrics. The metrics used to rate the proposed configurations were average outlet velocity, mass flow rate, and outlet pressure. The channel modeled the underbody of the tractor as well as the device itself. As 12 different configurations have been evaluated, each domain had a different structure to mimic the interior of the proposed device. For example, considering device configuration #2 in the preliminary study (Ramp 6° - Side Skirt 4°), the region where the channel is modeled is highlighted in red as shown in Figure 3.8. The first section of the domain models the tractor underbody of the GCM (Figure 3.9). The tractor wheels were eliminated for simplicity as the primary goal was to evaluate the device concepts and determine which ones had the highest drag reduction potential. The inlet dimensions of the channel as well as the length were the same for all 12 configurations as these factors were limited by the underbody dimensions of the GCM. The total length of the channel was 1.97 m with the tractor underbody section being 1.02 m in length. The inlet is 0.323 m in width

and 0.038 m in height. The channel domain also accounted for the ground clearance of the vehicle in order to provide a more realistic approximation of the flow in the device.

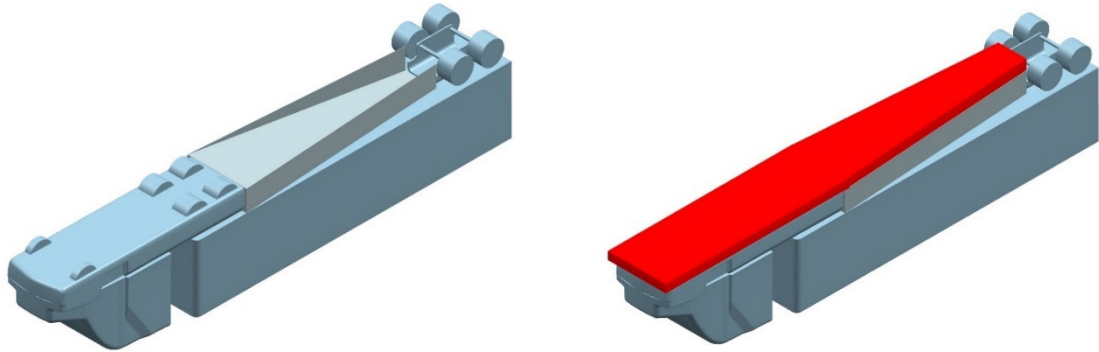


Figure 3.8: GCM with device configuration #2 (Ramp 6° - Side Skirt 4°) (left) and the channel location highlighted in red (right)

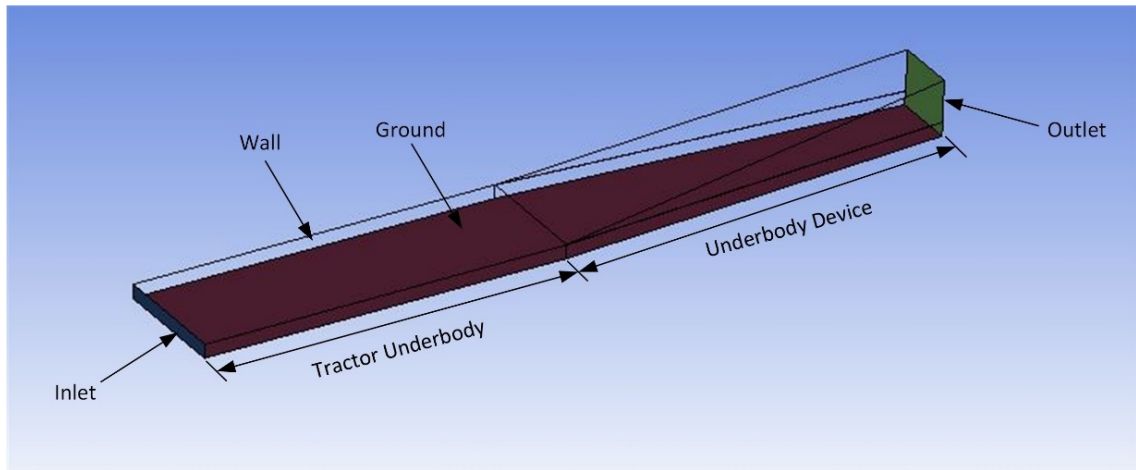


Figure 3.9: Domain of device configuration #2 in the preliminary study

The simulations were performed at a uniform inlet velocity of 51.45 m/s (185 km/h). This corresponds to a width-based Reynolds number of $Re = 1.1 \times 10^6$. The inlet turbulence intensity was set to 5% (Lauwers 2009) and a no-slip stationary plane boundary condition was set for the domain ground. A zero-pressure gradient was specified for the outlet condition. These boundary conditions were set to be identical to the GCM with Underbody

Device Setup boundary conditions in order to maintain consistency throughout this research.

3.2.4.2. *GCM with Underbody Device Setup*

The devices from the preliminary study that were found to have the highest drag reduction potential were simulated on the GCM model. In addition, the GCM was simulated to set up a baseline for the drag reduction devices. The GCM has a height of 0.48 m, a width of 0.32 and a length of 2.46 m. The computational domain used to evaluate the GCM was 2.17 m × 3.05 m × 9.84 m. The model has a frontal area (A) of 0.164 m² which resulted in a blockage of 2.5%. The computation domain is shown in Figure 3.10. West and Apelt (West and Apelt 1982) have reported that the effects of a blockage ratio less than 6% are negligible on the measured pressure distribution and the drag coefficient. Meanwhile, Leuschen and Mebarki (Leuschen and Mébarki 2012) reported that a blockage ratio less than 4% requires a correction to the drag coefficient in the order of 0.03 to 0.05. However, the relative improvement of the proposed device is not influenced by the blockage ratio effects, as the drag coefficient of the baseline model and the model with the device are equally affected by their identical blockage ratios. Additionally, this blockage ratio was specifically chosen to mimic the blockage used by an experimental study conducted on the GCM (Storms et al. 2004, 2006) that will be later used for validation.

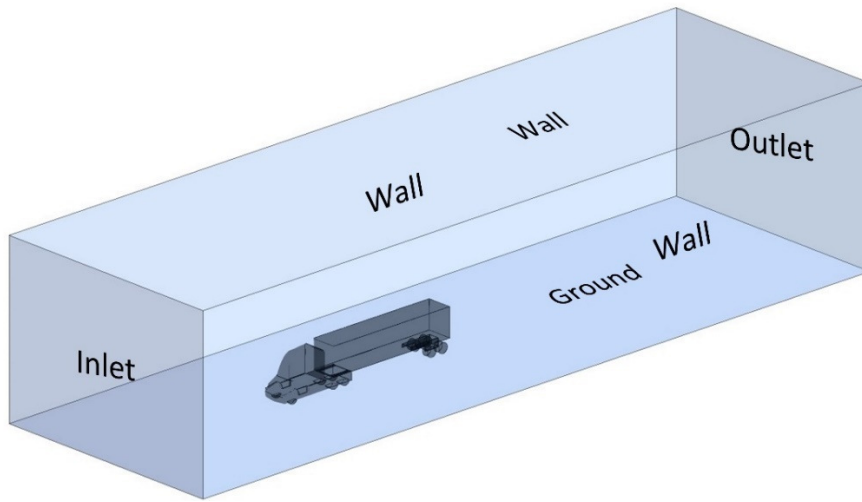


Figure 3.10: Computational domain

The simulations were performed at a uniform inlet velocity of 51.45 m/s (185 km/h) at zero yaw. This corresponds to a width-based Reynolds number of $Re = 1.1 \times 10^6$. The inlet turbulence intensity was set to 5% (Lauwers 2009) and a no-slip stationary plane boundary condition was set for the domain ground. During this study, the influence of the turbulence intensity was simulated up to 10% with no profound effect on the drag coefficient of the model. A zero-pressure gradient was specified for the outlet condition. This Reynolds number along with the domain ground condition was used specifically in order to validate the baseline model with NASA’s experimental data (Storms et al. 2006). A summary of the boundary conditions is shown in Table 3.2.

Table 3.2: Boundary conditions

Surface	Boundary Condition	Additional Information
Inlet	Constant velocity inlet	$V_u = 51.45 \text{ m/s}$, $I = 5\%$
Outlet	Pressure outlet	$P_{outlet} = 0$
Left Wall	Wall	-
Right Wall	Wall	-
Top Wall	Wall	-
Ground	Wall	-
GCM	Wall	-

3.2.5. Grid Generation

In order to create the computational domain used for this study, the commercial grid generation software ANSYS Meshing was utilized for its proven robustness and its compatibility with ANSYS Fluent. Building a grid can be a tedious task, as many grid properties are varied during grid refinement process in order to reach a grid independent solution. In addition, the grid has to be regenerated if a different geometry is analyzed which can be a time-consuming process. Thus, a systematic approach has been proposed in this section to generate and refine the grid accordingly.

3.2.5.1. *Boundary layer grid*

In order to correctly capture the flow structure around the boundary layer, the inflation layer has to be correctly calculated. Three primary parameters govern the inflation layer, first aspect ratio, geometric growth rate and a number of layers. The first aspect ratio allows the prisms to be extruded at a prism height that is proportional to the base triangle on the vehicle. In order to achieve good characteristics, the triangle size has to vary smoothly. In addition, each succeeding prism layer must increase in height at a constant rate. This is referred to as the geometric growth rate. The total number of layers is the number of inflation layers calculated before the mesh switches to tetrahedral. In essence, the combination of these three parameters should allow for a good transition between the prism layer and the tetrahedral region. This is key to achieve an inflation layer that satisfies the numerical requirements as a large cell-gradient between the prism layer and the tetrahedral layer may lead to numerical diffusion.

The inflation layer of the model was generated to meet the recommended best practice for vehicle surfaces (Lanfrit 2005). The inflation layer was set to have a first aspect

ratio of 5, a geometric growth rate of 1.2 and a total number of layers of 5. Figure 3.11 shows an overview of the inflation layer around the domain.

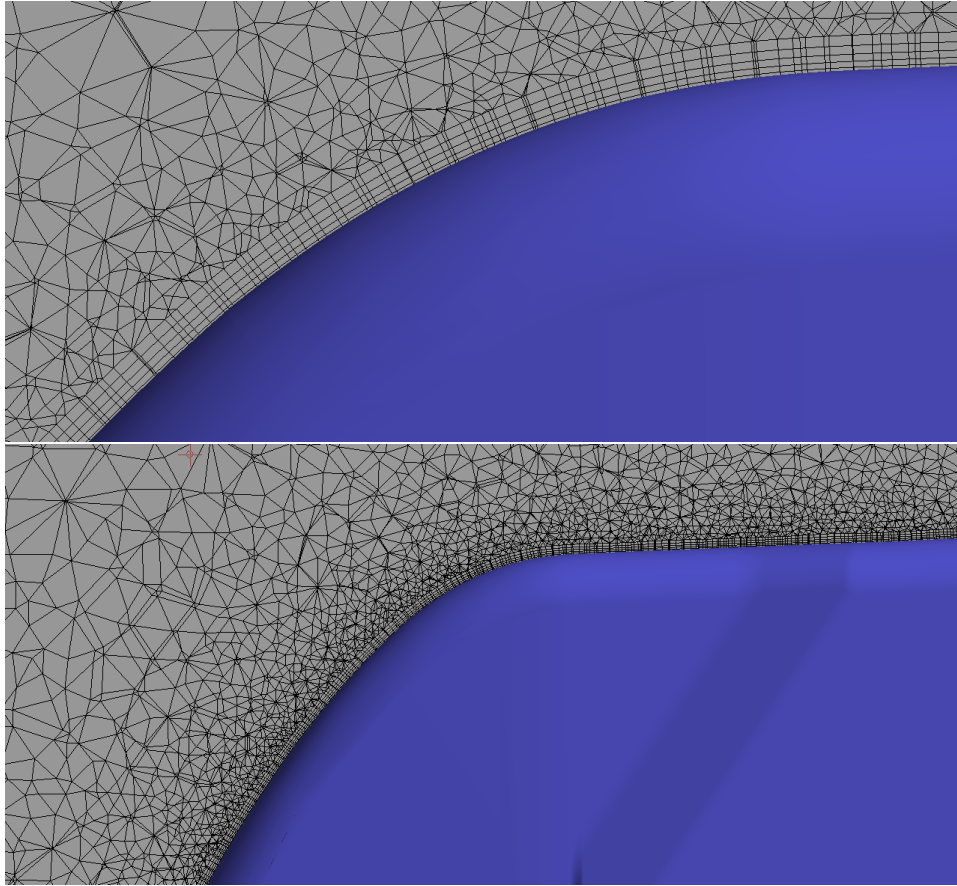


Figure 3.11: Close up of the inflation layer at the tractor face

As the surface mesh must be as smooth as possible in order to allow the prism layers to be extruded from the surface of the model, great emphasis has been placed on the surface mesh refinement. The surface mesh was set at 5 mm initially to avoid any sharp prisms; which are a source of highly skewed cells. The surface mesh was refined later during the grid independence study. Figure 3.12 below shows the surface mesh details for the GCM.

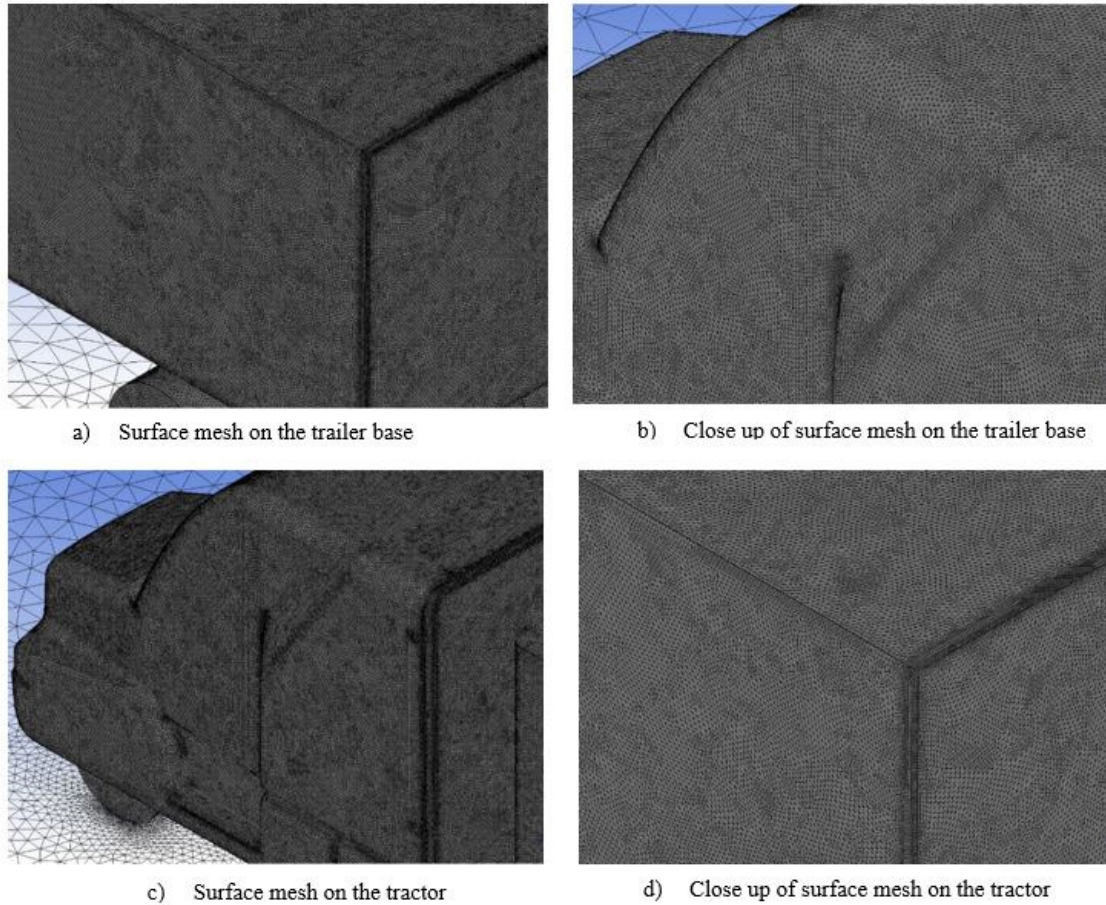


Figure 3.12: Overview of the surface mesh

3.2.5.2. Unstructured grid

In order to better capture the flow structure at the underbody and wake regions and subsequently the changes that will be introduced with the addition of the device, three refinement regions were created around the vehicle. This strategy is more time consuming than mesh adaptation but provides very accurate results as a constant size of elements can be applied to each refinement box. The strategy is often referred to as the control strategy and is recommended by ANSYS (Lanfrit 2005). The vehicle itself was enclosed in a refinement box that included two smaller refinement regions that covered the underbody and the wake of the vehicle. These regions were set to maintain a minimum cell size that

was not dependent on the global refinement. These refinement regions are shown in Figure 3.13. The vehicle refinement is the largest refinement region around the vehicle, the wake refinement being the region directly behind the back of the trailer and the underbody refinement being the region that encloses the full underbody of the vehicle.

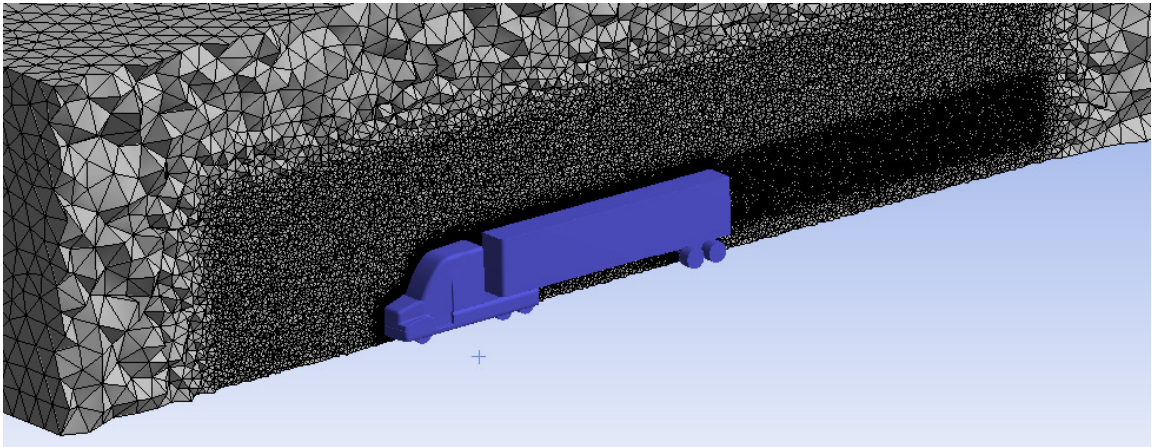


Figure 3.13: Computational domain refinement regions

The vehicle refinement region was set as half the domain dimensions, which is $1.14 \text{ m} \times 1.56 \text{ m} \times 4.92 \text{ m}$. The element size in this refinement region was set to 30 mm. The wake refinement region was set to have the same width and height of the vehicle base, which is $w = 0.323$ and $h = 0.477 \text{ m}$ respectively. The length of wake refinement region was set to be equal to the length of the GCM. The element size was set to 15 mm. As for the underbody refinement region, the region was set to completely enclose the underbody of the vehicle with an element size of 5 mm. These refinement region dimensions were based on the recommended best practice to control volume mesh near a vehicle (Lanfrit 2005). Figure 3.14 shows an overview of the computational domain at different grid slices.

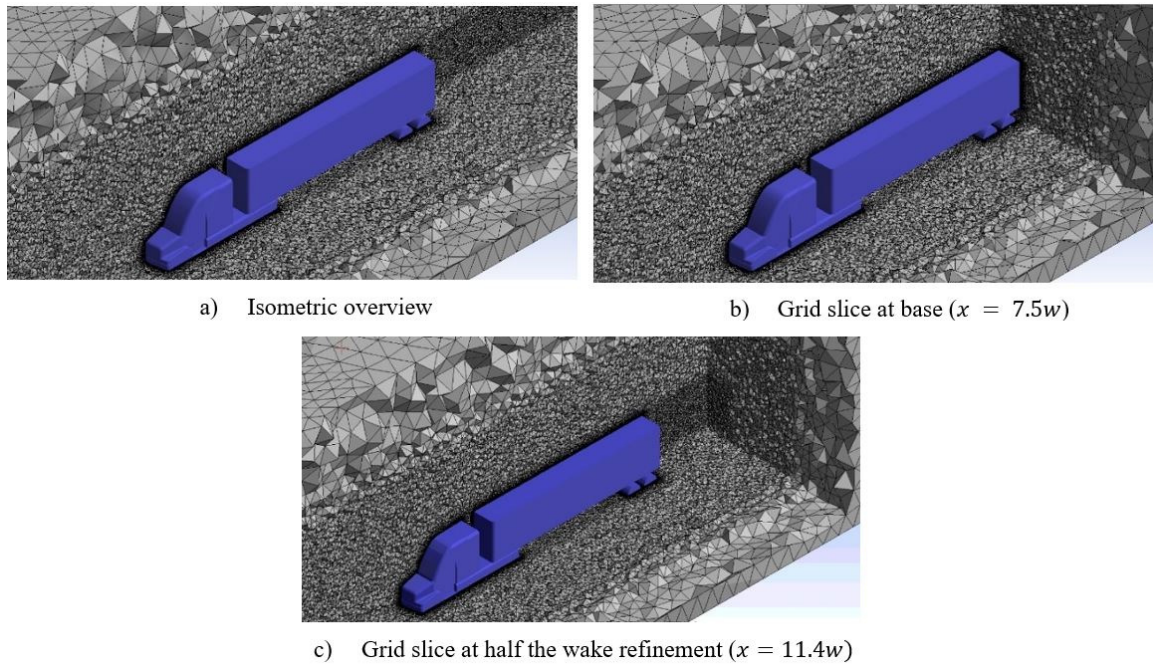


Figure 3.14: Overview of the computational domain

3.2.5.3. Grid Independence

The purpose of a grid independence study is critical; as it determines if the simulation results are influenced by mesh refinement. The choice of grid size depends on the compromise between computational power and the required accuracy, as a finer grid requires more computing time. In addition, finer grids require lower under-relaxation factors to ensure a stable solution. These factors will be discussed in the solver settings section.

In order to ensure grid independence, the baseline GCM model was simulated with three different grids, which were compared with the experimental drag coefficient. The three grid resolutions were 12.8×10^6 , 20.8×10^6 and 25.7×10^6 elements. The drag coefficient converged at approximately 6,000 iterations for all three cases in addition to the continuity and momentum residuals. As the grid resolution was further refined, the relative differences between the predicted and experimental drag coefficients were decreasing,

which indicated a trend towards convergence. For example, the predicted drag coefficient was 0.407 and 0.404 respectively for the grid with the resolution of 20.8×10^6 and 25.7×10^6 elements. These are approximately 2.3% and 1.6% higher than the drag coefficient obtained experimentally. The results of the grid independence study are shown in Table 3.3. Although the results of the grid with the resolution of 25.7×10^6 elements was about 0.7% better than that of the 20.8×10^6 grid, it was decided to use the latter for the rest of the study to save time. This is because this study is focused on optimizing the underbody device.

Table 3.3: Summary of the grid independence study for the baseline GCM.

Vehicle Cell Size (mm)	Grid Resolution	Predicted Drag Coefficient	Error in Drag Coefficient
5	12.8×10^6	0.420 +/- 0.005	5.6 %
3	20.8×10^6	0.407 +/- 0.004	2.3 %
2.5	25.7×10^6	0.404 +/- 0.002	1.6 %

3.2.6. Solver Settings

As previously mentioned, the RANS based $k-\omega$ SST turbulence model (Menter 1993) in ANSYS Fluent was used in conducting this study. A previous study conducted by Pointer (Pointer 2004) demonstrated that the $k-\omega$ SST turbulence model displayed the least amount of error (0.8%) compared to other turbulence models in predicting the drag coefficient of the GCM model with a width based Reynolds number similar to the one used in this study. The $k-\omega$ SST turbulence model requires the y^+ values around the surface of the vehicle to fall between 20 and 200 (Pointer 2004). As shown in Figure 3.15, the y^+ values fall within the required range for the turbulence model used.

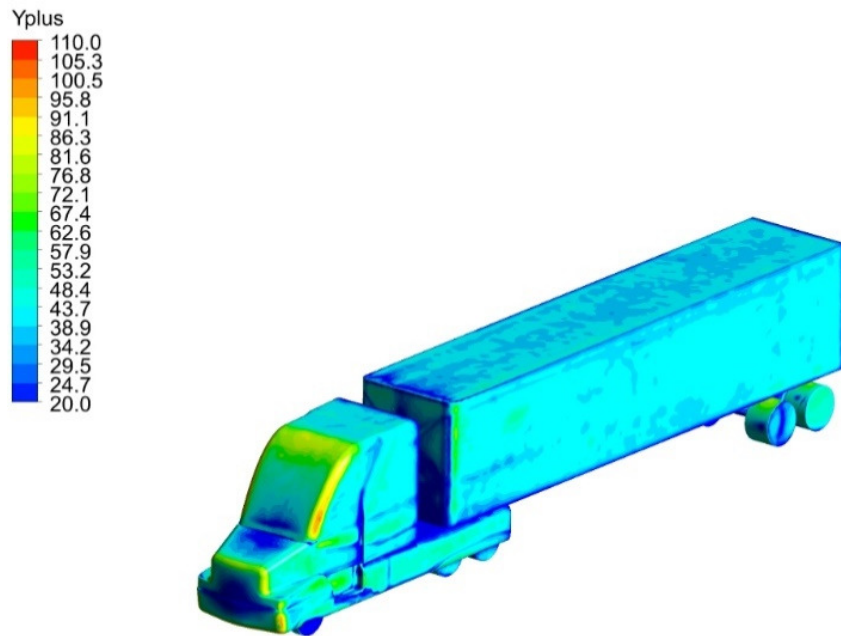


Figure 3.15: y^+ values along the surface of the baseline GCM.

All simulations were conducted using a steady state solver employing the SIMPLE algorithm. Pressure, momentum, turbulent kinetic energy and the specific dissipation rate were all evaluated using the second-order upwind scheme. In order to improve the convergence and stability of the solver, different under relaxation solver settings were implemented as recommended by ANSYS. These settings are summarized in Table 3.4.

Table 3.4: Summarized under relaxation solver settings

Pressure	0.2
Density	1
Body Forces	1
Momentum	0.5
Turbulence Kinetic Energy	0.5
Specific Dissipation Rate	0.5
Turbulent Viscosity	1

3.2.7. Post Processing

The post-processing conducted in this research thesis was done using ANSYS CFD-Post. Different contours, profiles, iso-surfaces, and metrics were calculated in order to evaluate the changes in the flow influenced by the device. Turbulence Kinetic Energy (TKE) is the mean kinetic energy per unit mass of the turbulent fluctuations in a turbulent flow and is calculated using the following equation:

$$k = \frac{1}{2} (\overline{u'^2} + \overline{v'^2} + \overline{w'^2}) \quad (3.14)$$

Where u' , v' and w' are the velocity fluctuations in the x, y and z direction respectively. The unit for TKE is $\frac{m^2}{s^2}$. The pressure coefficient was calculated using the following equation:

$$C_p = \frac{P - P_{ref}}{\frac{1}{2} \rho_{ref} v_{ref}^2} \quad (3.15)$$

Where P is the static pressure at the measure point, P_{ref} is the static pressure at the freestream, ρ_{ref} is the fluid density in the freestream and v_{ref} being the freestream fluid velocity.

The mass flow rate was calculated using the mass flow function, which computes the mass flow through a specified 2D location. The function formula is shown below:

$$[< phase >.]massFlow()@ < Location > \quad (3.16)$$

Where [*phase*] is a prefix that applies for multiphase flow and is not required for single-phase flows, *Location* being the location of the 2D plane where the mass flow rate is calculated.

As for the average velocity and average pressure, the areaAve function is employed to calculate the area-weighted average of these variables. This function takes into account the mesh element size as without the area weighting function the average of the variable would be biased toward regions of high mesh density.

In order to calculate the drag coefficient, a drag monitor was set up during the solution to monitor the drag convergence. ANSYS Fluent calculates the drag of a body by using the reference values set up by the user. The reference values include the area and the length. In this case, the area was set as the frontal area of the GCM which was $A = 0.164 \text{ m}^2$. The length refers to the characteristic length of the model which in this case was the length of the GCM, $L = 2.46 \text{ m}$. After the simulations have converged, the drag coefficient was averaged over the last 1000 iterations of the simulation.

3.3. Validation

A primary reason for the selection of the GCM model over other generic models or commercial tractor-trailer combinations was the availability of extensive experimental results conducted by the NASA Ames Research Centre on the model (Storms et al. 2006). The experimental data includes the drag coefficient of the different configurations tested for the GCM model, the pressure coefficient around the centreline of the baseline model, three-component particle image velocimetry as well as force and moment measurements. In order to validate the simulations conducted in this study on the GCM model, a drag coefficient monitor was set up in ANSYS Fluent to monitor the overall drag coefficient of the vehicle which was conducted in parallel with the residual monitoring. This drag coefficient was then compared to the experimental drag coefficient whilst conducting the grid independence study. Then, the pressure coefficient along the centreline of the vehicle

was extracted from the baseline simulation in order to validate it with the experimental pressure coefficient.

3.4. Uncertainty and Error Analysis

According to NASA (NASA 2008), error in computational fluid dynamics simulations can be classified into two primary sections, acknowledged error and unacknowledged error. Acknowledged errors are errors that have a set of established procedures to find and minimize them. Acknowledged errors are generally grouped into the following four sections:

1. Physical approximation error
2. Computer round-off error
3. Iterative convergence error
4. Discretization error

Physical approximation errors occur due to simplification of the simulated model or the uncertainty in the formulation of the model. According to Mehta (Mehta 1998), the sources of uncertainty in physical models can be due to the following:

1. The phenomenon that is not completely understood
2. Parameters that are used in the model are known but still have some degree of uncertainty
3. The models used are simplified, introducing sources of uncertainty
4. Validating the model with experimental data is not possible or to some degree incomplete

The physical approximation errors in this study are minimized by validating the model used with experimental data that were provided by Storms (Storms et al. 2006, 2004)

and the numerical data provided by Pointer (Pointer 2004). As the GCM has not been simplified in any way when compared to the GCM used for the experimental study (Storms et al. 2006, 2004), this source of uncertainty is minimized.

On the other hand, computer round-off error is due to the accuracy in which the computer stores the numerical data. With the advanced computing power available, this error is considered insignificant compared to the rest of the errors. This error is minimized in this study by conducting the simulations using double-precision, which increases the significant digits carried during calculations from 7 (single-precision) to 15.

Discretization errors are the most important as they are dependent on the quality of the grid. These errors occur due to the representation of the governing flow as algebraic expressions in the discrete domain space. A grid convergence study is an approach often used to determine the level of discretization error existing in a simulation. As the grid is refined, the number of grid points increases while the discretization error approaches zero. This is called grid convergence.

As mentioned previously, a grid independence study was conducted in this study to minimize the discretization error. In the grid independence study, the drag coefficient of the model was monitored and compared to the available experimental drag coefficient. In addition, the pressure distribution around the model was compared to the experimental pressure distribution. For numerical studies where experimental data is not available or applicable, a number of methods have been proposed to estimate the error on the grid convergence of a solution. The Grid Convergence Index (GCI) was suggested by Roache (Roache 1994) to quantify the uncertainty of the grid convergence. The method approximates results that would be achieved if the grid was doubled using a second-order

method. The second-order method relates the results from any grid refinement test to achieve this approximation.

On the other hand, unacknowledged errors are errors with no established procedures to find and minimize them. These errors are generally split into two sections, computer programming error, and usage error. Computer programming errors are errors in the programming code in the computational fluid dynamics suite used. These errors are usually discovered by the programmers and fixed through updates. Usage errors are due to incorrect usages of the CFD software, by specifying incorrect models or inputs. These errors are minimized through experience conducting simulations and training.

3.5. Design of Active Mechanism

3.5.1. Introduction

Having achieved an optimal shape for the device, the next thing was to make the device active for the reasons mentioned earlier. To this end, a collapsible mechanism was developed to enable the storage of the device when not required. In addition, the mechanism was also developed to eliminate parasitic drag when not in use (i.e. low-speed driving). The collapsibility also allows the device to clear road protrusions such as loading docks and speed bumps which otherwise would damage any underbody device. As previously mentioned, the underbody devices currently available in the literature tend to collect snow in countries with colder climates. Truck drivers then have to clear the accumulated snow before entering weight stations. The collapsible mechanism mitigates this issue as the device collapses into a flat position, preventing any snow or ice accumulation. The device was designed so that it can be both actively or manually controlled.

During normal use, the device would deploy at set speeds (i.e. highway speeds) in order to reduce drag. If the vehicle slows down, the device automatically collapses in order to eliminate any parasitic drag it might cause. In addition, it provides a safeguard from damaging the device if the vehicle maneuvers any road protrusions. The driver of the vehicle can also manually control the device when necessary.

3.5.2. Design Considerations

Energy efficiency and ease of use were two primary design objectives or considerations of the active mechanism. Maximizing the energy efficiency of the mechanism is critical to achieving optimal energy savings. Thus, it was set out that the active mechanism will be operated using a single motor in order to save energy. Additionally, the mechanism will only require the motor during collapsing but must be deployed using its weight and gravity. This was considered the best way to achieve energy efficiency for the active mechanism. The choice of using an electric motor over a hydraulic system was primarily to allow the device to be a stand-alone package that can be applied to any tractor-trailer with minimum modification. In addition, tractor-trailers do not usually have a hydraulic system as these systems are generally on heavy vehicles that have moving trailers; such as dump trucks. Thus, the device would have to include its stand-alone hydraulic system which will make it costly and heavy compared to using an electric motor.

In terms of ease of use, the design will require minimal driver involvement as it will be actively deployed when the vehicle reaches highway speed. Also, the device will collapse once the vehicle slows down. This will significantly reduce the potential of the device getting damaged. In addition, this allows the device to be future proof as it can be

applied to autonomous heavy vehicles. The goal is to achieve a simple design that meets the design requirements while maintaining energy efficiency and ease of use.

Chapter 4 : Results and Discussion

In this chapter, the results of this research are summarized into three sections; preliminary results, baseline configuration and detailed results. The first section presents the preliminary study conducted to evaluate the proposed device concepts. In the second section, the baseline configuration is validated as well as discussing the flow structure around the model. In the third section, the concepts that are proven in the preliminary study are simulated and evaluated on the GCM to determine how they influence the flow around the vehicle as well as the drag reduction. Finally, the active mechanism designed to allow for the collapsibility of the device is discussed in section four.

4.1. Preliminary Results

As previously mentioned, the preliminary study was conducted using a similar CFD code to what was used in this study. Each device configuration was simulated as a channel. The channel was modeled based on the interior of the proposed device with different side skirt and ramp angles. These combinations resulted in 12 different device configurations that were evaluated based on the average outlet velocity, mass flow rate and the average outlet pressure of the device.

4.1.1. Baseline Channel

In order to set up a baseline for the 12 device configurations, a channel was modeled to mimic the underbody of the GCM. The channel was split into two sections, the first section represented the underbody of the tractor, while the second section represented the underbody of the trailer. The first section spanned between the channel entrance and the step, while the second section was between the step and the channel exit. These two sections apply to the other 12 configurations as well. From hereafter, the first section will be referred

to as the tractor underbody section while the second section will be referred to as the trailer underbody section.

As shown in Figure 4.1, the flow is comprised of a large recirculation zone that extends throughout the trailer underbody section of the channel; evident by the negative flow velocity due to flow separation. This recirculation zone is caused by the flow separating off the edge of the tractor underbody section. This recirculation region is responsible for the low-pressure zone in the channel as shown in Figure 4.2. The low-pressure zone is comparable to the underbody recirculation zone discussed previously in the literature review; which is a result of the underbody flow separating over the trailing edge of the tractor. The average outlet velocity of the flow exiting the channel is 7.77 m/s and the mass flow rate is 0.36 kg/s. This low flow velocity is mainly due to the flow recirculation caused by the separation from the tractor underbody section of the channel. It is important to note that these values are measured through a plane that does not cover the tractor underbody ground clearance.

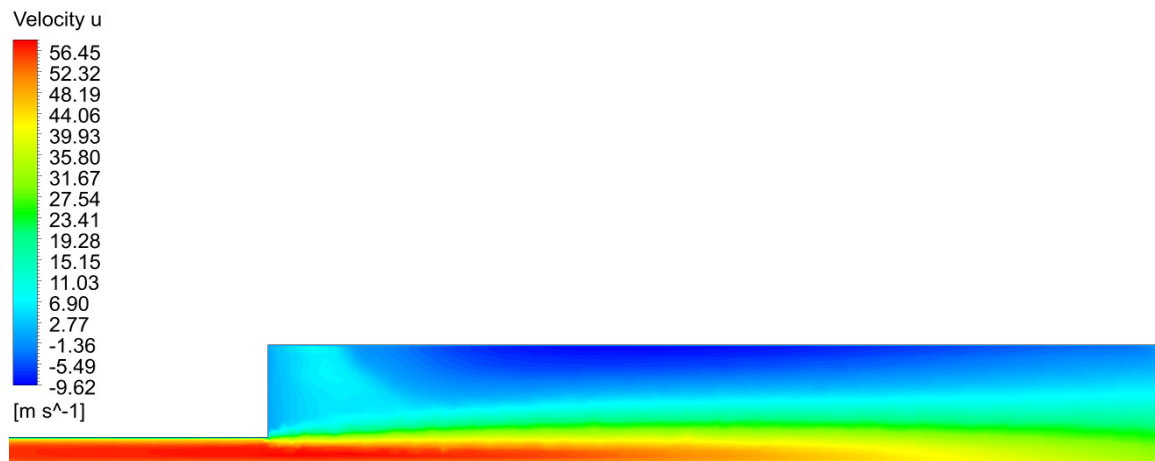


Figure 4.1: Velocity contour at the centerline of the baseline channel



Figure 4.2: Pressure contour at the centerline of the baseline channel

4.1.2. Channel Optimization

In this section, the 12 device configurations are examined and assessed in terms of average outlet velocity, mass flow rate, and outlet pressure. In addition, the velocity contours for each configuration are inspected for flow separation. A high mass flow rate through the channel implies that more of the bulk flow is attaching to the device and not recirculating at the underbody. Meanwhile, a low outlet pressure would adversely affect the pressure in the wake of the vehicle. Additionally, velocity contours along with the average outlet velocity aids in detecting flow separation at different configurations and how they affect the flow. Based on this background, the top two performing device configurations will be selected. These two device configurations will be then modeled and simulated on the GCM model to determine their effects on drag and the flow structure around the model.

The average outlet velocity of the 12 device configurations discussed in this preliminary study is summarized in Figure 4.3. The highest two configurations were configuration #3 (Ramp 3° - Side Skirt 4°) and configuration #6 (Ramp 4° - Side Skirt 4°)

with an average outlet velocity of 36.1 m/s and 29.8 m/s respectively. As for the mass flow rate, the highest two configurations were configuration #12 (Ramp 6° - Side Skirt 4°) and configuration #9 (Ramp 5° - Side Skirt 4°) with a mass flow rate of 0.50 kg/s and 0.49 kg/s respectively. Configurations 7 and 10 displayed flow separation and recirculation which explains their relatively low average outlet velocities. Both of these configurations were then eliminated. A detailed analysis of this preliminary study can be found in Appendix I. A summary of all the results is shown in Table 1.

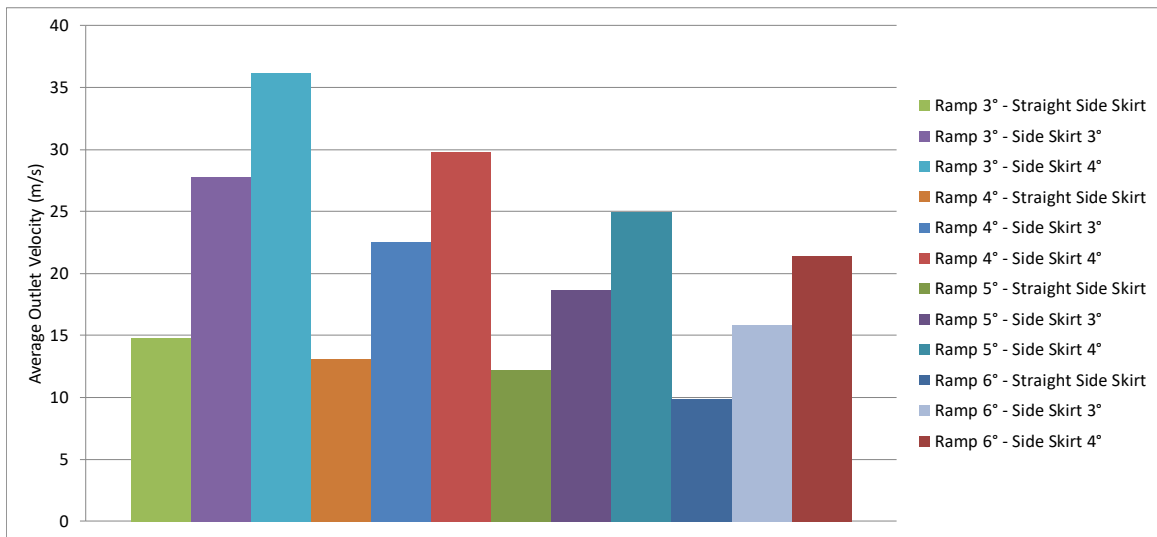


Figure 4.3: Comparison between the average outlet velocity of all 12 device configurations

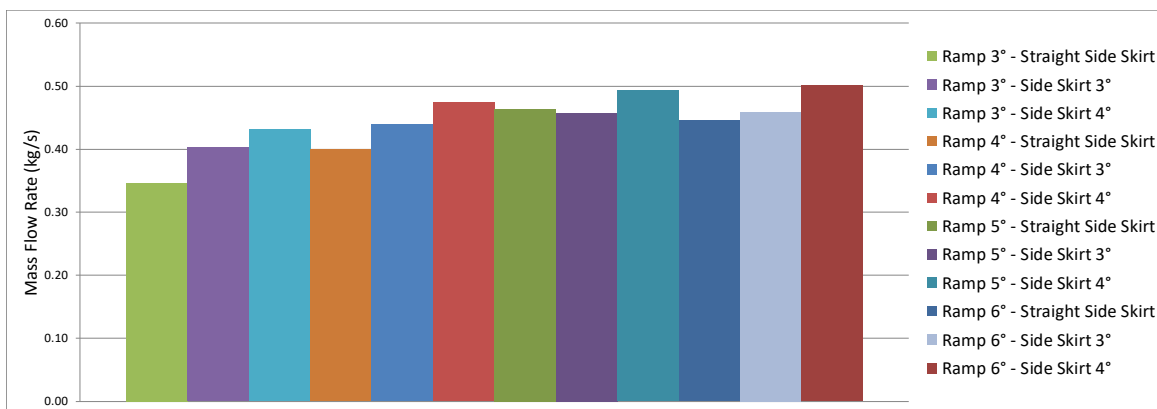


Figure 4.4: Comparison between the mass flow rate of all 12 device configurations

Table 4.1: Summary of the preliminary simulations comparing the average outlet velocity, mass flow rate and average outlet pressure of all 12 configurations

Device Configuration Number	Device Description	Average Outlet Velocity (m/s)	Mass Flow Rate (kg/s)	Average Outlet Pressure (Pa)
-	Baseline	7.77	0.36	-2.59
1	Ramp 3° - Straight Side Skirt	14.80	0.35	-2.21
2	Ramp 3° - Side Skirt 3°	27.80	0.40	-0.56
3	Ramp 3° - Side Skirt 4°	36.16	0.43	2.62
4	Ramp 4° - Straight Side Skirt	13.10	0.40	-1.19
5	Ramp 4° - Side Skirt 3°	22.54	0.44	-0.68
6	Ramp 4° - Side Skirt 4°	29.78	0.48	1.29
7	Ramp 5° - Straight Side Skirt	12.23	0.46	-2.36
8	Ramp 5° - Side Skirt 3°	18.63	0.46	-0.67
9	Ramp 5° - Side Skirt 4°	24.91	0.49	0.39
10	Ramp 6° - Straight Side Skirt	9.86	0.45	-3.52
11	Ramp 6° - Side Skirt 3°	15.85	0.46	-0.73
12	Ramp 6° - Side Skirt 4°	21.41	0.50	0.39

From these preliminary simulations, it was concluded that the optimum two configurations were the devices with a ramp angle of 5° with a side skirt angle of 4° and a ramp angle of 6° with a side skirt angle of 4° (Table 4.2). These two configurations were chosen primarily because they provided the highest mass flow rate exiting the device, which implies that more of the bulk flow is attaching to the device and not recirculating at the underbody. In addition, the outlet pressure of the device was another primary factor. A higher exit pressure could contribute to increasing the pressure in the wake. These two configurations were then simulated on the GCM to evaluate the reduction in the drag coefficient of the model and the overall changes in the trailer underbody flow field and how they contribute to the drag coefficient reduction.

Table 4.2: Results of the preliminary simulations comparing the average outlet velocity, mass flow rate and average outlet pressure of the top two configurations in terms of mass flow rate.

Device Configuration	Average Outlet Velocity (m/s)	Mass Flow Rate (kg/s)	Average Outlet Pressure (Pa)
Ramp 6° - Side Skirt 4°	21.41	0.50	0.39
Ramp 5° - Side Skirt 4°	24.91	0.49	0.39

4.2. Baseline Configuration

4.2.1. Validation

In order to ensure that the computational results obtained are accurate and capture the correct flow field, the baseline configuration was validated using both wind tunnel experimental data provided by the NASA Ames Research Center (Storms et al. 2004, 2006) and a numerical study (Pointer 2004). In the first section, the predicted drag coefficient is validated with the experimental drag coefficient of the GCM. In the second section, the predicted pressure coefficient distribution around the model is compared to the experimental pressure distribution as well as the predicted distribution from another numerical study.

4.2.1.1. Drag Convergence

In order to validate the simulations conducted in this study on the GCM model, a drag coefficient monitor was set up in ANSYS Fluent to monitor the overall drag coefficient of the vehicle which was conducted in parallel with the residual monitoring. This was conducted on three separate grids, a coarse grid of 12.8 million elements, a medium grid with 20.8 million elements and a fine grid with 25.7 million elements. All three grids converged at around 6000 iterations as shown in Figure 4.5, with the fine grid having a drag coefficient being within 1.6% of the experimental drag coefficient of 0.398. Examining the last 1000 iterations (Figure 4.6), the drag coefficient fluctuates slightly

around a nominal value. This fluctuation was around ± 0.002 for the coarse grid, ± 0.002 for the medium grid and ± 0.001 for the fine grid. Thus, the drag coefficient was calculated for each grid by averaging the drag coefficient over the final 1000 iterations. As previously mentioned, the medium grid was chosen in conducting this research thesis as it provided a balance between computational time and accuracy. These results are summarized in Table 4.3.

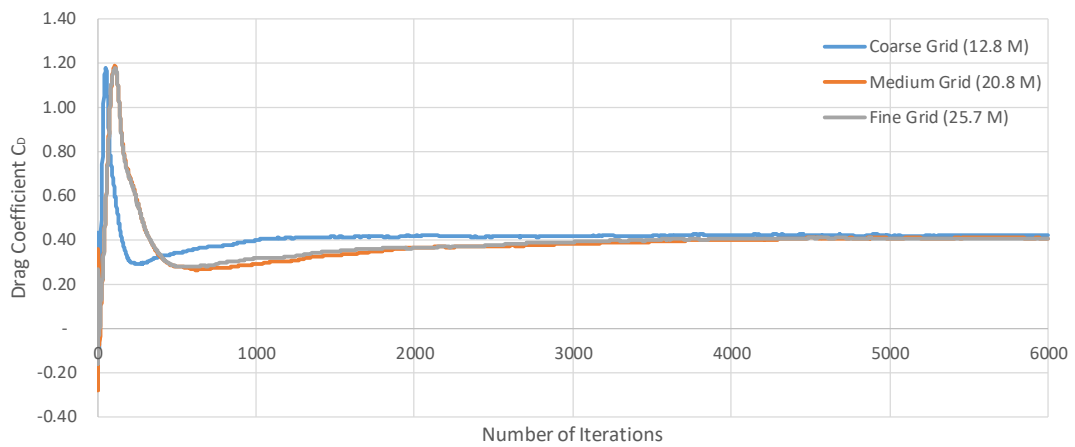


Figure 4.5: Comparison between the drag monitors for all three grids

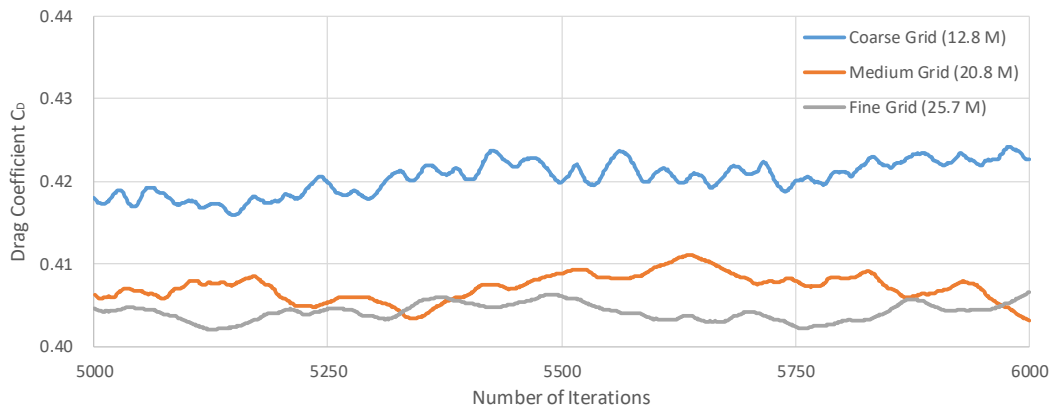


Figure 4.6: Close up of the drag monitors for all three grids at the last 1000 iterations

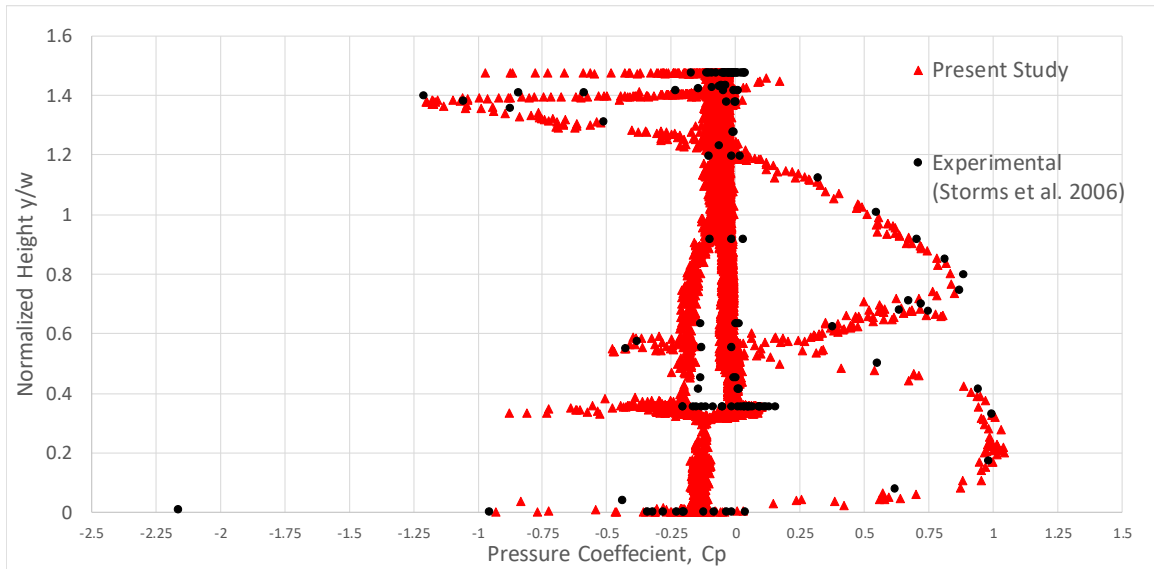
Table 4.3: Drag convergence for the baseline GCM

Grid Resolution	Predicted Drag Coefficient	Error in Drag Coefficient
12.8×10^6	0.420 +/- 0.005	5.6 %
20.8×10^6	0.407 +/-0.004	2.3 %
25.7×10^6	0.404 +/-0.002	1.6 %

4.2.1.2. *Pressure Coefficient Profile*

The surface pressure coefficient around the centerline of the vehicle was compared to the GCM experimental studies done by the NASA Ames Research Center (Storms et al. 2006) and the computational results by Pointer (Pointer 2004). The pressure coefficient was plotted against the normalized vehicle height; where the height of the GCM (y) was normalized by the vehicle width (w). As shown in Figure 4.7, the simulation results showed a similar trend between the experimental pressure coefficient and the predicted pressure coefficient in the present study. The differences in the pressure coefficient primarily occurred at the underbody of the trailer as well as the base of the trailer where the flow recirculation is predominant. These differences can be attributed to the predicted velocity field as the separated flow at the underbody of the trailer and the trailer base cause local discrepancies compared to the experimental results. This was also concluded by Pointer (Pointer 2004) when evaluating the effects of different turbulence models on the pressure coefficient. In addition, the pressure coefficient predictions were similar to the results found by Pointer. The primary differences occurred in the same regions where the experimental results differed (trailer underbody and trailer base). Overall the results were similar except for the trailer underbody and base region where Pointer had closer results to the experimental data.

a)



b)

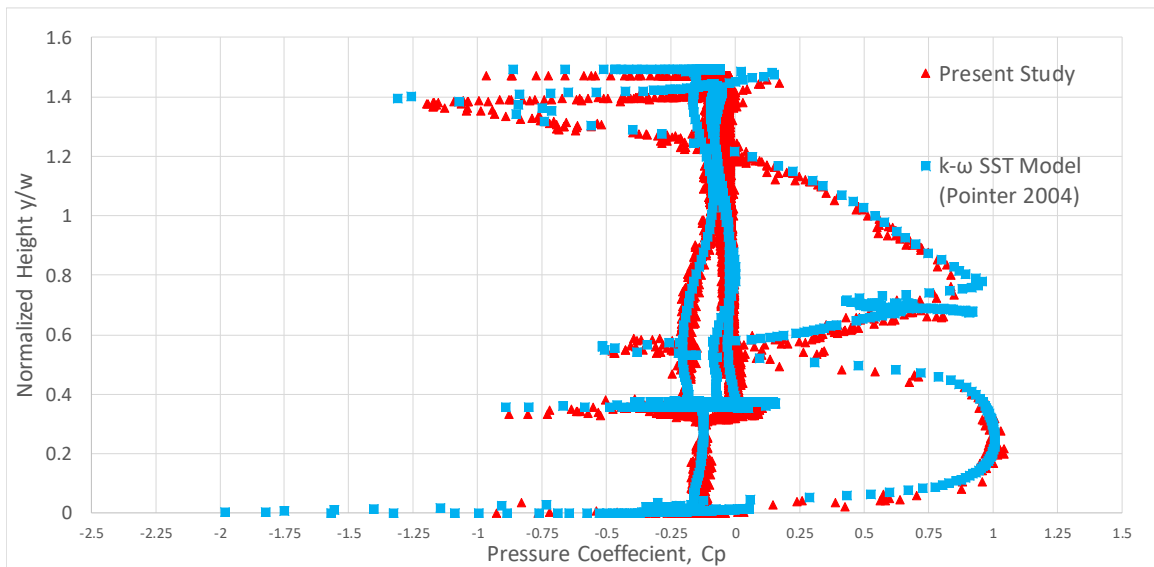


Figure 4.7: a) Comparison between the predicted pressure coefficient distribution along the vehicle surface with the experimental pressure coefficient data for the GCM (Storms et al. 2006) along the normalized height. b) Comparison between the predicted pressure coefficient distribution along the vehicle surface with the computational results by Pointer (Pointer 2004) along the normalized height.

4.2.2. Flow Structure

From the simulations, the drag coefficient (C_D) of the baseline GCM was computed to be 0.407, compared to the experimental drag coefficient of 0.398. Pointer (Pointer 2004) predicted the C_D to be 0.401 for the same turbulence model which is a few drag counts worse than the experimental results. These computational discrepancies can be attributed to differences in the generated grids as well as software differences, as the commercial software used for this study was ANSYS Fluent (ANSYS 2017a) while Star-CD (CD-ADAPCO Group 2008) was utilized by Pointer. In addition, this study was focused on optimizing the device thus the results were considered sufficient for validating the simulations. Examining the underbody flow physics of the model, the flow is comprised of a large recirculation zone that extends from the underbody of the tractor. This recirculation zone is caused by the tractors underbody acting as a pseudo step where the flow separates, recirculating through the trailers underbody. This can be seen in Figure 4.8, which displays the velocity contour along the centerline of the GCM model. Thus, by providing the flow with a ramp where it can attach and be guided to the end of the trailer this recirculation zone can be significantly reduced. In theory, this will reduce the negative pressure region at the underbody due to the flow recirculation. This should also reduce the size of the vehicle wake as the flow will exit the underbody with minimal turbulence. In addition, the expansion that occurs as the flow exits the device should provide an overall pressure increase in the flow at the trailer base. In addition, by implementing a converging side skirt to the ramp, the flow can be accelerated so that it can remain attached at higher ramp angles. The side skirt will also shield the underbody flow from crosswinds that could disturb the flow field and increase drag.



Figure 4.8: Velocity contour along the centerline of the baseline GCM.



Figure 4.9: Velocity contour along the center of the aft trailer wheels of the baseline GCM ($z = 0.123$ m).

Examining the velocity contour at an offset of $z = 0.123$ m (which corresponds to the center of the aft trailer wheels) (Figure 4.9), the recirculation zone at the underbody of the trailer is not as large when compared to the velocity contour at the centerline of the vehicle (Figure 4.8). This is due to the average speed of the flow being higher as you move closer to either side of the tractor, which is because the flow separating from the side of the tractor has not yet recirculated. This can be seen in Figure 4.10, which shows the velocity contours at the underbody of the baseline GCM at four different sections. Section 1 is located 0.5 m forward of the trailer wheels. The sections were positioned in increments of

0.25 m downstream from Section 1 to 3. For Section 4, it is located parallel to the trailer base. At section 1 and 2, the velocity of the flow is highest on either side of the contour while the flow at the center is much slower. As the flow moves toward the trailer wheels (Section 3), it stagnates at the front of the wheels. This causes the flow to recirculate behind the wheels as shown in Section 4.

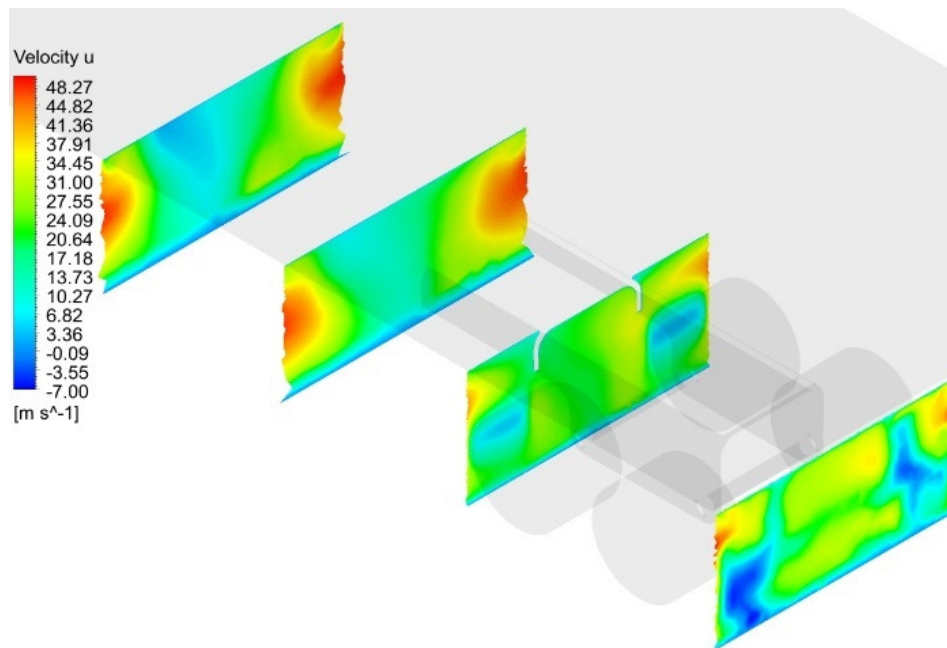


Figure 4.10: Velocity contours along the underbody of the baseline GCM.

4.3. Detailed Results

The first device configuration (Ramp 5° - Side Skirt 4°) reduced the drag coefficient of the vehicle to 0.394. This was approximately 3.3% lower than the baseline GCM. For the second device configuration (Ramp 6° - Side Skirt 4°), the drag reduction was more significant as the drag coefficient of the vehicle reduced to 0.391; a reduction of approximately 4.1%. A comparison between the baseline model and the two devices is shown in Table 4.4. Examining the velocity contours of the two devices (Figure 4.11 and 4.12), the recirculation zone in the baseline model (Figure 4.8) was eliminated. For the

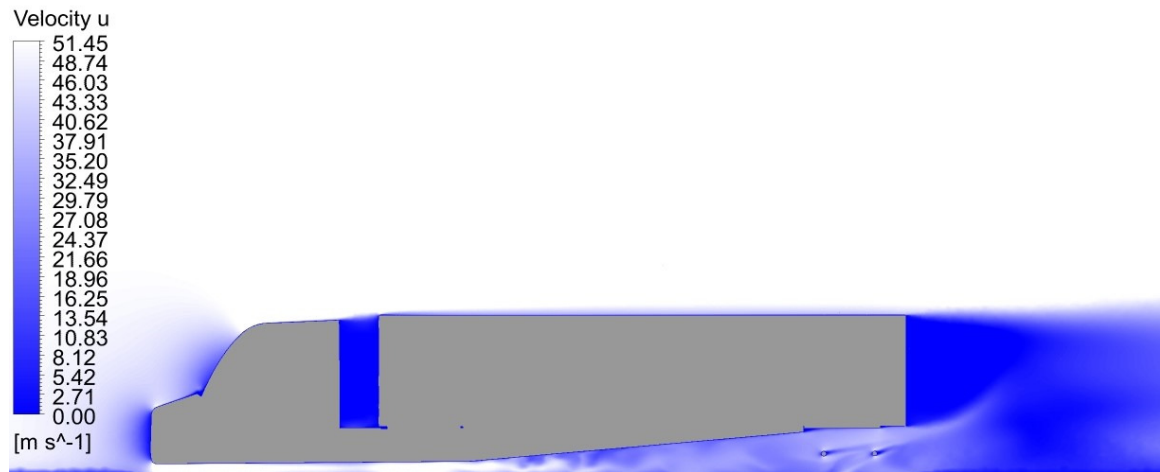
underbody device with a ramp angle of 6° and a side skirt of 4° , the underbody flow remains attached as it flows from the underbody of the tractor. For the first device (Ramp 5° - Side Skirt 4°), the flow recirculates slightly at the end of the device as the edge of the ramp creates a backward facing step. This difference is a result of the decrease in the ramp angle which causes the edge of the device be slightly elevated and not flush with the bottom face of the trailer.

Examining the velocity contours at the underbody of the device, both device configurations have increased the average velocity of the underbody flow (Figure 4.13) when compared to the baseline configuration (Figure 4.10). As shown in Figure 4.13, the velocity of both device configurations was higher compared to the baseline configuration at Sections 1 and 2. Also, the velocity at the outside of both side skirts increased slightly. This is likely due to the side skirt providing a surface for the flow to attach, that otherwise would be detaching and recirculating off the tractor. This, in turn, increased the velocity of the flow impinging the trailer wheels as shown in Section 3, which has slight adverse effects as the flow recirculates behind the trailer wheels (Section 4). This was found to cause a slight increase in drag due to the flow recirculating as it separates around the trailer axles and wheels but was not significant enough to offset the drag reduction contributed by eliminating the underbody recirculation zone.

Ortega and Salari have previously proposed an underbody fairing (Ortega and Salari 2008) that was simulated on a full-scale heavy vehicle. Their optimal design reduced the drag coefficient of the heavy vehicle from 0.641 to 0.599, which is approximately a reduction of 7%. Due to the lack of dynamic similarity, the present results cannot be compared directly to that study as it uses a different tractor-trailer model and Reynolds

number. In addition, Ortega and Salari have simulated the heavy vehicle at a yaw angle of 6.1° while in this study crosswind was not modeled in order to validate the data with the experimental data available for the GCM (Storms et al. 2006). In the next section, the pressure contours of the trailer base will be examined to evaluate the effects of the device on the pressure behind the vehicle.

a)



b)

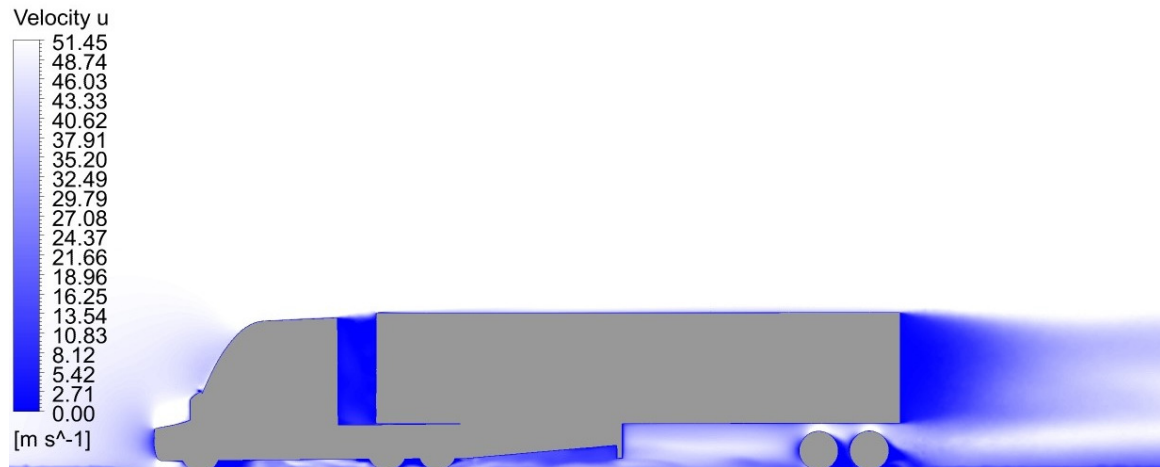
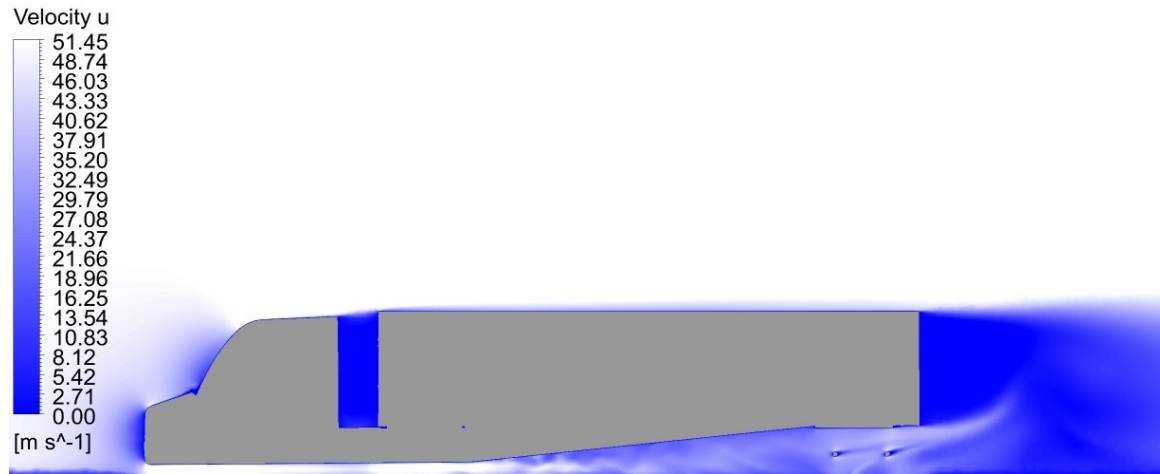


Figure 4.11: Velocity contour of the GCM with the underbody device (Ramp 5° - Side Skirt 4°) at the a) centerline of the model b) center of the aft trailer wheels ($z = 0.123$ m).

a)



b)

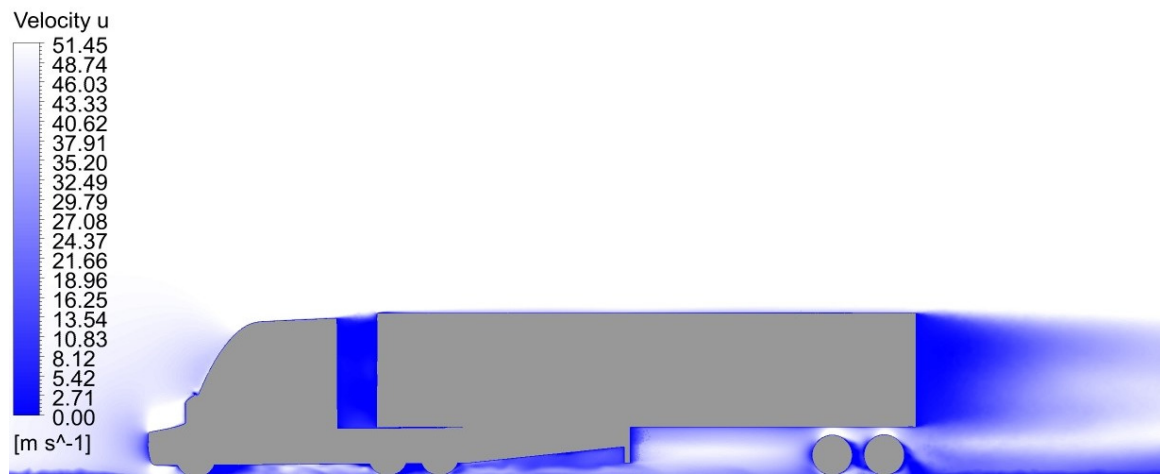
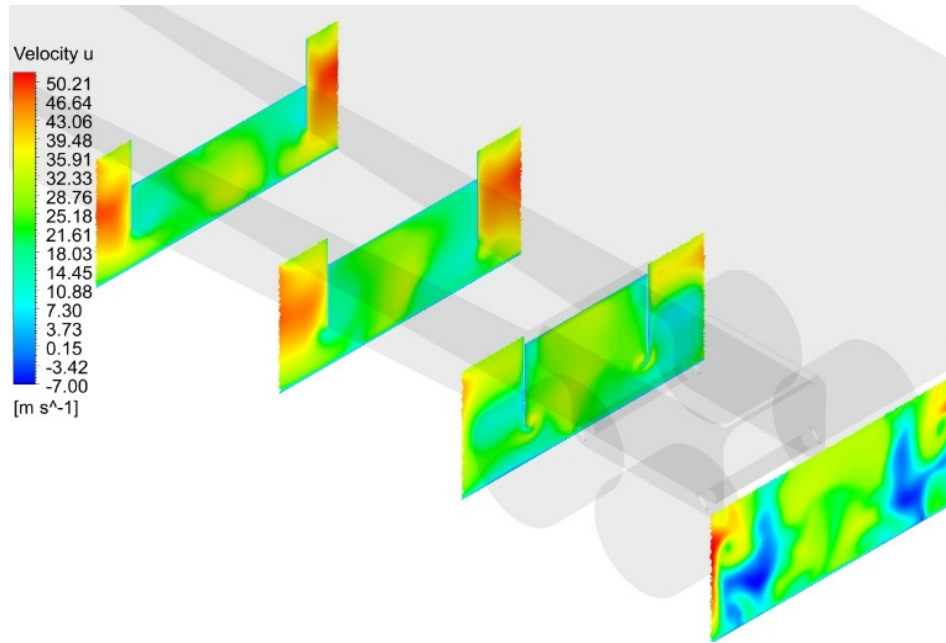


Figure 4.12: Velocity contour of the GCM with the underbody device (Ramp 6° - Side Skirt 4°) at the a) center of the model b) center of the aft trailer wheels ($z = 0.123$ m).

a)



b)

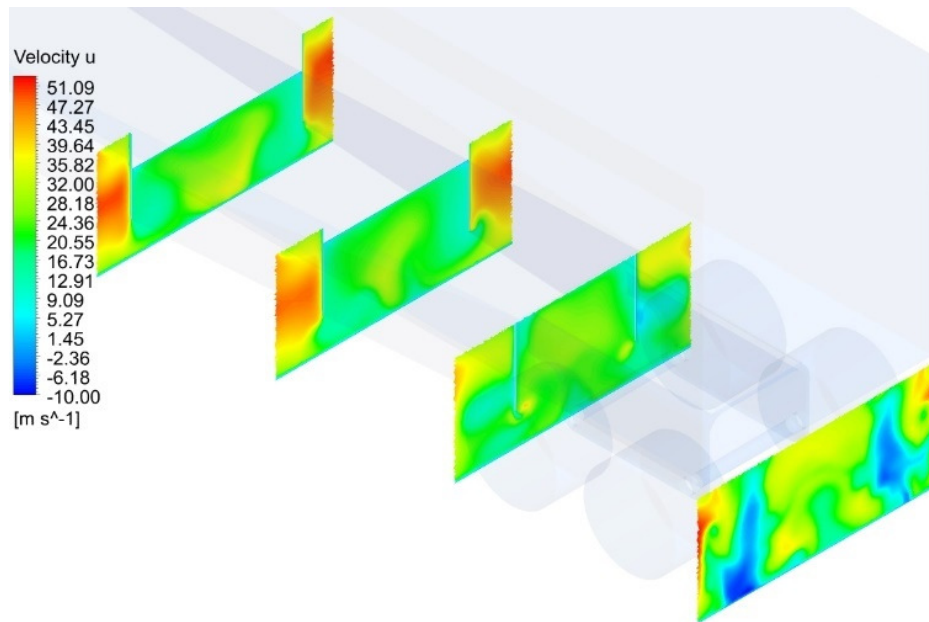


Figure 4.13: a) Velocity contours along the underbody of the baseline GCM with the underbody device (Ramp 5° - Side Skirt 4°). b) Velocity contours along the underbody of the baseline GCM with the underbody device (Ramp 6° - Side Skirt 4°).

Table 4.4: Results of the evaluation of the underbody devices and their percent drag reduction compared to the baseline GCM.

Configuration	Predicted Drag Coefficient	Percent Drag Reduction
Baseline GCM	0.407	-
GCM with Ramp 5° - Side Skirt 4°	0.394	3.3 %
GCM with Ramp 6° - Side Skirt 4°	0.391	4.1 %

4.3.1. Velocity and Pressure Profiles

The velocity profiles and the pressure coefficients at four sections of the underbody were examined on the model using both device configurations in order to compare them with the baseline model. Section 1 is located 0.5 m forward of the trailer wheels. The sections were positioned in increments of 0.25 m downstream from Section 1 to 3. For Section 4, it is located parallel to the back side of the trailer base. All sections were located at a height of $y = 0.3$ m, which is approximately the same height as the trailer axle.

Examining the underbody velocity profiles along both device configuration and comparing them to the baseline model (Figure 4.14) the device alters the underbody flow by increasing the flow velocity at the inside of the device. This could be seen in the velocity profiles at both Sections 1 and 2 (Figure 4.14a and 4.14b), which are located upwind of the trailer wheel assembly. This is similar to what Ortega and Salari (Ortega and Salari 2008) have found with their underbody fairing. Their fairing had a channel running through the center in order to guide the flow exiting the tractor drive wheel. At Section 3 (Figure 4.14c), the velocity profiles for both device configurations were similar to the baseline vehicle except for a slight increase in flow velocity at the outside of the device. As previously mentioned, this would be due to the side skirt providing a surface for the flow that otherwise would be detaching and recirculating off the tractor to attach. This was found to cause a slight increase in drag due to the flow recirculating as it separates around the trailer axles

and wheels but was not significant enough to offset the drag reduction contributed by eliminating the underbody recirculation zone. The velocity profile downstream of the trailer wheel assembly (Section 4) using the device was also similar to the baseline model but as the recirculation was significantly reduced (Figure 4.12a) the air flow exiting the underbody was less turbulent.

Examining the pressure coefficient profiles at the same sections (Figure 4.15), both device configurations reduced the coefficient of pressure throughout the width of the trailer in Sections 1 and 2 (Figure 4.15a and 4.15b). The first device configuration (Ramp 5° - Side Skirt 4°) produced the lowest overall pressure coefficient compared to the second device configuration (Ramp 6° - Side Skirt 4°). This can be attributed to the larger ramp inclination angle being less conducive for flow reattachment compared to a smaller ramp angle. At Section 3 (Figure 4.15c), both device configurations and the baseline model displayed identical coefficients of pressure. This is due to the flow stagnating at the trailer wheels on both ends while remaining attached at the center of the device as the side skirts converge. For Section 4 (Figure 4.15d), the coefficient of pressure decreased slightly for both device configurations compared to the baseline model. This is caused by the increase in flow rate through the trailer wheel assembly as the flow is guided away from the trailer wheels. This will cause a slight increase in drag due to the flow recirculating as it separates around the trailer axles, but it is not significant enough to offset the drag reduction contributed by the reduction of high-speed flow interacting with the trailer wheels. Similar results were reported by Ortega and Salari (Ortega and Salari 2008) with their longest channeled fairing as it reduced the fluid velocity to which the trailer wheel assembly is exposed to.

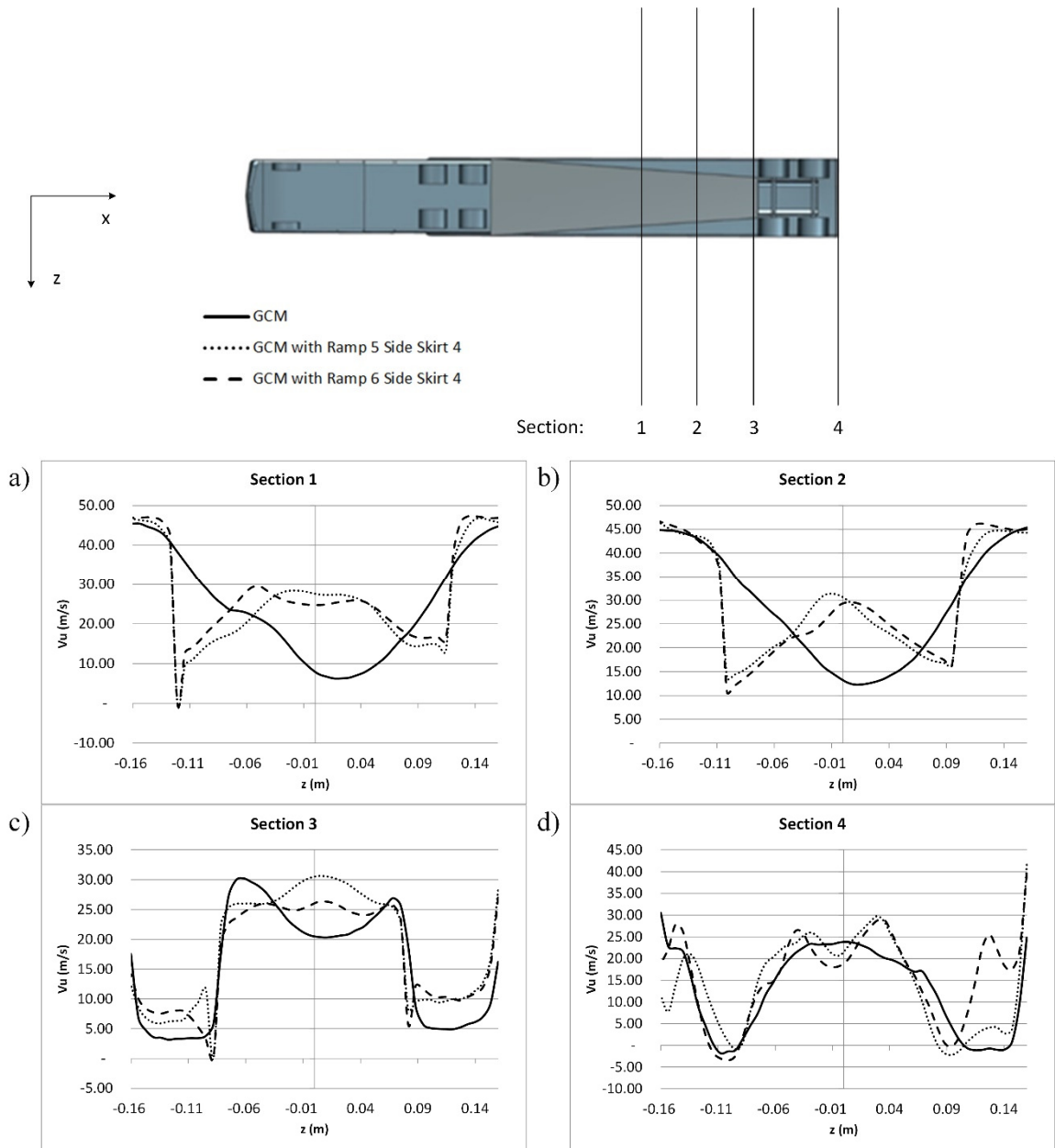


Figure 4.14: Velocity profile (V_u) at the trailer underbody comparing the baseline GCM (solid line), GCM with Ramp 5° - Side Skirt 4° (dotted line) and the GCM with Ramp 6° - Side Skirt 4° (dashed line). The profiles were located at $y = 0.3$ m with a 0.25 m spacing between a) Sections 1, b) Section 2 and c) Section 3 where Section 3 is at device exit. d) Section 4 is parallel to the trailer backside.

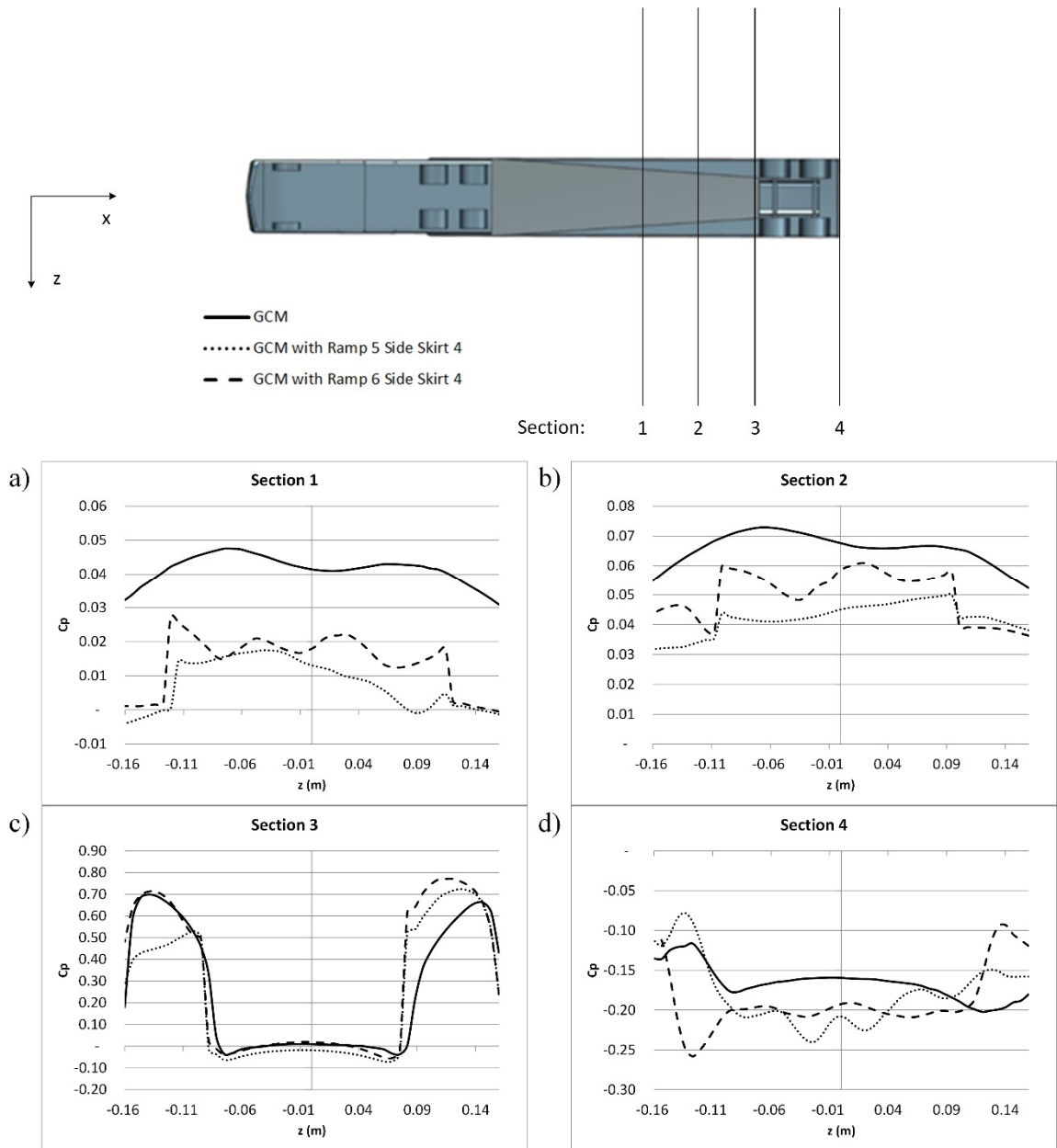


Figure 4.15: Coefficient of pressure (C_p) at the trailer underbody comparing the baseline GCM (solid line), GCM with Ramp 5° - Side Skirt 4° (dotted line) and the GCM with Ramp 6° - Side Skirt 4° (dashed line). The profiles were located at $y = 0.3$ m with a 0.25 m spacing between a) Sections 1, b) Section 2 and c) Section 3 where Section 3 is at device exit. d) Section 4 is parallel to the trailer backside.

4.3.2. Pressure Contours

Examining the coefficient of pressure (C_p) at the back surface of the trailer with both device configurations and the baseline configuration (Figure 4.16), the lowest C_p tends to be at the lower region of trailer backside. For the baseline model, this region is the largest covering around a third of the trailer backside with a C_p approximately between -0.18 and -0.2 (Figure 4.16a). The addition of the device with a ramp angle of 5° and a side skirt angle of 4° decreased the size of that low-pressure region as seen in Figure 4.16b. Another noticeable change is that the device also increased the C_p behind the trailer wheels. This was due to the flow being forced to exit the trailer underbody through the tandem axle housing. This led the pressure coefficient to decrease in that region as seen in Figure 4.16b as the majority of the flow is exiting the underbody from there at a higher velocity. The second device configuration (Ramp 6° - Side Skirt 4°) (Figure 4.16c), displayed an identical pressure coefficient field at the back side of the trailer compared to the first configuration. Since the second device configuration (Ramp 6° - Side Skirt 4°) has proven to have a higher drag reduction compared to the first configuration (Ramp 5° - Side Skirt 4°) as well as better flow characteristic, the rest of this analysis will be conducted on the second device configuration. From hereafter, the second device configuration will be referred to as the optimized device.

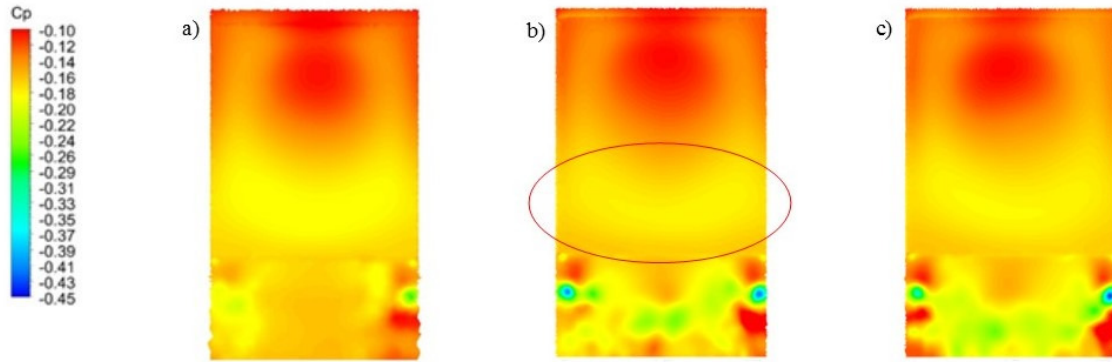


Figure 4.16: Pressure coefficient (C_p) prediction at the trailer base of the a) baseline GCM, b) the GCM equipped with the underbody device (Ramp 5° Side Skirt 4°) and c) the GCM equipped with the underbody device (Ramp 6° Side Skirt 4°).

In order to further investigate and verify the effects of the proposed device on the wake of the vehicle, the pressure at the wake of the baseline model was examined and compared to the model with the optimized device. The coefficient of pressure was investigated at 6 different planes located at the trailer base. Planes A to C were located parallel to the trailer base in order to capture the flow changes downstream of the wake. Plane A was located at the trailer base, while Planes B and C were positioned 0.09 m and 0.18 m from Plane A. Meanwhile, Planes 1 to 3 were located perpendicular to the trailer base in order to capture the flow details occurring in the horizontal plane. Plane 1 was located 0.08 m from the bottom edge of the trailer base. Planes 2 and 3 were located 0.16 m and 0.24 m away from Plane 1. Figure 4.17 indicates the locations of these planes on the trailer base.

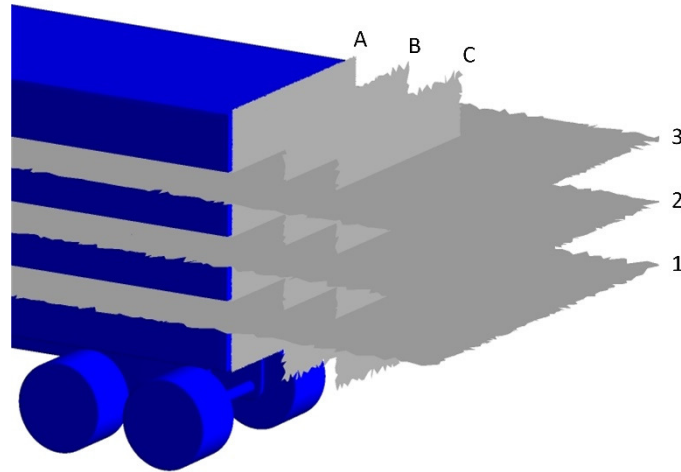


Figure 4.17: Planes where the pressure contours at the wake are located. Plane A was located at the trailer base, while Planes B and C were positioned 0.09 m and 0.18 m from Plane A. Plane 1 was located 0.08 m from the bottom edge of the trailer base, with Planes 1 to 3 were positioned in increments of 0.08 m.

Examining the coefficient of pressure (C_p) at Plane A (Figure 4.18a), the lowest pressure tends to be concentrated at the lower portion of the trailer base. For the baseline model, this region covers approximately a third of the trailer wake. Compared to the model with the optimized device, the size of this low-pressure region was decreased as seen in Figure 4.18a. Moving further downstream in the wake to Plane B, the effects of the optimized device become more prominent as it increases the overall pressure at this plane of the wake (Figure 4.18b). The pressure at this plane for the model with the optimized device is higher than the baseline vehicle by 2.2%. As for Plane C, the effect of the device is less noticeable. This is expected, as Plane C is close to the end of the wake, where the influence of the device is minimal. This increase in pressure at the three planes contributes to the decrease in the drag coefficient of the vehicle.

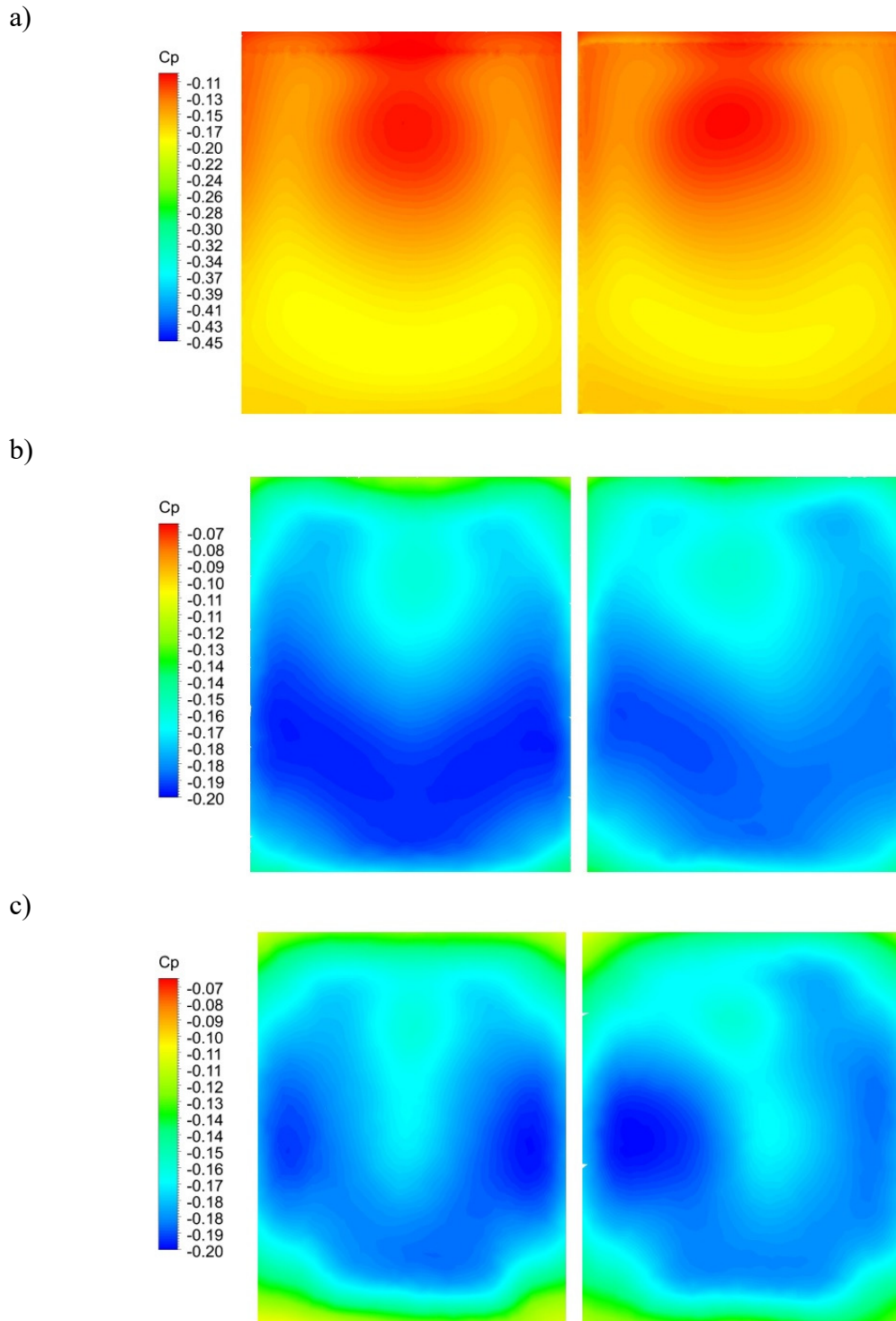


Figure 4.18: Comparison between the pressure at the wake of the baseline model (left) and the model with the optimized device (right) at a) Plane A, b) Plane B and c) Plane C. The location of these planes is shown in Figure 4.17.

Meanwhile, examining the pressure contours at Plane 1 (Figure 4.19a), the model with the optimized device increased the pressure at this region of the wake compared to the baseline model. At Plane 2 (Figure 4.19b), the increase in pressure due to the device was less noticeable. However, at Plane 3 (Figure 4.19c), the baseline model and the model with the optimized device displayed nearly identical pressure contours. This is expected as due to the device not influencing the pressure in this region as much as the plane is further away from the effect of the underbody. Also, the flow separating from the top surface of the trailer has influence due to this plane being closer to the top of the trailer. By creating a plane that starts at the top edge of Plane A and end at the bottom edge of Plane C, the changes occurring diagonally through the wake can be compared between the baseline model and the model with optimized device. As shown in Figure 4.20, the optimized device increases the pressure at this plane compared to the baseline model. Overall, increasing the pressure in the wake reduces the adverse impact of this region on the drag coefficient of the vehicle. Additionally, the increase in the overall pressure reduced the size of the wake as evident in Planes 1 and 3 (Figure 4.19a and 4.19c), where the length of the low-pressure region was decreased. This reduction in wake length was approximately 3.5% compared to the baseline model wake length.

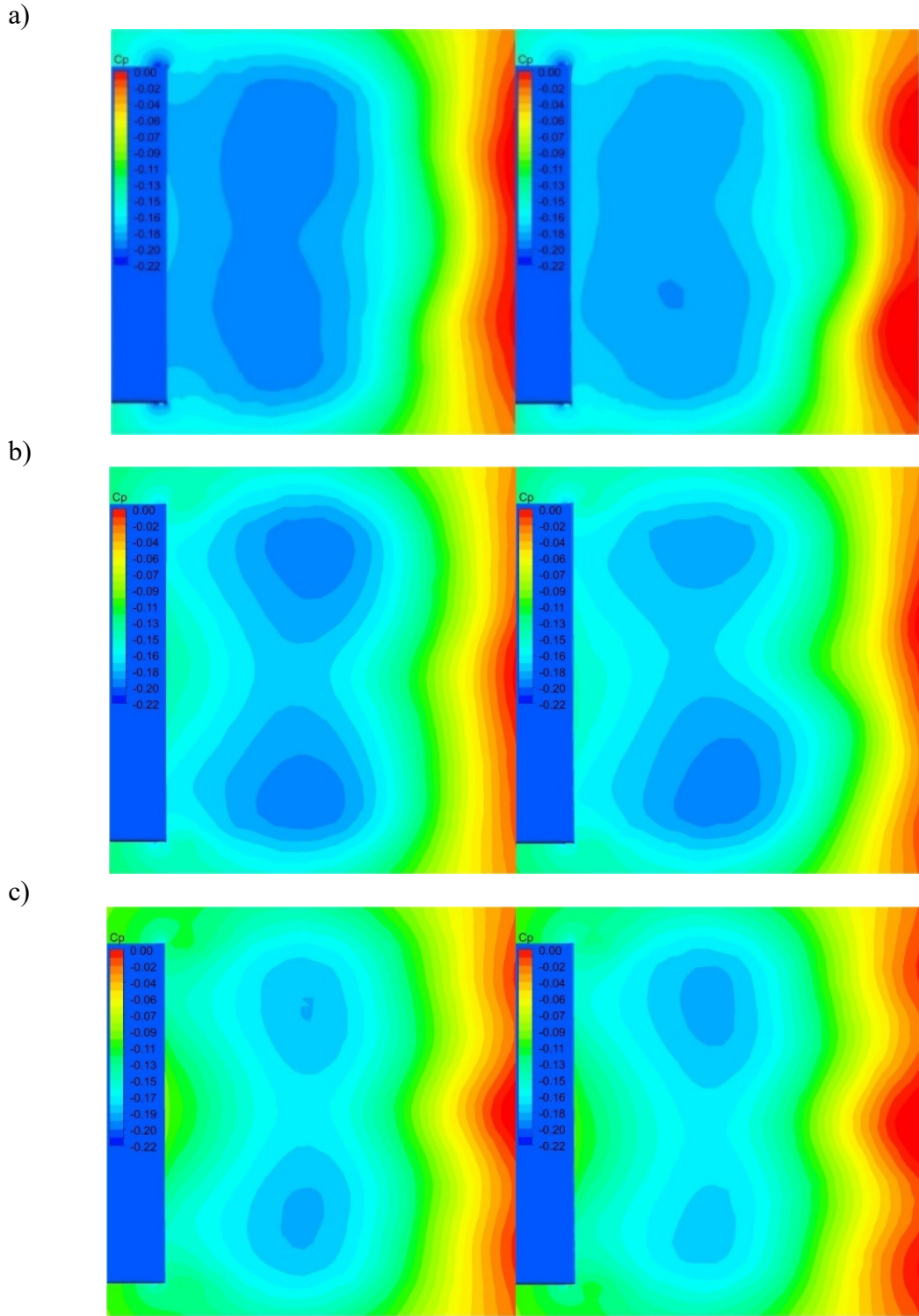


Figure 4.19: Comparison between the wake of the baseline model (left) and the wake of the model with the optimized device (right) at a) Plane 1, b) Plane 2 and c) Plane 3. The location of these planes is shown in Figure 4.17.

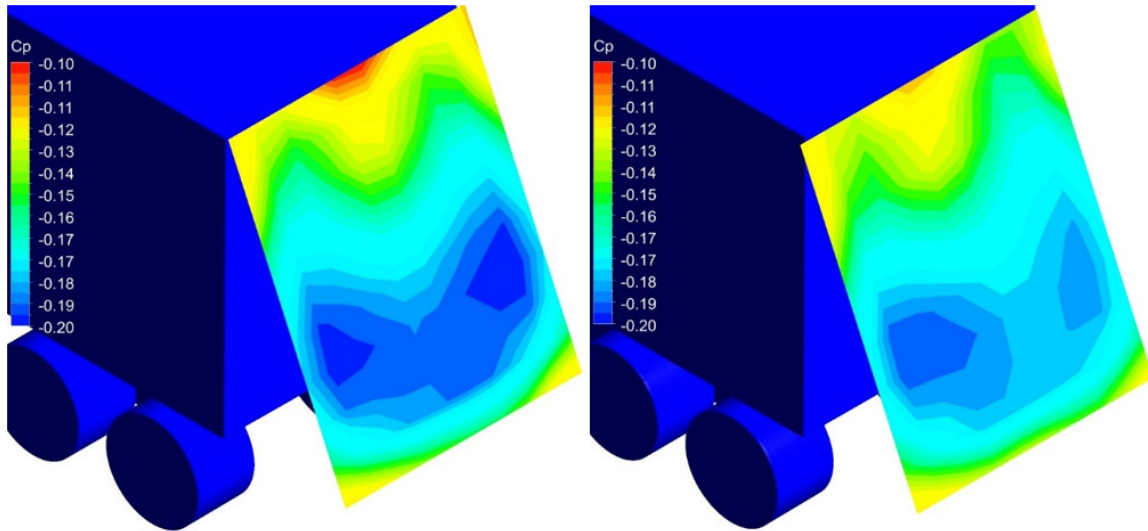


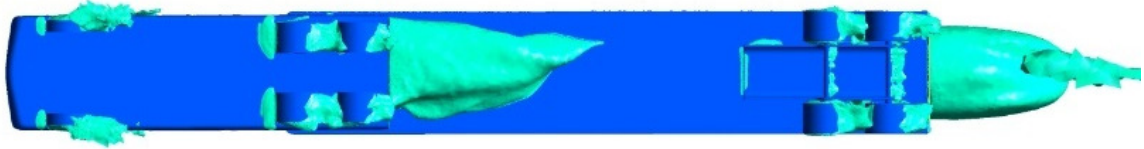
Figure 4.20: Comparison between the wake of the baseline model (left) and the wake of the model with the optimized device (right) at a slanted plane

4.3.3. Iso-Surfaces

To further determine how the underbody flow influences the wake region of the model, the flow structure at the underbody of the model is examined. The iso-surfaces in Figure 4.21 are used to illustrate the effects of the devices on the model. The velocity was set to $V_u = -0.01$ m/s to highlight the regions with flow separation/recirculation. As shown in Figure 4.21a for the baseline case, the flow separates from the tractor drive wheels and underbody, creating a low-pressure region that spans approximately half the length of the trailer. In addition, the wake of the model is slightly larger as it includes another small recirculation region that is closer to the domain ground. With the optimized device (Figure 4.21b), the recirculation region at the underbody of the tractor is eliminated. Moreover, the low-pressure region that was apparent beyond the large recirculation region was eliminated. It also appears that the wake of the model with the optimized device is smaller in length compared to the baseline model. This will be further examined in later sections. In addition, the device has increased the average velocity throughout the underbody of the model

(Figure 4.22b) compared to the baseline model (Figure 4.22a). As shown in Figure 4.22b, the bulk flow inside the optimized device had higher overall velocities throughout the length of the device; reaching approximately 30 m/s at the device exit compared to the baseline model where the velocity peaked at about 22 m/s (Figure 4.22a).

a)

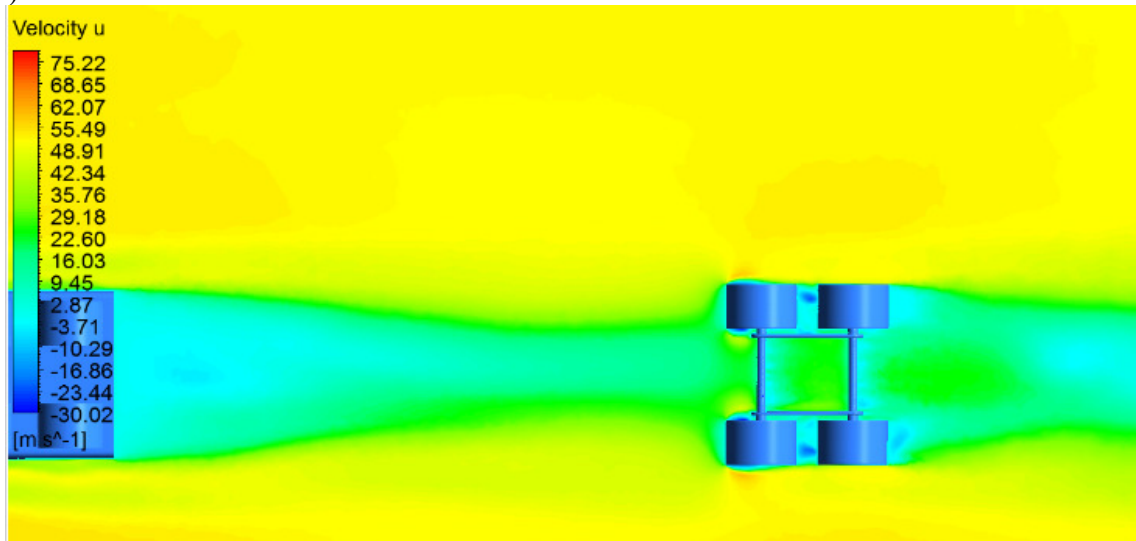


b)



Figure 4.21: Iso-surface at $V_u = -0.01$ m/s for the a) baseline model and b) model with optimized device

a)



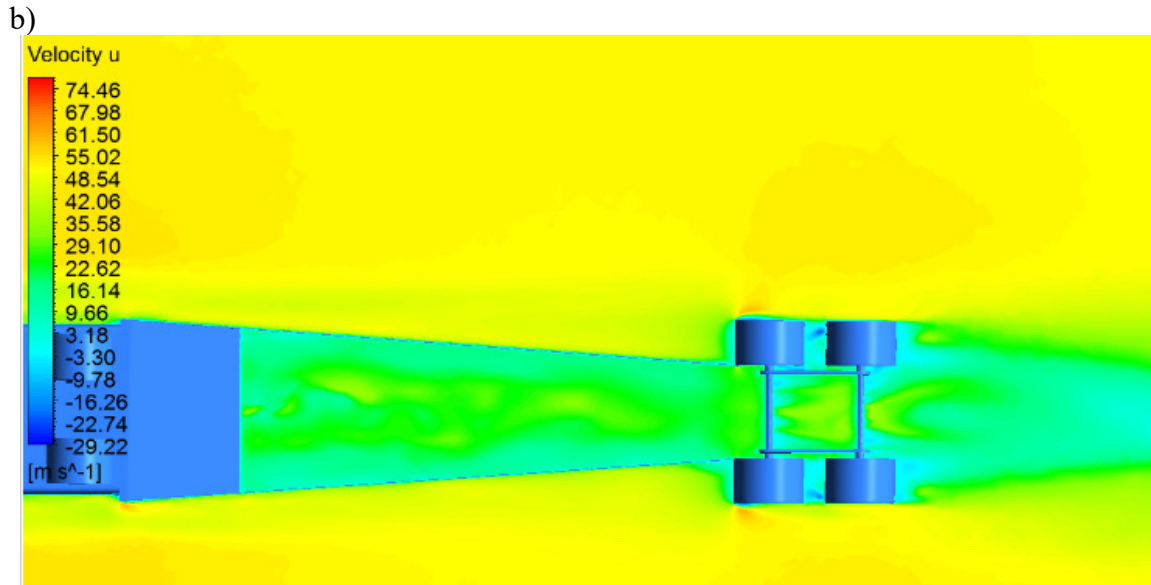


Figure 4.22: Velocity contours at the a) underbody of the baseline model and b) the underbody of the model with optimized device

4.3.4. Streamlines

Examining the velocity streamlines at the wake, the changes in the flow due to the device can be identified. For the baseline model (Figure 4.23a), the flow exits the underbody of the trailer with the flow closer to the underbody recirculating immediately into the wake, while the flow closer to the ground follows a curved path downstream (highlighted in red). Most of this flow eventually recirculates into the wake but travels a longer path. This leads to an increase in the length of the wake. Meanwhile, for the model with the optimized device (Figure 4.23b), the majority of the bulk flow exiting the device is attached to the surface of the device as will be shown later. This allows the flow to smoothly exit in a streamline that recirculates into the wake; reducing the length of the wake as shown in Figure 4.23b (highlighted in red). As mentioned previously, this reduction in the wake length was approximately 3.5% compared to the baseline model wake length. Additionally, this confirms the size decrease seen previously at the pressure contours at the wake (Figures 4.11 – 4.12) and the iso-surface (Figure 4.21b). It is also

noticeable that the recirculation at the bottom of the wake has slightly increased but with no noticeable effect on the pressure.

Examining the velocity streamlines at the underbody (Figure 4.24), it clearly shows that the flow is neatly attached to the device with minimal recirculation zones. However, flow separation and recirculation zones can be found in the baseline model as shown in Figure 4.24a. In addition, Figure 4.24 confirms the reduction of recirculation zones stated earlier in Figure 4.11 and 12.

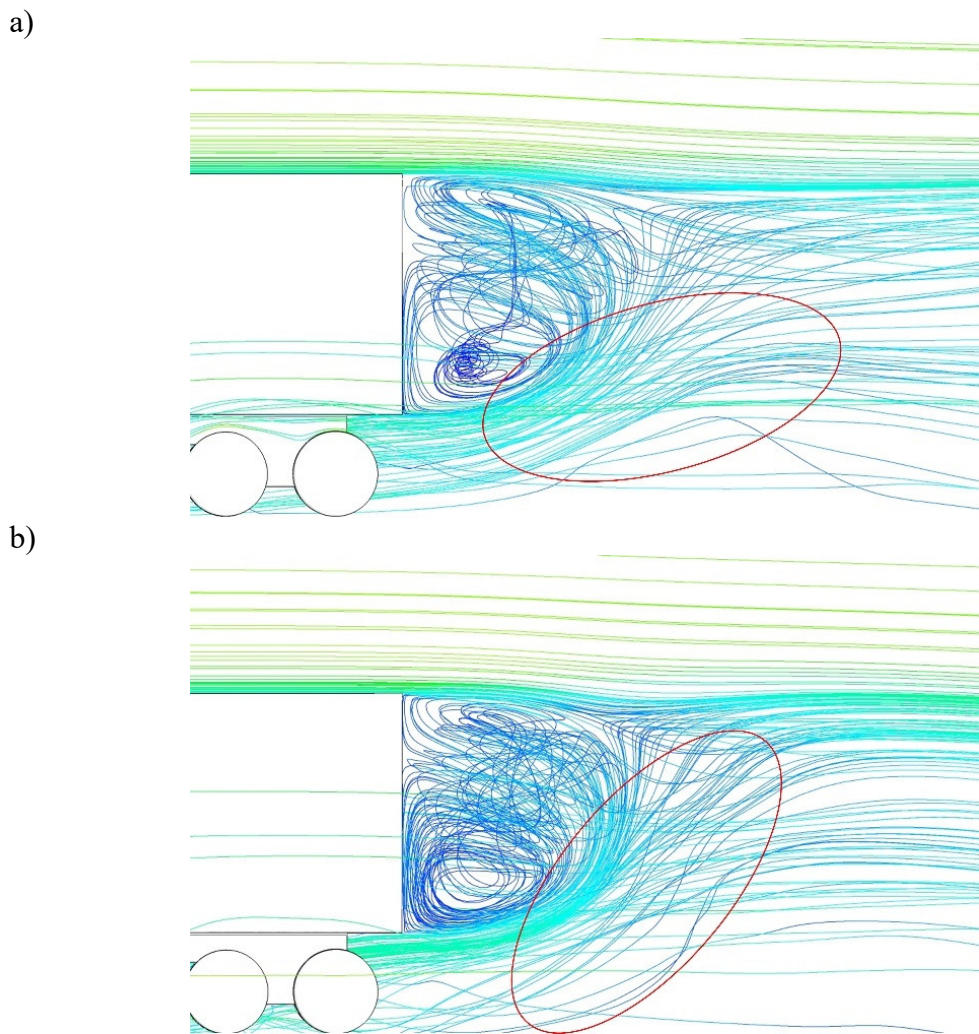


Figure 4.23: Comparison between the velocity streamlines at the wake of the a) baseline model and b) model with optimized device

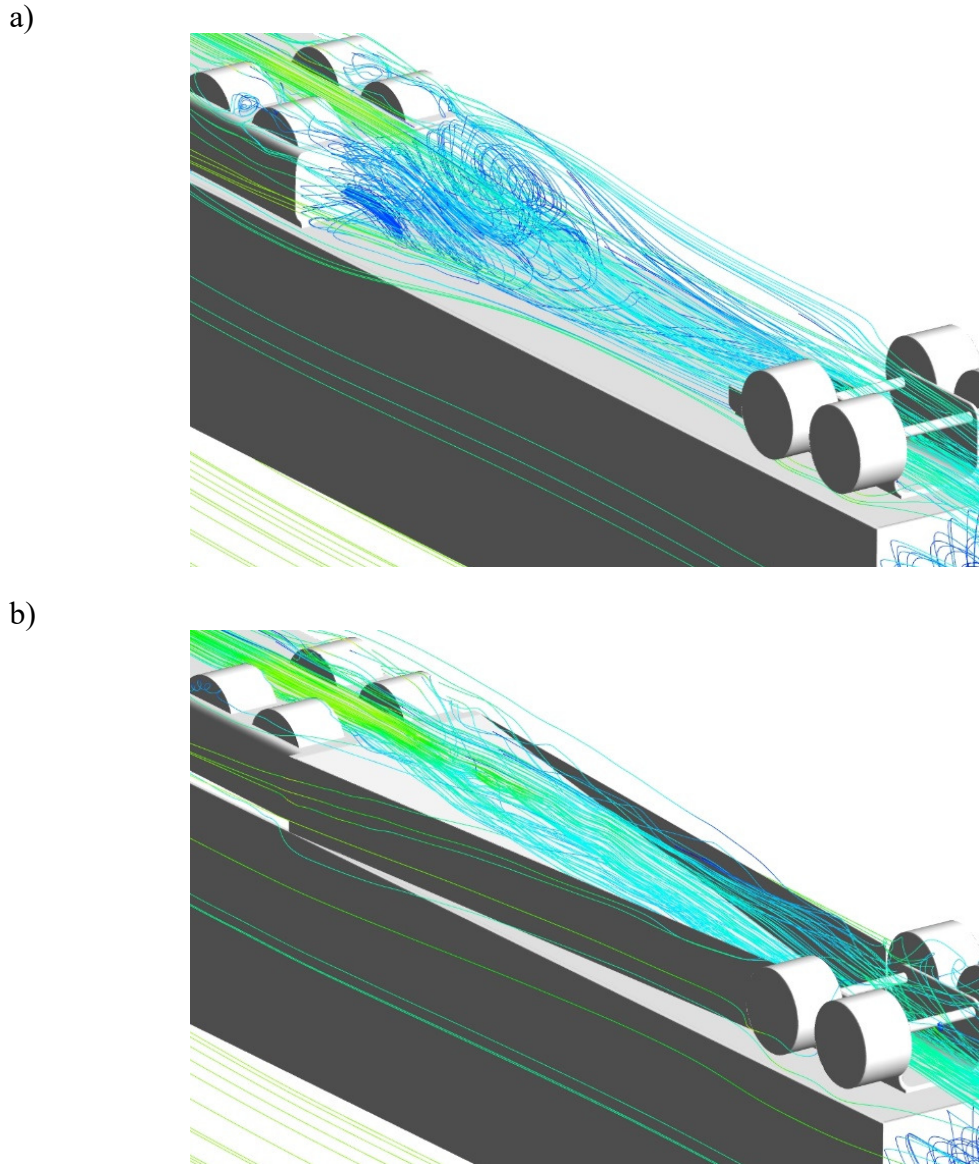


Figure 4.24: Comparison between the velocity streamlines at the underbody of the a) baseline model and b) model with optimized device

4.3.5. Turbulence Kinetic Energy and Intensity

In order to further investigate and verify the effects of the proposed device on the wake of the vehicle, the turbulence kinetic energy was examined on the baseline model and compared to the model with the optimized device. The turbulence kinetic energy profile was extracted from 5 sections located on the trailer base. Section 0 was located at the

bottom edge of the trailer base. Each position was then positioned in increments of 0.09 m from Section 0. Figure 4.25 indicates the locations of the sections on the trailer base.

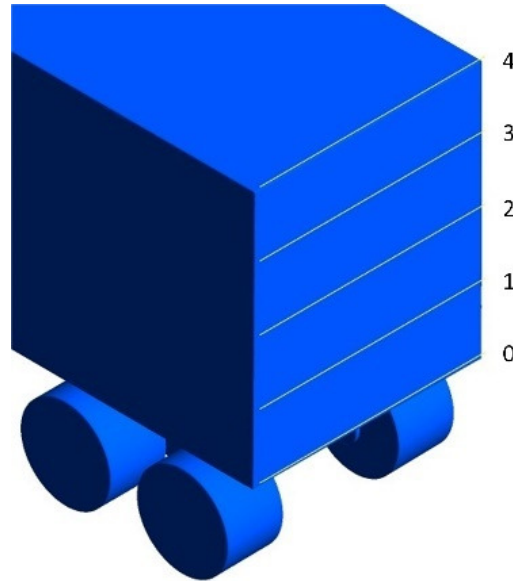
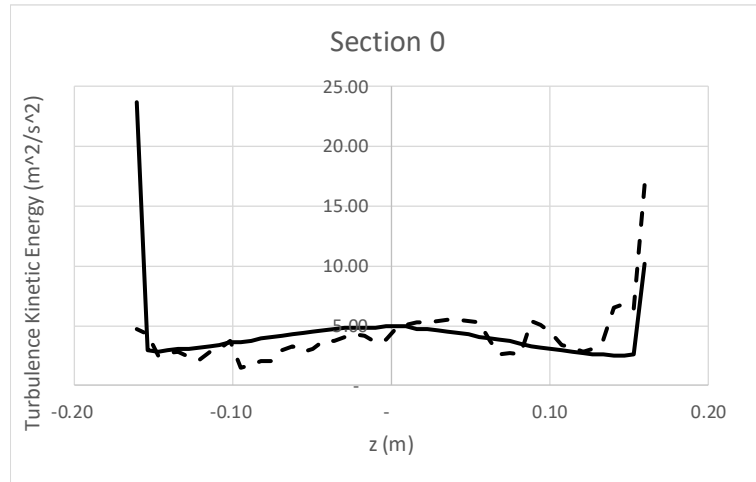


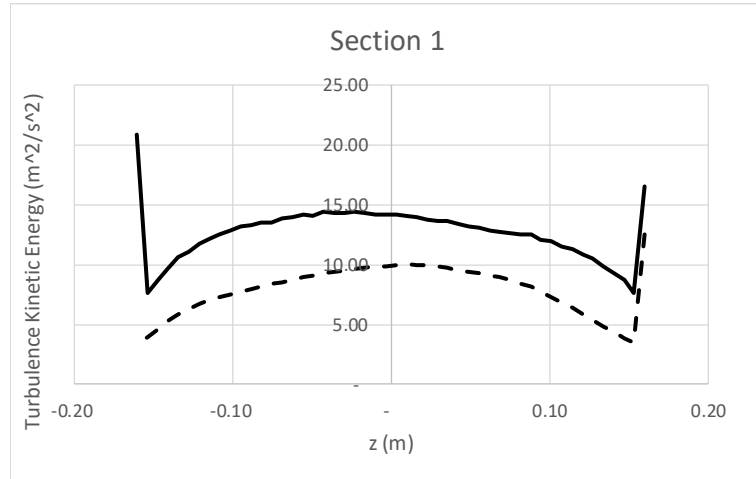
Figure 4.25: Locations where different profiles and contours are obtained. Section 0 is at the bottom edge of the trailer base, with each consecutive section being in increments of 0.09 m, and Section 4 being at the top edge of the trailer base.

Examining the turbulence kinetic energy profile at Section 0 (Figure 4.26a), the optimized device displayed a similar turbulence kinetic energy profile compared to the baseline model. This similarity could be attributed to the flow being on the edge of separation, making both flow profiles identical. As for the profile at Section 1 (Figure 4.26b), the optimized device exhibits an overall lower turbulence kinetic energy compared to the baseline model. This is also evident in the profiles at Section 2 to 4 (Figure 4.26c – 4.26e). By decreasing the turbulence kinetic energy at the surface of the trailer base, the size of the model's wake can be reduced.

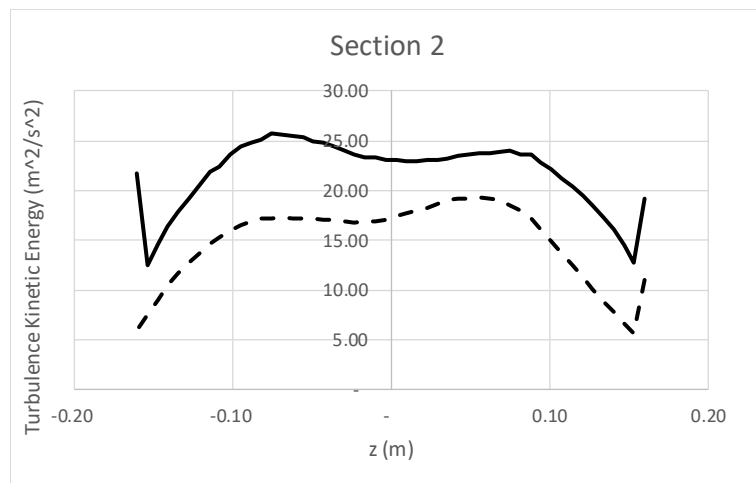
a)



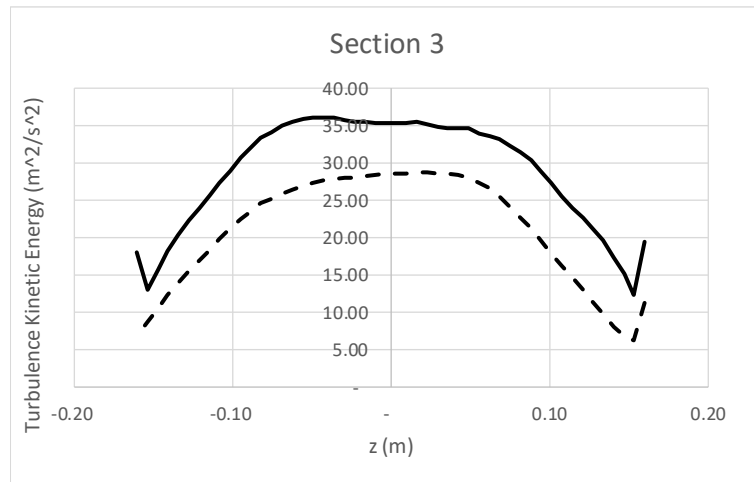
b)



c)



d)



e)

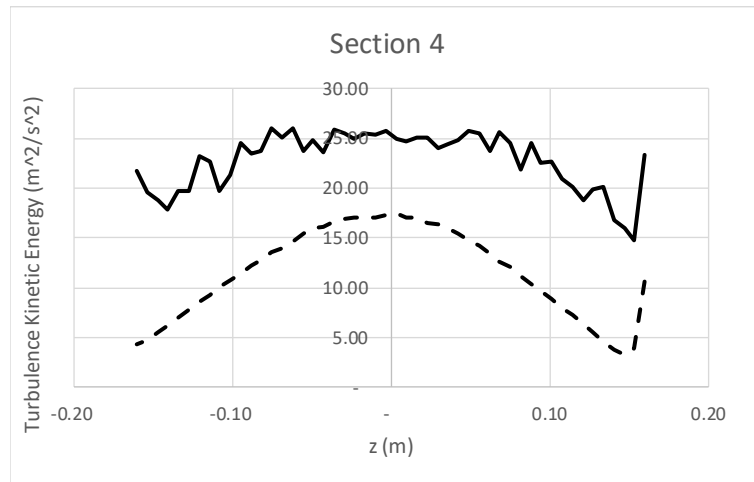
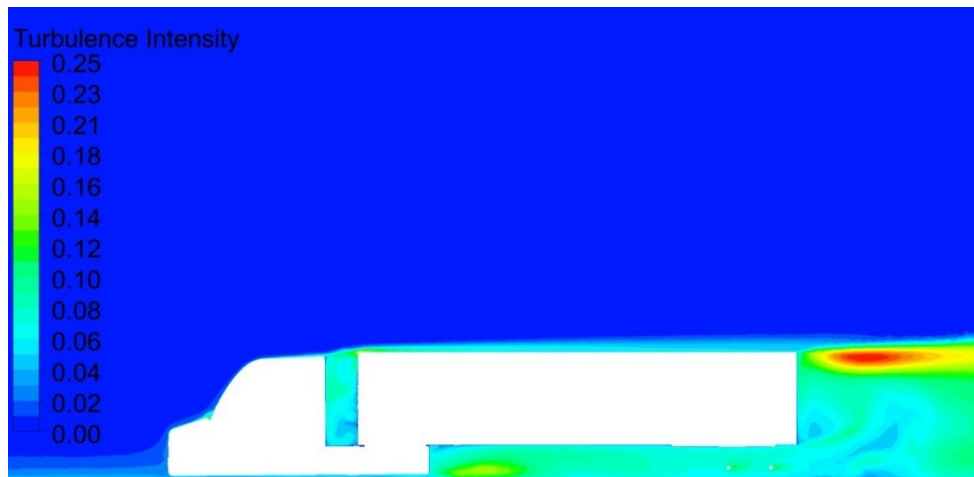


Figure 4.26: Turbulence kinetic energy profiles at position a) 0, b) 1, c) 2, d) 3 and e) 4 for the baseline model (solid lines) compared to model with optimized device (dashed lines)

a)



b)

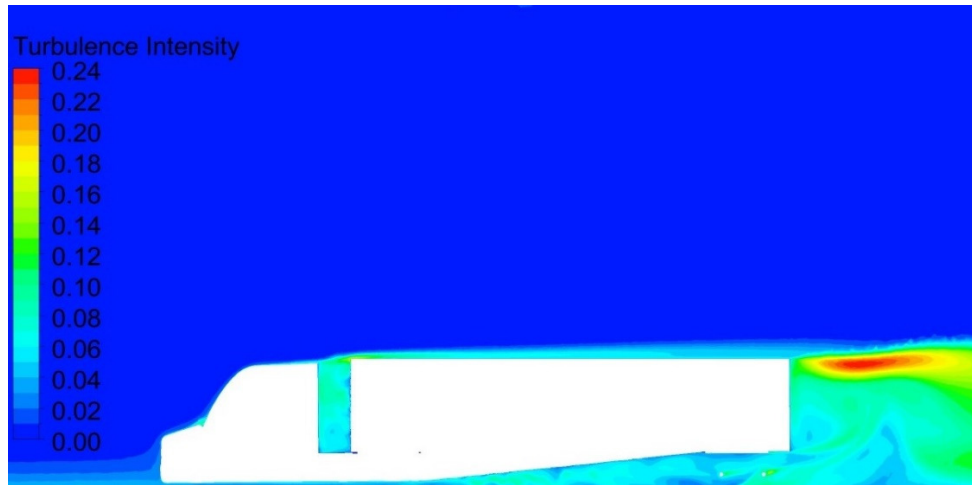


Figure 4.27: Comparison between the turbulence intensity at the centerline of the a) baseline model and b) model with optimized device

Examining the turbulence intensity at the centerline of the model; the optimized device (Figure 4.27b) reduces the turbulence intensity at the underbody of the model when compared it to the baseline model (Figure 4.27a). This is primarily due to the elimination of flow recirculation at the underbody using the optimized device.

4.4. Active Mechanism

The mechanism was packaged inside the device in order to prevent any changes in the underbody flow field that could adversely affect the performance of the device. In addition, the collapsible mechanism is designed to be actuated using a single motor, which adds to the novelty of the design and packaging. Figure 4.28 displays the device and its various components in the deployed position, where the ramp **5** and the converging side skirts **1** are fully open.

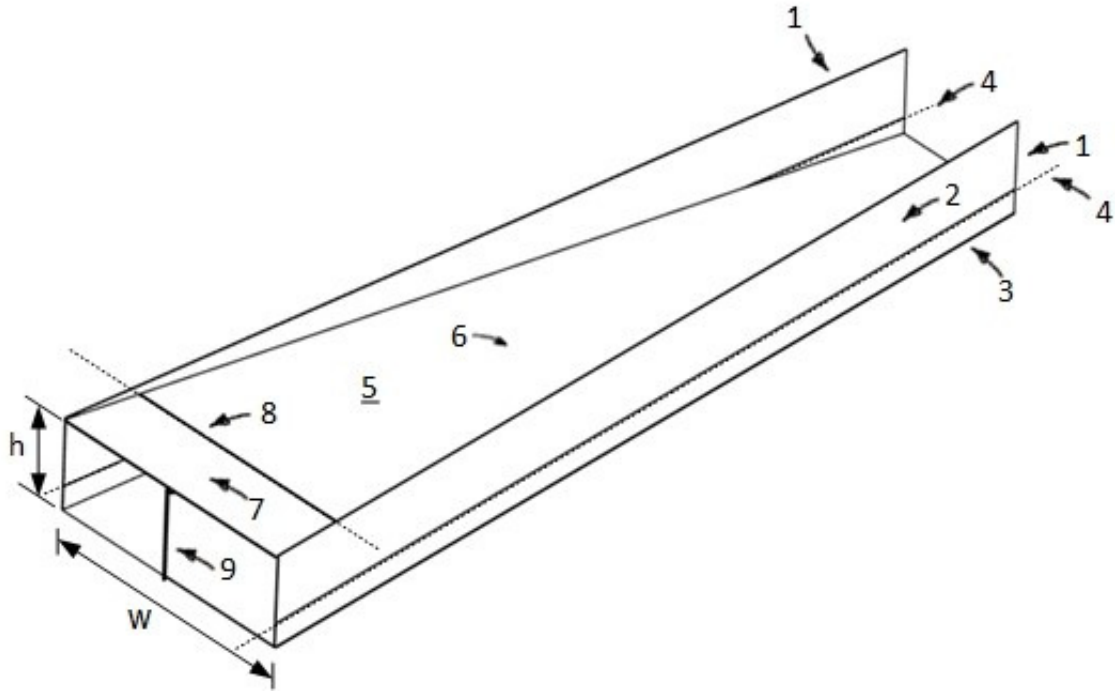


Figure 4.28: Device in the deployed position

The ramp **5** is composed of two components, the first section **7** and the second section **6**. Once collapsing is initiated, the first section of the ramp **7** moves downward using a motor to slide on the rail **9**. The rail allows the first section **7** to slide and also rotate in the clockwise direction around joint **10**. This allows the ramp to collapse and stay within the device perimeters which are enclosed by the bottom surface of the device. Figure 4.29 displays a close up of the rail.

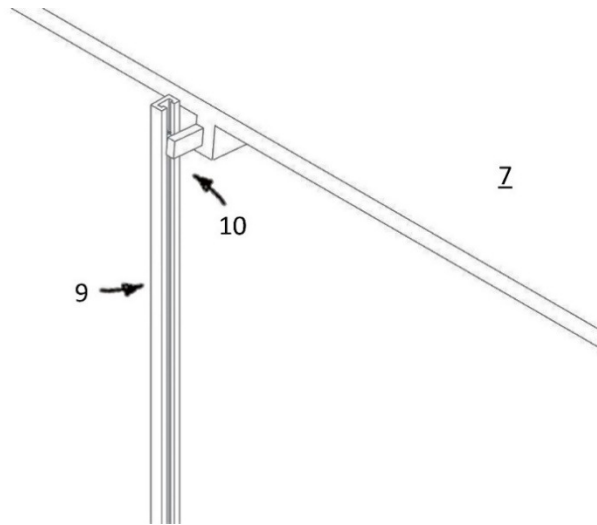


Figure 4.29: Close up of the 2 DOF rail joint

As the first section of the ramp **7** slides and rotates around joint **10** using the rail **9**, it is also pivoting around joint **8**, which connects both sections of the ramp. Shown in Figure 4.30, the second section of the ramp **6** is connected to the bottom surface of the device using joint **12**. This joint allows both sections of the ramp to rotate around **11**. Figure 4.31 displays the device with the ramp halfway through collapsing. As the motor continues to pull the ramp towards the bottom surface of the device, the side skirts are triggered to collapse automatically using a unique solution.

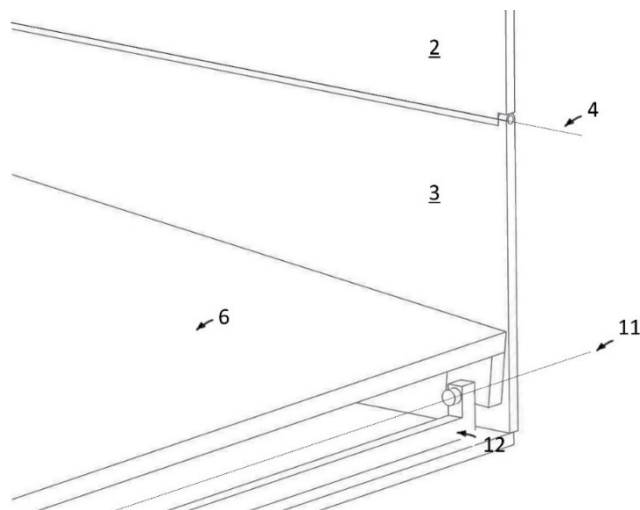


Figure 4.30: Close up of the ramp pivot joint

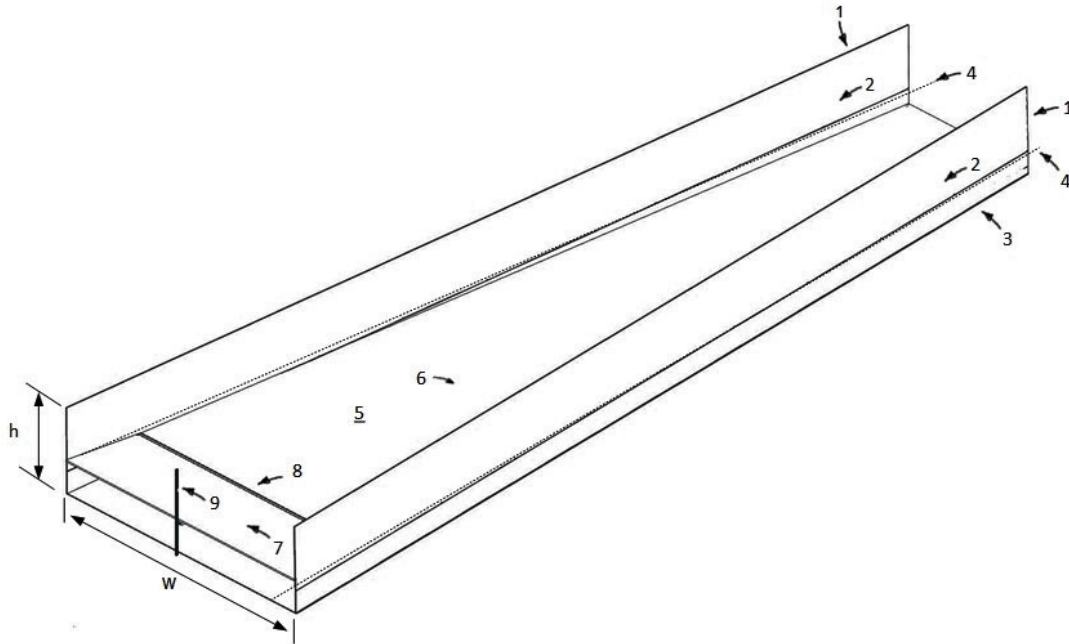


Figure 4.31: Device halfway during ramp collapsing

As soon as the ramp passes the joint **4** that connects both side skirt sections, this triggers the first section of the side skirt **2** to collapse. The first section **2** and the second section **3** of the side skirts are connected using a self-closing hinge **13**. Figure 4.32 shows a close up of the locations of the self-closing hinges. A self-closing hinge is a hinge that has a spring. The spring is preloaded as the device is deployed; where the ramp pushes both side skirts during deployment. This preloads the self-closing hinges and allows for the device to collapse using only one motor. This is similar to the hinge on a self-closing door, where the hinge is preloaded as a person opens the door and the door automatically closes once the person is not in contact with it.

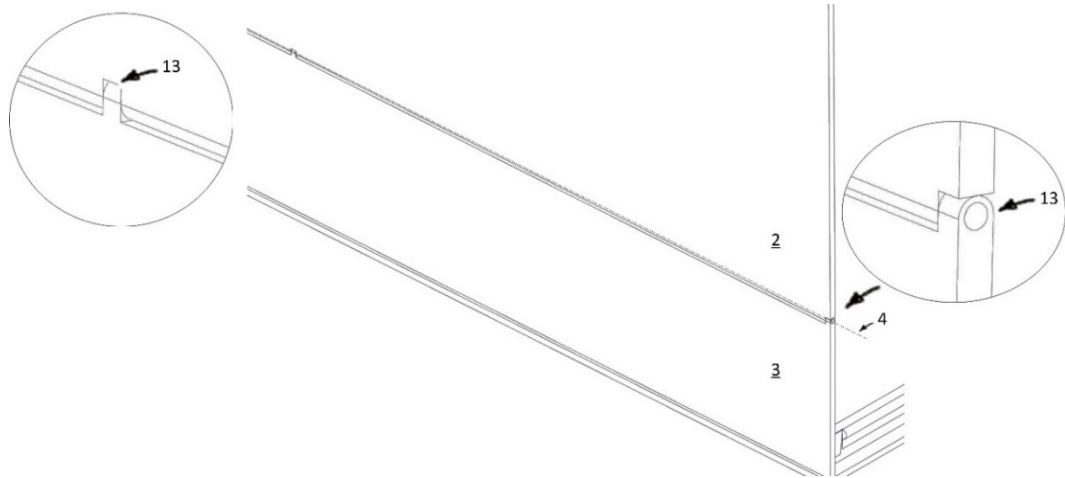


Figure 4.32: Close up of the side skirt indicating the locations of the self-closing hinges

Figure 4.33 shows the device with the ramp fully closed and the side skirts in the process of collapsing. The second section of the side skirt **3** is fixed to the bottom surface of the device. The first section of the side skirt **2** is connected to the second section **3** using the self-closing hinges mentioned previously. The hinges **13** rotate around **4** to allow the first section of the side skirt **2** to move a full 90 degrees to fold flat on top of the ramp. The fully collapsed device is shown in Figure 4.34.

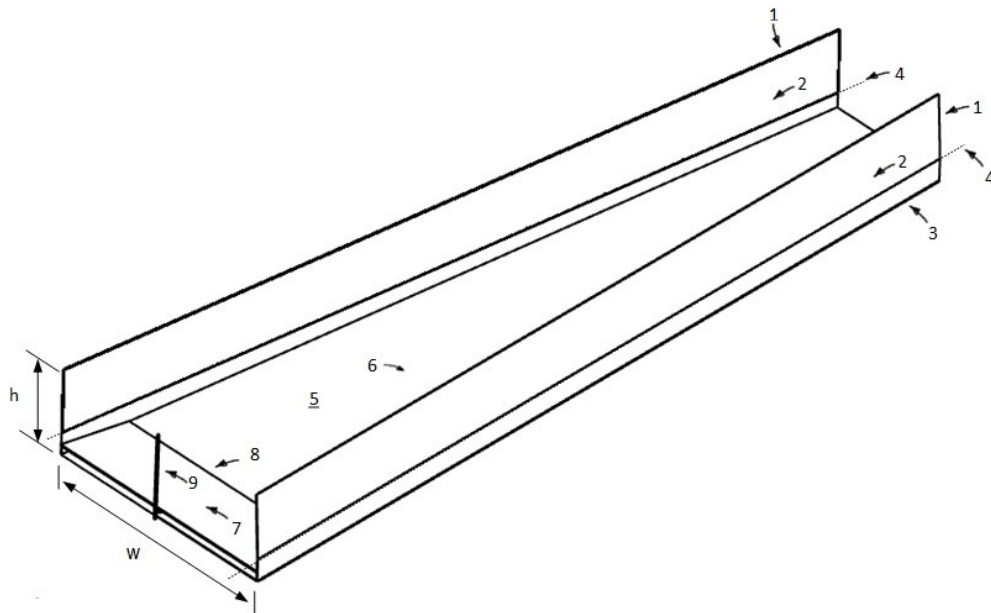


Figure 4.33: Device with ramp collapsed

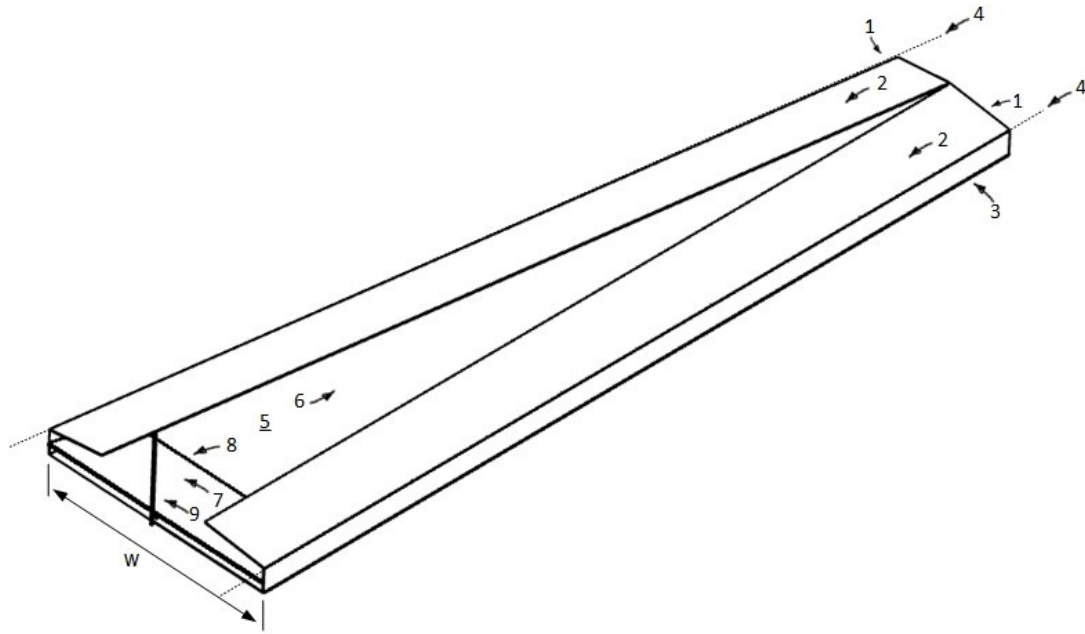


Figure 4.34: Device in the collapsed position

Once the device is collapsed, the vehicle maintains a ground clearance that is nearly identical to a vehicle without the device; due to the device's low profile construction. This low profile is possible due to the device being hollow from the inside in order to save weight and to accommodate the collapsible mechanism. The novel mechanism is designed to deploy the device without the use of a motor, by only using gravity. The motor is only used during collapsing to lift the device and lock it in place. The locking mechanism allows the device to stay in position without the need of any external power from the motor. Thus, the mechanism only uses energy whenever the device is collapsed allowing the device to have minute energy consumption.

As the device was designed to have a minimal footprint while maintaining optimal functionality, it can be constructed from flexible composite materials such as fiberglass as they provide a lightweight solution. In addition, fiberglass is flexible yet can withstand frequent impact.

4.5. Summary of Results

In this research thesis, concepts for reducing the aerodynamic drag of tractor-trailers are developed and analyzed. These concepts were aimed specifically to reduce the drag caused by the underbody region of a tractor-trailer. Twelve different device configurations were simulated and analyzed in the preliminary study in order to determine the two configurations that had the highest drag reduction potential. The drag reduction potential was evaluated based on three metrics: mass flow rate, average outlet velocity and average outlet pressure of the configuration. Both of these device configurations were then simulated on the GCM, a generic tractor-trailer model. The baseline GCM was validated using experimental wind tunnel data provided by NASA Ames Research Centre. The computational grid used was within 2.3 % of the experimental drag coefficient of the GCM. In addition, the baseline GCM was also compared to another numerical study that was conducted using an identical turbulence model.

The first configuration reduced the drag coefficient of the model by 3.3 % while the second configuration reduced the drag coefficient further to 4.1%. It was found that the second configuration eliminated the underbody recirculation region completely while decreasing the negative pressure at the trailer base. As the second configuration had a much favorable impact on the drag coefficient and flow structure around the model, it was chosen as the optimized device and further investigation was conducted to understand its full effect on the flow field around the model.

The optimized device reduced the wake length by approximately 3.5% compared to the baseline GCM. In addition, the device reduced the negative adverse pressure in the wake as well as the turbulence kinetic energy at the trailer base. In order to enhance the

practicality of the device, a novel active collapsible mechanism was developed to make this device deployable automatically at highway speeds and collapsed when not needed. This eliminates the parasitic drag the device might cause while operating below recommended speeds. In addition, it provides a safeguard to protect the device from any road protrusions.

Chapter 5 : Conclusions and Recommendations

5.1. Conclusion

A novel active underbody drag reduction device for tractor-trailers was developed and investigated in this research thesis. The drag reduction potential of twelve device configurations was evaluated based on three metrics: mass flow rate, average outlet velocity and average outlet pressure of the configuration. The simulations were validated using experimental data provided by the NASA Ames Research Centre. A summary of the conclusions drawn from this research thesis is as follows:

- The optimized device achieved the highest drag reduction by reducing the drag coefficient of the GCM by 4.1 %. This was primarily due to the device eliminating the flow recirculation at the underbody of the tractor-trailer.
- The optimized device reduced the length of the wake by approximately 3.5%. In addition, the adverse negative pressure in the wake was reduced.
- An active mechanism was designed around the optimized device in order to allow the device to collapse when not needed to eliminate parasitic drag and to protect the device from road protrusions. As mentioned previously in the literature review, a collapsible underbody device can mitigate some of the primary issues that prevent the widespread adoption of underbody drag reduction devices.

5.2. Main Contribution

The novelty of the proposed device and its improvement over existing devices is a key contribution of this research thesis. The proposed active underbody drag reduction

device is a first of its kind; combining the benefits of a side skirt and a trailer underbody fairing in an operationally viable package. The ability for the device to be actively or manually controlled prevents some of the issues that have prevented the widespread adoption of underbody drag reduction devices. Underbody devices are usually damaged by road protrusions such as loading docks and speed bumps. The ability for the device to collapse below a set speed prevents these damages. In addition, the parasitic drag that could be caused by the device deployment at low speeds is prevented.

5.3. Limitations

The potential limitations of this study can be summarized into the following points:

- Prototype testing was not conducted in this study, thus the influence of environmental effects (i.e. extreme temperatures) on the device was not determined
- As the device was designed around the GCM which has a 13.7 m trailer (45 ft), the influence of the device on larger trailer sizes has not been determined.
- The device was designed without accounting for trailer landing gear. Thus, the trailer's landing gear would need to be detached in order to install the device.

5.4. Recommendations for Future Works

Based on the research conducted in this thesis, several recommendations can be made for future work:

- Examination of the proposed device alongside other heavy vehicle drag reduction devices can be conducted to determine if further drag reduction can be achieved.
- Wind tunnel testing can be conducted to further evaluate the proposed device and determine if further optimization can be made

- The effects of crosswind on the drag reduction of the device can be investigated to better simulate real-life conditions.
- The effects of the flow changes introduced by the device on the vehicle stability can be investigated in a wind tunnel.
- The device can be simulated and/or tested on a moving ground to determine their effect on the flow field and drag reduction.
- Examination of the proposed device at low-speeds to determine the influence of parasitic drag.

Publications from Thesis

Ibrahim, M. and Agelin-Chaab, M., “Investigation and Development of Underbody Aerodynamic Drag Reduction Devices for Trailer Trucks,” SAE Technical Paper 2018-01-0707, 2018, doi:10.4271/2018-01-0707.

Ibrahim, M., and Agelin-Chaab, M., 2018, “Effects of an underbody device on the characteristics of a trailer truck wake region” ASME 2018 5th Joint US-European Fluids Engineering Summer Conference

Ibrahim, M., and Agelin-Chaab, M., 2018, “Optimization of an underbody aerodynamic drag reduction device for trailer trucks” 9th International Symposium on Fluid-Structure Interactions, Flow-Sound Interactions, Flow-Induced Vibration & Noise

References

- Allan, J. W. 1981. "Aerodynamic Drag and Pressure Measurements on a Simplified Tractor-Trailer Model." *Journal of Wind Engineering and Industrial Aerodynamics* 9 (1–2): 125–36. doi:10.1016/0167-6105(81)90083-0.
- American Trucking Associations. 2015. "Reports, Trends & Statistics." http://www.trucking.org/News_and_Information_Reports_Industry_Data.aspx.
- ANSYS. 2013. "ANSYS Fluent Theory Guide." ANSYS Inc.
- . 2017a. "ANSYS Fluent." <http://www.ansys.com/Products/Fluids/ANSYS-Fluent>.
- . 2017b. "ANSYS Fluent User's Guide." ANSYS, Inc.
- Balkanyi, Szabolcs R, Luis P Bernal, and Bahram Khalighi. 2002. "Analysis of the Near Wake of Bluff Bodies in Ground Proximity." <http://dx.doi.org/10.1115/IMECE2002-32347>.
- Barnard, R.H. 2009. "Road Vehicle Aerodynamic Design."
- Batchelor, G. K. 1967. "An Introduction to Fluid Dynamics." *Book*. doi:10.1063/1.3060769.
- Buil, Ramon Miralbes, and Luis Castejon Herrer. 2009. "Aerodynamic Analysis of a Vehicle Tanker." *Journal of Fluids Engineering* 131 (4). ASME: 41204–17. <http://dx.doi.org/10.1115/1.3077135>.
- Castellucci, Paul J, and Kambiz Salari. 2005. "Computational Simulation of Tractor-Trailer Gap Flow with Drag-Reducing Aerodynamic Devices." *Methods*, no. 724. doi:10.4271/2005-01-3625.
- Cattafesta, L. N., and M. Sheplak. 2011. "Actuators for Active Flow Control." *Annual Review of Fluid Mechanics* 43: 247–72. doi:10.1146/annurev-fluid-122109-160634.
- CD-ADAPCO Group. 2008. "STAR-CD." Melville, NY.
- Choi, Haecheon, Jungil Lee, and Hyungmin Park. 2014. "Aerodynamics of Heavy Vehicles." *Annual Review of Fluid Mechanics* 46 (1): 441–68. doi:10.1146/annurev-fluid-011212-140616.
- Cooke, Dave. 2015. "Engines for Change - From Cell Phones to Sodas, How New Truck Standards Can Improve the Way America Ships Goods."
- Cooper, Kevin R. 2003. "Truck Aerodynamics Reborn – Lessons from the Past." *SAE Technical Paper*, no. 2003-01–3376. doi:10.4271/2003-01-3376.
- . 2004. "Commercial Vehicle Aerodynamic Drag Reduction: Historical Perspective as a Guide BT - The Aerodynamics of Heavy Vehicles: Trucks, Buses, and Trains." In , edited by Rose McCallen, Fred Browand, and James Ross, 9–28. Berlin, Heidelberg: Springer Berlin Heidelberg. doi:10.1007/978-3-540-44419-0_2.

- Cooper, Kevin R, and Jason Leuschen. 2005. "Model and Full-Scale Wind Tunnel Tests of Second-Generation Aerodynamic Fuel Saving Devices for Tractor-Trailers." *SAE International* . doi:10.4271/2005-01-3512.
- Corke, T C, and R Spivey. 2008. "Methods and Apparatus for Reducing Drag via a Plasma Actuator." Google Patents. <https://www.google.ca/patents/US20080122252>.
- Croll, Robert H, Walter T Gutierrez, Basil Hassan, Jose E Suazo, and Anthony J Riggins. 1996. "Experimental Investigation of the Ground Transportation Systems (GTS) Project for Heavy Vehicle Drag Reduction." *SAE International* . doi:10.4271/960907.
- Drollinger, R. 1987. "Heavy Duty Truck Aerodynamics." *SAE Technical Paper Series*. doi:10.4271/870001.
- EIA. 2013. "Annual Energy Outlook." <https://www.eia.gov/outlooks/aeo/>.
- . 2017. "How Much Carbon Dioxide Is Produced from Burning Gasoline and Diesel Fuel?" <https://www.eia.gov/tools/faqs/faq.php?id=307&t=11>.
- Englar, R. J. 2001. "Advanced Aerodynamic Devices to Improve the Performance , Economics , Handling and Safety of Heavy Vehicles." *SAE Technical Paper Series 2001-01-2072*, no. 724: 16. doi:10.4271/2001-01-2072.
- EPA and NHTSA. 2011. "Greenhouse Gas Emissions Standards and Fuel Efficiency Standards for Medium- and Heavy-Duty Engines and Vehicles."
- Gilliéron, Patrick, and Azeddine Kourta. 2010. "Aerodynamic Drag Reduction by Vertical Splitter Plates." *Experiments in Fluids* 48 (1): 1–16. doi:10.1007/s00348-009-0705-7.
- Gutierrez, W. T., B. Hassan, R. H. Croll, and W. H. Rutledge. 1996. "Aerodynamics Overview of the Ground Transportation Systems (GTS) Project for Heavy Vehicle Drag Reduction." In *International Congress and Exposition of the Society of Automotive Engineers (SAE)*, 26–29. doi:10.4271/960906.
- Han, T, D C Hammond, and C J Sagi. 1992. "Optimization of Bluff Body for Minimum Drag in Ground Proximity." *AIAA Journal* 30 (4): 882–89. doi:10.2514/3.11005.
- Heineck, James T, Stephen M Walker, and Dale Satran. 2004. "The Measurement of Wake and Gap Flows of the Generic Conventional Truck Model (GCM) Using Three-Component PIV BT - The Aerodynamics of Heavy Vehicles: Trucks, Buses, and Trains." In , edited by Rose McCallen, Fred Browand, and James Ross, 173–84. Berlin, Heidelberg: Springer Berlin Heidelberg. doi:10.1007/978-3-540-44419-0_19.
- Hinze, J. O. 1975. *Turbulence*. 2nd Revise. Mcgraw-Hill College.
- Howell, Jeff, Andrew Sheppard, and Alex Blakemore. 2003. "Aerodynamic Drag Reduction for a Simple Bluff Body Using Base Bleed." *SAE International*, no. 3: 2003-01–0995. doi:10.4271/2003-01-0995.
- Hucho, W, and G Sovran. 1993. "Aerodynamics of Road Vehicles." *Annual Review of Fluid Mechanics* 25 (1): 485–537. doi:10.1146/annurev.fl.25.010193.002413.

- Hyams, Daniel G, Kidambi Sreenivas, Ramesh Pankajakshan, D Stephen Nichols, W Roger Briley, and David L Whitfield. 2011. "Computational Simulation of Model and Full Scale Class 8 Trucks with Drag Reduction Devices." *Computers & Fluids* 41 (1): 27–40. doi:<https://doi.org/10.1016/j.compfluid.2010.09.015>.
- Kader, B. A. 1981. "Temperature and Concentration Profiles in Fully Turbulent Boundary Layers." *International Journal of Heat and Mass Transfer* 24 (9): 1541–44. doi:[10.1016/0017-9310\(81\)90220-9](https://doi.org/10.1016/0017-9310(81)90220-9).
- Khalighi, Bahram, S Zhang, C Koromilas, S. R. Balkanyi, Luis P. Bernal, G. Iaccarino, and P. Moin. 2001. "Experimental and Computational Study of Unsteady Wake Flow Behind a Bluff Body with a Drag Reduction Device." *Society of Automotive Engineers*, no. 724: 1–15. doi:[10.4271/2001-01-1042](https://doi.org/10.4271/2001-01-1042).
- Lanfrit, Marco. 2005. "Best Practice Guidelines for Handling Automotive External Aerodynamics with FLUENT." *Fluent 2*: 1–14.
- Launder, B E, and D B Spalding. 1972. *Lectures in Mathematical Models of Turbulence*. London; New York: Academic Press.
- Lauwers, K. 2009. "Computational and Experimental Analysis of Trailer Shape Modifications for Drag Reduction." Delft University of Technology.
- Leuschen, Jason, and K.R. Cooper. 2006. "Full-Scale Wind Tunnel Tests of Production and Prototype, Second-Generation Aerodynamic Drag-Reducing Devices for Tractor-Trailers." *SAE Technical Paper*, no. 2006-01–3456. doi:[10.4271/2006-01-3456](https://doi.org/10.4271/2006-01-3456).
- Leuschen, Jason, and Kevin R Cooper. 2009a. "Summary of Full-Scale Wind Tunnel Tests of Aerodynamic Drag-Reducing Devices for Tractor-Trailers BT - The Aerodynamics of Heavy Vehicles II: Trucks, Buses, and Trains." In , edited by Fred Browand, Rose McCallen, and James Ross, 451–62. Berlin, Heidelberg: Springer Berlin Heidelberg. doi:[10.1007/978-3-540-85070-0_41](https://doi.org/10.1007/978-3-540-85070-0_41).
- . 2009b. "Summary of Full-Scale Wind Tunnel Tests of Aerodynamic Drag-Reducing Devices for Tractor-Trailers BT - The Aerodynamics of Heavy Vehicles II: Trucks, Buses, and Trains." In , edited by Fred Browand, Rose McCallen, and James Ross, 451–62. Berlin, Heidelberg: Springer Berlin Heidelberg. doi:[10.1007/978-3-540-85070-0_41](https://doi.org/10.1007/978-3-540-85070-0_41).
- Leuschen, Jason, and Youssef Mébarki. 2012. "Examination of the Maskell III Blockage Correction Technique for Full Scale Testing in the NRC 9-Meter Wind Tunnel." *SAE Int. J. Commer. Veh.* 5 (2). SAE International : 640–49. doi:[10.4271/2012-01-2047](https://doi.org/10.4271/2012-01-2047).
- Littlewood, R. P., and M. A. Passmore. 2012. "Aerodynamic Drag Reduction of a Simplified Squareback Vehicle Using Steady Blowing." *Experiments in Fluids* 53 (2): 519–29. doi:[10.1007/s00348-012-1306-4](https://doi.org/10.1007/s00348-012-1306-4).
- Maddox, Stephen, and Kd Squires. 2004. "Detached-Eddy Simulation of the Ground Transportation System." *The Aerodynamics of ...*, 89–104. doi:[10.1007/978-3-540-](https://doi.org/10.1007/978-3-540-)

44419-0_8.

- Malviya, V., R. Mishra, and J. Fieldhouse. 2009. "CFD Investigation of a Novel Fuel-Saving Device for Articulated Tractor-Trailer Combinations." *Engineering Applications of Computational Fluid Mechanics* 3 (4): 587–607. doi:10.1080/19942060.2009.11015293.
- McCallen, Rose, K. Salari, J. Ortega, L.J. DeChant, B. Hassan, C.J. Roy, W.D. Pointer, et al. 2004. "DOE's Effort to Reduce Truck Aerodynamic Drag - Joint Experiments and Computations Lead to Smart Design." *34th AIAA Fluid Dynamics Conference and Exhibit*, no. July: 1–16. doi:10.4271/2005-01-3511.
- McCallen, Rose, Kambiz Salari, J. Ortega, Paul Castellucci, David Pointer, Fred Browand, James Ross, and Bruce Storms. 2007. "DOE Project On Heavy Vehicle Aerodynamic Drag."
- Mehta, Unmeel B. 1998. "Credible Computational Fluid Dynamics Simulations." *AIAA Journal* 36 (5): 665–67. doi:10.2514/2.431.
- Menter, F. 1993. "Zonal Two Equation K-W Turbulence Models For Aerodynamic Flows." In *23rd Fluid Dynamics, Plasmadynamics, and Lasers Conference*. doi:10.2514/6.1993-2906.
- . 1994. "Two-Equation Eddy-Viscosity Turbulence Models for Engineering Applications." *AIAA Journal* 32 (8): 1598–1605. doi:10.2514/3.12149.
- Mohamed-Kassim, Zulfaa, and Antonio Filippone. 2010. "Fuel Savings on a Heavy Vehicle via Aerodynamic Drag Reduction." *Transportation Research Part D: Transport and Environment* 15 (5): 275–84. doi:10.1016/j.trd.2010.02.010.
- Muirhead, V U, and E J Saltzman. 1979. "Reduction of Aerodynamic Drag and Fuel Consumption for Tractor-Trailer Vehicles." *Journal of Energy* 3 (5). American Institute of Aeronautics and Astronautics: 279–84. doi:10.2514/3.48005.
- NASA. 2008. "Uncertainty and Error in CFD Simulations." <https://www.grc.nasa.gov/www/wind/valid/tutorial/errors.html>.
- NRC. 2016. "Fuel Efficiency Benchmarking in Canada's Trucking Industry." <https://www.nrcan.gc.ca/energy/efficiency/transportation/commercial-vehicles/reports/7607>.
- ORNL. 2013. *Transportation Energy Data Book*. 32nded. <http://cta.ornl.gov/data/index.shtml>.
- Ortega, J., and K Salari. 2004. "An Experimental Study of Drag Reduction Devices for a Trailer Underbody and Base." *34th AIAA Fluid Dynamics Conference and Exhibit*, no. July: 1–15. doi:10.2514/6.2004-2252.
- . 2008. "Investigation of a Trailer Underbody Fairing for Heavy Vehicle Aerodynamic Drag Reduction." *Heavy Vehicle Systems Optimization Program - FY 2008 Annual Report*, 241–50. doi:10.4271/2008-01-2601.
- Ortega, J., Kambiz Salari, and Bruce Storms. 2009. "Investigation of Tractor Base

- Bleeding for Heavy Vehicle Aerodynamic Drag Reduction BT - The Aerodynamics of Heavy Vehicles II: Trucks, Buses, and Trains.” In , edited by Fred Browand, Rose McCallen, and James Ross, 161–78. Berlin, Heidelberg: Springer Berlin Heidelberg. doi:10.1007/978-3-540-85070-0_13.
- Pankajakshan, Ramesh, Brent Mitchell, and David L Whitfield. 2009. “Full-Scale Simulations of Drag Reduction Devices for Class 8 Trucks BT - The Aerodynamics of Heavy Vehicles II: Trucks, Buses, and Trains.” In , edited by Fred Browand, Rose McCallen, and James Ross, 339–48. Berlin, Heidelberg: Springer Berlin Heidelberg. doi:10.1007/978-3-540-85070-0_32.
- Paschkewitz, J S. 2006. “Simulation of Spray Dispersion in a Simplified Heavy Vehicle Wake.” *Energy and Environment Directorate, Lawrence Livermore National Laboratory*, 1–20.
- Peres, N, and R Pasquetti. 2013. “Numerical Study of Drag Reduction of a Car Model by Active Control Using Micro-Jets.” *Main*, 1–6.
- Peterson, R. 1981. *Drag Reduction Obtained by the Addition of a Boattail to a Box Shaped Vehicle*.
- Plunkett Research. 2016. “Transportation Industry Statistics and Market Size Overview, Business and Industry Statistics.” <https://www.plunkettresearch.com/statistics/Industry-Statistics-Transportation-Industry-Statistics-and-Market-Size-Overview/>.
- Pointer, W. 2004. “Evaluation of Commercial CFD Code Capabilities for Prediction of Heavy Vehicle Drag Coefficients.” *34th AIAA Fluid Dynamics Conference and Exhibit*, no. July: 1–10. doi:10.2514/6.2004-2254.
- Raemdonck, G. M. R. Van, and M. J. L. Van Tooren. 2008. “Time-Averaged Phenomenological Investigation of a Wake behind a Bluff Body.” *BBAA VI International Colloquium on: Bluff Bodies Aerodynamics & Applications*, 20–24. doi:10.1.1.667.9620.
- Roache, P. J. 1994. “Perspective: A Method for Uniform Reporting of Grid Refinement Studies.” *Journal of Fluids Engineering* 116 (3): 405. doi:10.1115/1.2910291.
- Rouméas, Mathieu, Patrick Gilliéron, and Azeddine Kourta. 2009. “Analysis and Control of the near-Wake Flow over a Square-Back Geometry.” *Computers and Fluids* 38 (1): 60–70. doi:10.1016/j.compfluid.2008.01.009.
- Roy, Christopher, Jeffrey Payne, Mary McWherter-Payne, and Kambiz Salari. 2004. “RANS Simulations of a Simplified Tractor/Trailer Geometry BT - The Aerodynamics of Heavy Vehicles: Trucks, Buses, and Trains.” In , edited by Rose McCallen, Fred Browand, and James Ross, 207–18. Berlin, Heidelberg: Springer Berlin Heidelberg. doi:10.1007/978-3-540-44419-0_21.
- Roy, Subrata, Pengfei Zhao, Arnob DasGupta, and Jignesh Soni. 2016. “Dielectric Barrier Discharge Actuator for Vehicle Drag Reduction at Highway Speeds.” *AIP Advances* 6 (2). doi:10.1063/1.4942979.

- Salari, Kambiz, J. Ortega, and Paul Castellucci. 2004. "Computational Prediction of Aerodynamic Forces for a Simplified Integrated Tractor-Trailer Geometry." In *34th AIAA Fluid Dynamics Conference and Exhibit*. Fluid Dynamics and Co-Located Conferences. American Institute of Aeronautics and Astronautics. doi:doi:10.2514/6.2004-2253.
- Schoon, Ronald E. 2007. "On-Road Evaluation of Devices to Reduce Heavy Truck Aerodynamic Drag." SAE International . doi:10.4271/2007-01-4294.
- Singh, S N, L Rai, P Puri, and A Bhatnagar. 2005. "Effect of Moving Surface on the Aerodynamic Drag of Road Vehicles." *Proceedings of the Institution of Mechanical Engineers, Part D: Journal of Automobile Engineering* 219 (2): 127–34. doi:10.1243/095440705X5886.
- Sinha, Sumon K. 2008. "Improving Fuel Efficiency of Tractor Trailer Trucks with Deturbulator Aero-Drag Reduction." In *Commercial Vehicle Engineering Congress & Exhibition*. doi:10.4271/2008-01-2602.
- Sovran, Gino. 1978. *Aerodynamic Drag Mechanisms of Bluff Bodies and Road Vehicles*. Springer. doi:10.1007/978-1-4684-8434-2.
- Spalart, P, and S Allmaras. 1992. "A One-Equation Turbulence Model for Aerodynamic Flows." In *30th Aerospace Sciences Meeting and Exhibit*. Aerospace Sciences Meetings. American Institute of Aeronautics and Astronautics. doi:doi:10.2514/6.1992-439.
- Steers, L L, and E J Saltzman. 1977. "Reduced Truck Fuel Consumption through Aerodynamic Design." *Journal of Energy* 1 (5). American Institute of Aeronautics and Astronautics: 312–18. doi:10.2514/3.47945.
- Storms, Bruce, James C. Ross, James T. Heineck, Stephen M. Walker, David M. Driver, Gregory G. Zilliac, and Daniel P. Bencze. 2001. "An Experimental Study Of The Ground Transportation System (GTS) Model In The NASA Ames 7- By 10-Ft Wind Tunnel."
- Storms, Bruce, Dale Satran, James Heineck, and Stephen Walker. 2004. "A Study of Reynolds Number Effects and Drag-Reduction Concepts on a Generic Tractor-Trailer." In *34th AIAA Fluid Dynamics Conference and Exhibit*. Fluid Dynamics and Co-Located Conferences. American Institute of Aeronautics and Astronautics. doi:doi:10.2514/6.2004-2251.
- Storms, Bruce, Dale R. Satran, James T. Heineck, and Stephen M. Walker. 2006. "A Summary of the Experimental Results for a Generic Tractor-Trailer in the Ames Research Center 7- by 10-Foot and 12-Foot Wind Tunnels." Moffett Field, CA.
- TIAX. 2010. *Technologies and Approaches to Reducing the Fuel Consumption of Medium- and Heavy-Duty Vehicles*. Washington, DC: The National Academies Press. doi:10.17226/12845.
- Tooren, M.V., and G.V. Raemdonck. 2009. "A Practical Scientific Approach For Aerodynamic Truck Design." *Proceedings Of Euromech Colloquium 509: External*

- Aerodynamics Of Railway Vehicles, Trucks, Buses And Cars*, 293–303.
- Trucker Path. 2017. “Trucking Industry Statistics.” <https://truckerpath.com/blog/trucking-industry-statistics/>.
- Verzicco, R., M. Fatica, G. Iaccarino, P. Moin, and B. Khalighi. 2002. “Large Eddy Simulation of a Road Vehicle with Drag-Reduction Devices.” *AIAA Journal* 40 (12): 2447–55. doi:10.2514/2.1613.
- West, G. S., and C. J. Apelt. 1982. “The Effects of Tunnel Blockage and Aspect Ratio on the Mean Flow Past a Circular Cylinder with Reynolds Numbers between 104 and 105.” *Journal of Fluid Mechanics* 114: 361–77. doi:10.1017/S0022112082000202.
- Wilcox, D.C. 1993. *Turbulence Modeling for CFD*. DCW Industries, Inc. La Canada, California. doi:0963605151.
- Wong, D. T M, and W. A. Mair. 1983. “Boat-Tailed Afterbodies of Square Section as Drag-Reduction Devices.” *Journal of Wind Engineering and Industrial Aerodynamics* 12 (2): 229–35. doi:10.1016/0167-6105(83)90071-5.
- Wood, R.M. 2006. “A Discussion of a Heavy Truck Advanced Aerodynamic Trailer System.” *SOLUS-Solutions and Technologies LLC*.
- Wood, R.M., and S.X.S. Bauer. 2003. “Simple and Low-Cost Aerodynamic Drag Reduction Devices for Tractor-Trailer Trucks.” *SAE Transactions* 112 (2): 143–160. doi:10.4271/2003-01-3377.
- Yi, W. 2007. “Drag Reduction Of A Three-Dimensional Car Model Using Passive Control Device.” Seoul National University.

Appendix: Detailed Preliminary Study Analysis

Examining velocity contour at device configuration #1 (Figure A.1), the flow develops through tractor underbody section of the channel and attaches to the device all the way to the channel exit. The flow slows down due to the area expansion caused by the ramp; as the flow exiting the device exits with an average outlet velocity of 14.8 m/s and a mass flow rate of 0.35 kg/s. Compared to the baseline channel, the average outlet velocity is approximately two times higher which is attributed to the elimination of recirculation as the device configuration provides a smooth transition from the tractor underbody section. As for the mass flow rate, it was slightly lower compared to the baseline model. This could be attributed to the reduction of the surface area at the outlet of the channel due to the ramp.

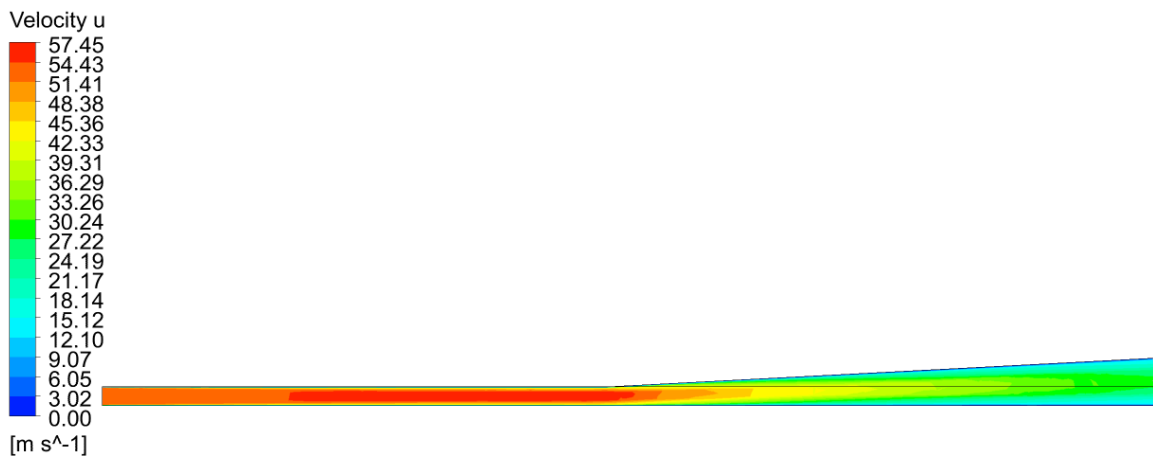


Figure A.1: Velocity contour at the centerline of device configuration #1 (Ramp 3° - Straight Side Skirt)

Moving on to device configuration #2, it is evident that the velocity throughout the length of the trailer underbody section (Figure A.2) is generally higher when compared to device configuration #1 (Figure A.1). This is expected as the converging side skirts would reduce the cross-sectional area through the channel compared to configuration #1, which has straight side skirts. This would accelerate the flow and allow for better flow attachment.

The average outlet velocity was around 27.79 m/s, which is approximately two folds the outlet velocity of configuration #1 and around 3.6 times higher than the baseline channel. In addition, the mass flow rate was 0.403 kg/s, which is approximately an increase of 16.5% compared to configuration #1 and a 13.2% increase compared to the baseline channel.

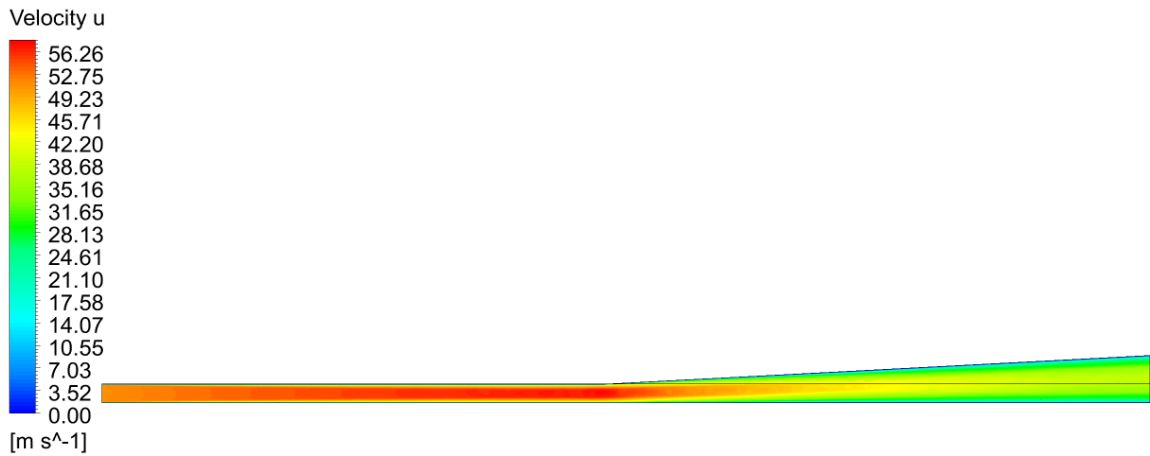


Figure A.2: Velocity contour at the centerline of device configuration #2 (Ramp 3° - Side Skirt 3°)

As for device configuration #3, the side skirt angle is increased from 3 degrees to 4 degrees compared to configuration #2. The overall velocity through the underbody trailer section is increased compared to the previous two configurations, which can be seen in Figure A.2. The average outlet velocity was 36.2 m/s while the mass flow rate was 0.432 kg/s; both are the highest compared to the previous two configurations.

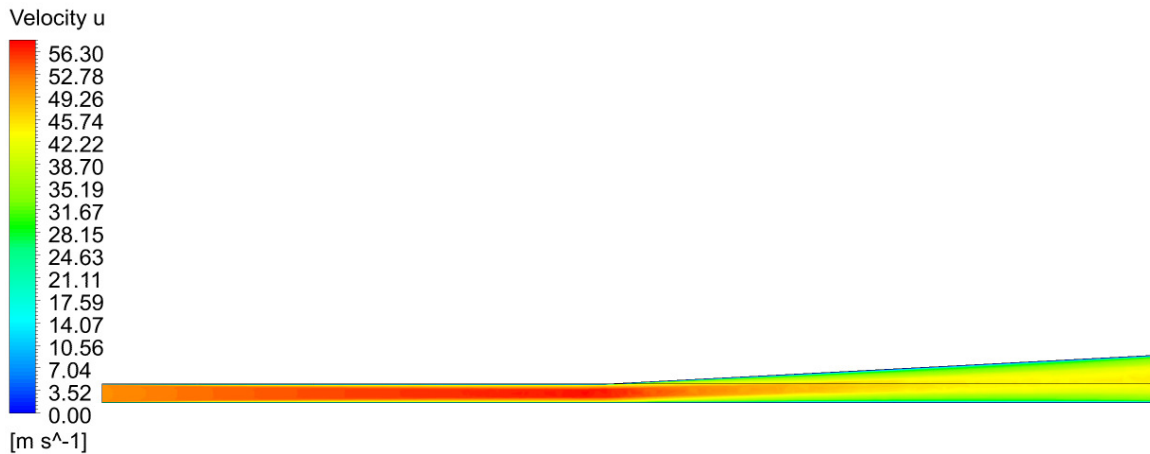


Figure A.3: Velocity contour at the centerline of device configuration #3 (Ramp 3° - Side Skirt 4°)

For device configurations #4 to 6, the ramp angle is increased from 3 degrees to 4 degrees. Examining device configuration #4, the flow remained attached to the ramp even as the configuration has straight side skirts (Figure A.4). The average outlet velocity was 13.1 m/s which is comparable to configuration #1 (Ramp 3° - Straight Side Skirt) as it also had straight side skirts. The mass flow rate was 0.40 kg/s, which is approximately an increase of 12.4% compared to device configuration #1.

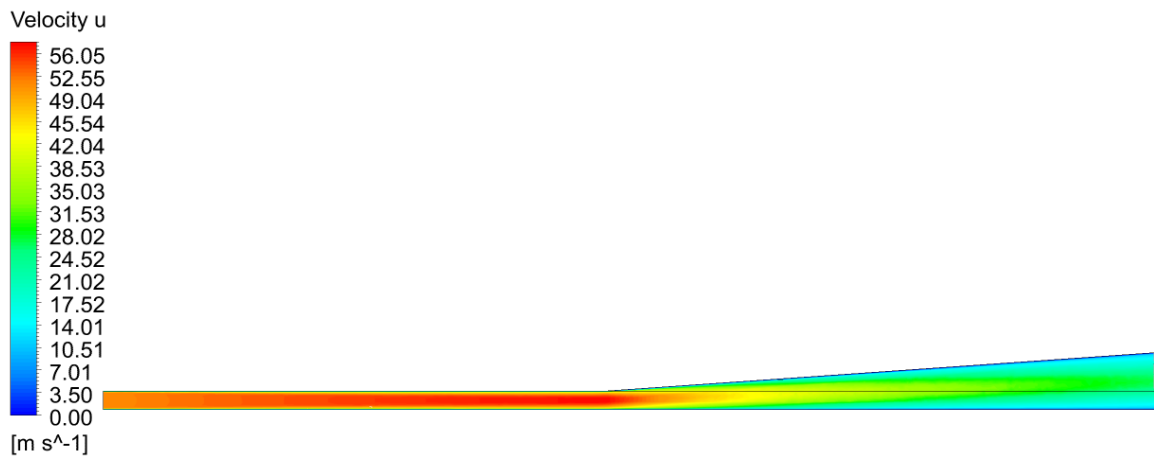


Figure A.4: Velocity contour at the centerline of device configuration #4 (Ramp 4° - Straight Side Skirt)

Increasing the side skirt angle to 3 degrees, the overall flow velocity throughout the trailer underbody section of the channel is increased as can be seen in Figure A.5. The average outlet velocity was 22.5 m/s which represents a decrease of 19% compared to configuration #2. This is reasonable as the surface area at the outlet of the channel is larger for configuration #5 (Ramp 4° - Side Skirt 3°) compared to configuration #2 (Ramp 3° - Side Skirt 3°). The mass flow rate was 0.439 kg/s, which presents an increase of 8.9 % compared to configuration #2.

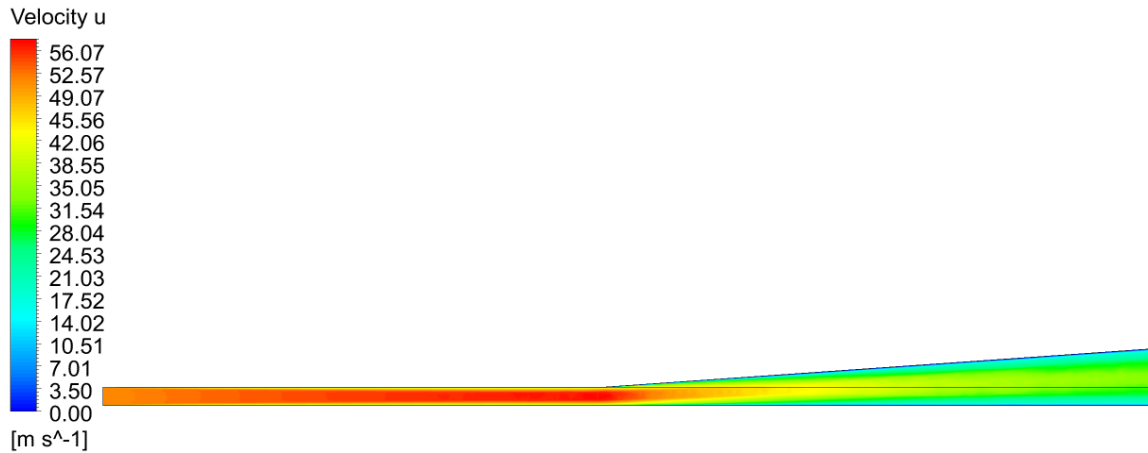


Figure A.5: Velocity contour at the centerline of device configuration #5 (Ramp 4° - Side Skirt 3°)

Examining configuration #6, the overall velocity throughout the channel was increased as shown in Figure A.6. The average outlet velocity was 29.8 m/s while the mass flow rate was 0.475 kg/s. Compared to configuration #3, the average outlet velocity decreased by 17.6 % while the mass flow rate increased by 10 %.

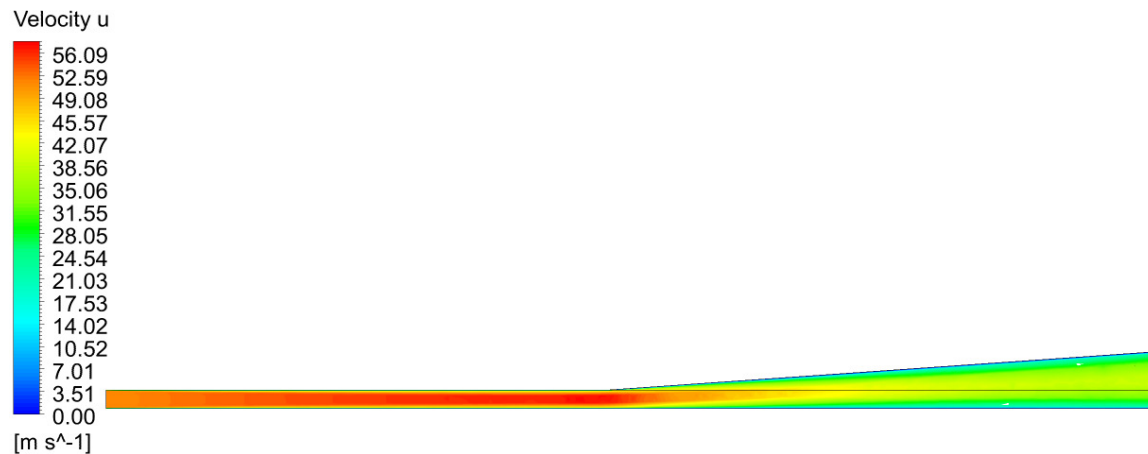


Figure A.6: Velocity contour at the centerline of device configuration #6 (Ramp 4° - Side Skirt 4°)

For configurations #7 – 9, the ramp angle was increased from 4 degrees to 5 degrees. Examining configuration #7, the flow separates through the trailer underbody section of the channel. This can be seen close to the channel exit, where negative velocity is evident. This means that a ramp angle of 5 degrees is just above the threshold of flow separation. The

average outlet velocity was 12.2 m/s, which is slightly lower than configuration #4 (Ramp 4° - Straight Side Skirt) which had an average outlet velocity of 13.1 m/s. Meanwhile, the mass flow rate was 0.46 kg/s.

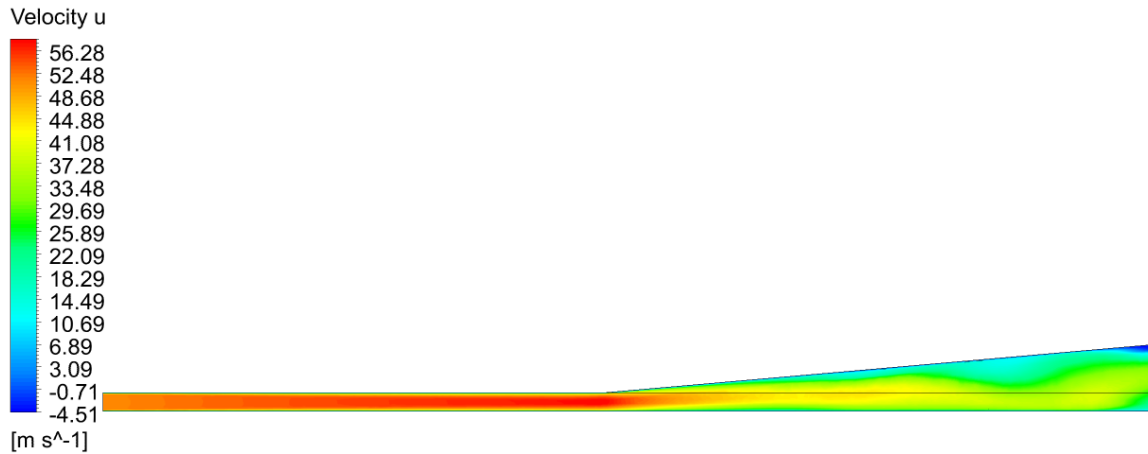


Figure A.7: Velocity contour at the centerline of device configuration #7 (Ramp 5° - Straight Side Skirt)

By removing the straight side skirts and adding a side skirt with an angle of 3 degrees, the flow separation that was evident in configuration #7 is eliminated in configuration #8 as shown in Figure A.8. The average outlet velocity is increased to 18.6 m/s, which is approximately an increase of 52.3 % compared to configuration #7. As for the mass flow rate, it was identical for both configurations. This is plausible as the flow started to separate near the end of the channel for configuration #7, thus the effect on the mass flow rate was not evident.

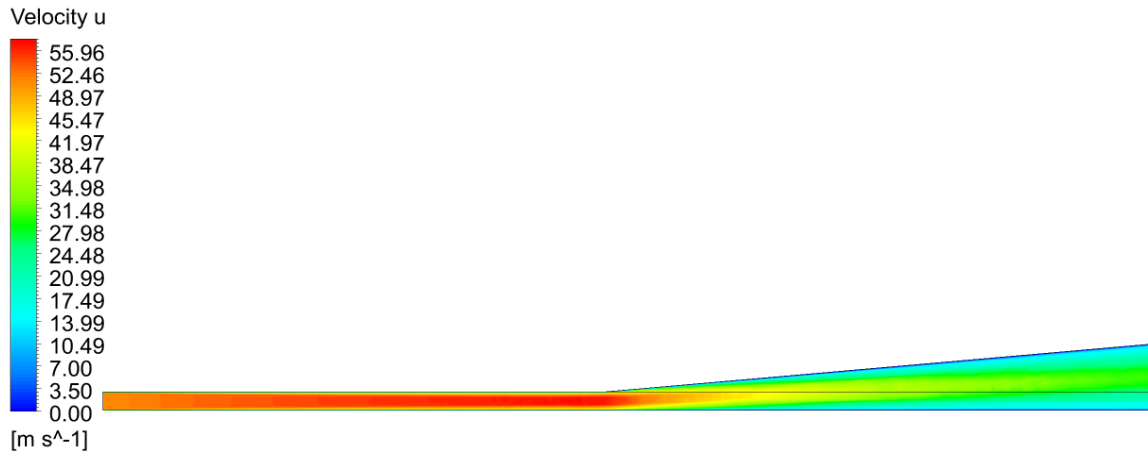


Figure A.8: Velocity contour at the centerline of device configuration #8 (Ramp 5° - Side Skirt 3°)

Examining configuration #9, the overall velocity throughout the trailer underbody section of the channel increased compared to configuration #8. The average outlet velocity was 24.9 m/s while the mass flow rate was 0.49 kg/s. This represents an increase of 33.7% and 6.5 % respectively when compared to configuration #8.

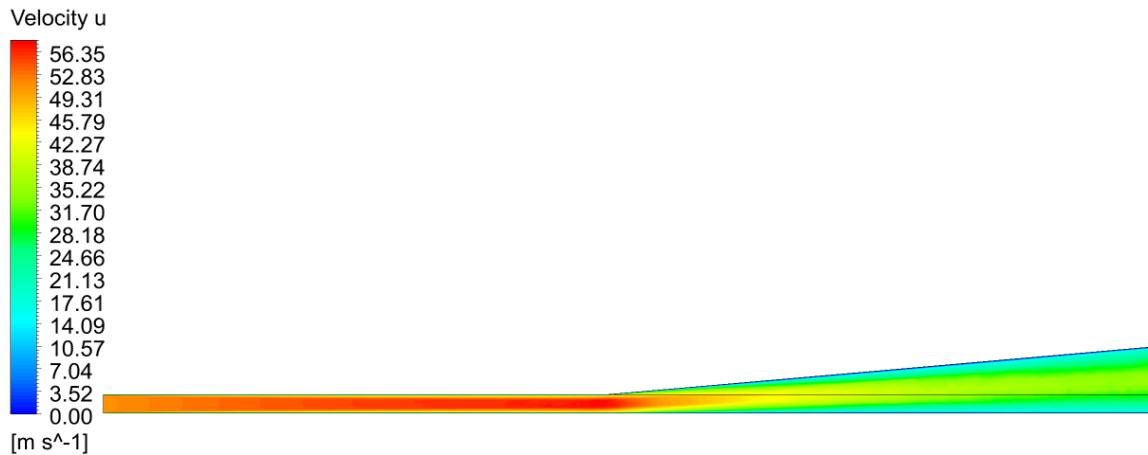


Figure A.9: Velocity contour at the centerline of device configuration #9 (Ramp 5° - Side Skirt 4°)

Moving on to configurations #10 to 12, the ramp angle was increased from 5 degrees to 6 degrees. As shown in Figure A.10, flow separation occurred much sooner in device configuration #10 compared to configuration #7. This is expected as the ramp angle was increased. The average outlet velocity was 9.9 m/s, which is the lowest velocity

between all device configurations. This drastic decrease in flow velocity can be attributed to the flow separating and recirculating approximately halfway through the trailer underbody section of the channel. The mass flow rate was 0.45 kg/s, which is a decrease of 2.2 % compared to configuration #7 (Ramp 5° - Straight Side Skirt).

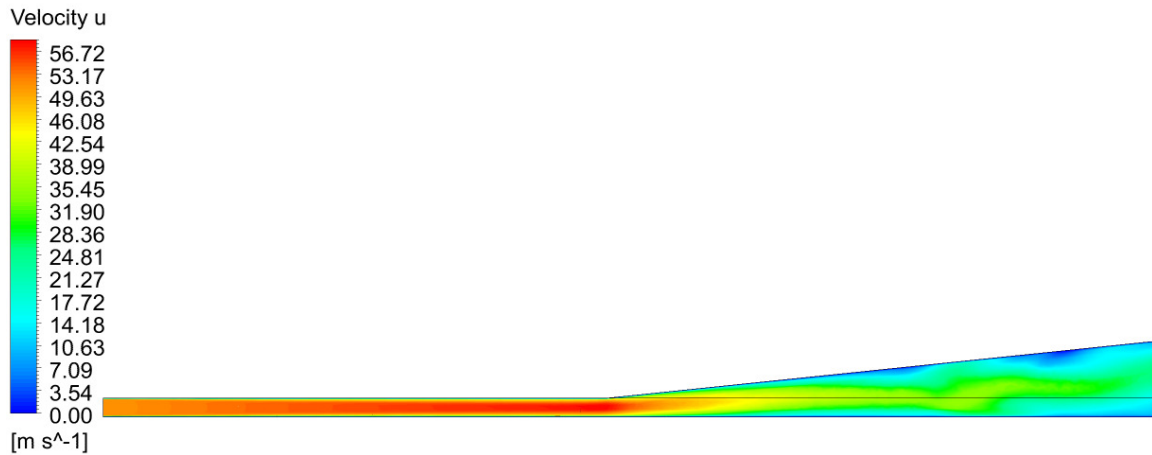


Figure A.10: Velocity contour at the centerline of device configuration #10 (Ramp 6° - Straight Side Skirt)

Examining the velocity contour of configuration #11, the flow separation seen in the previous configuration is eliminated. In addition, the overall flow velocity is higher as the average outlet velocity is 15.9 m/s. This can be attributed to the converging side skirts as they increase the flow velocity, which in turn energizes the flow allowing it to attach to higher ramp angles. The mass flow rate of this configuration was 0.46 kg/s which is identical to configuration #8.

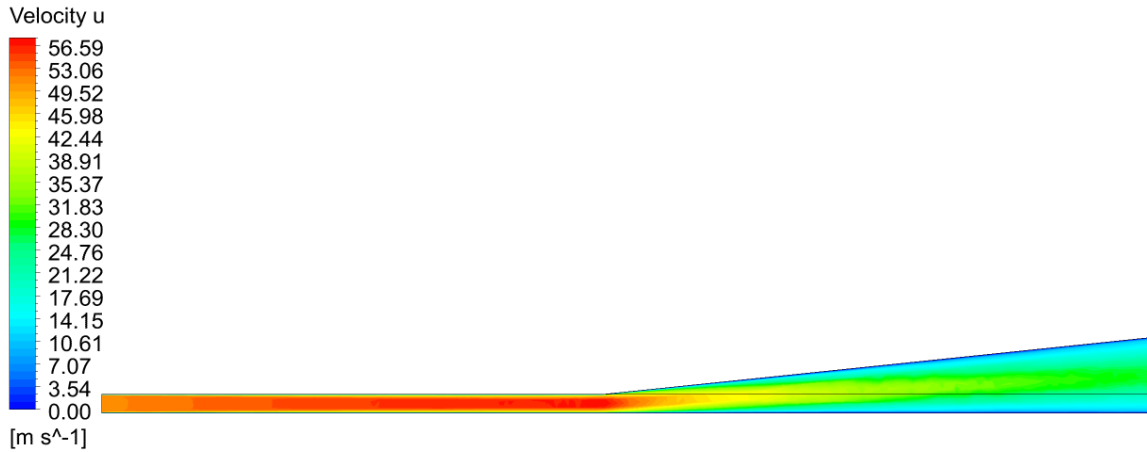


Figure A.11: Velocity contour at the centerline of device configuration #11 (Ramp 6° - Side Skirt 3°)

Increasing the side skirt angle to 4 degrees, the overall flow velocity of configuration #12 is higher compared to configuration #11. The average flow velocity increased approximately by 35 % to 21.4 m/s. In addition, the mass flow rate increased to 0.5 kg/s which is approximately 8.7 % compared to configuration #11. This configuration has the highest mass flow rate compared to all other device configurations. In addition, it has the highest ramp angle which allows for the device to have a higher ground clearance compared to the other two ramp angles when deployed.

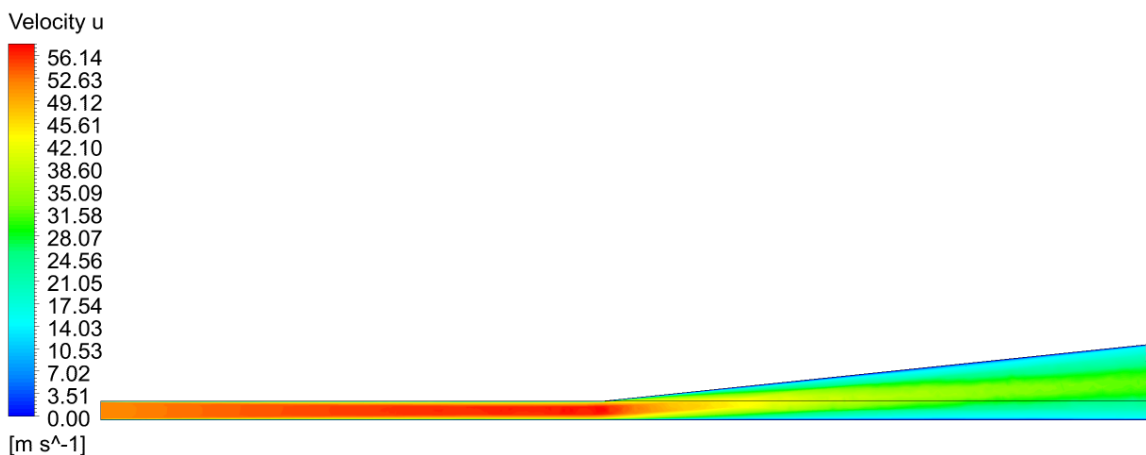


Figure A.12: Velocity contour at the centerline of device configuration #12 (Ramp 6° - Side Skirt 4°)